EFFECT OF INHOMOGENEOUS MAGNETIC FIELD ON HELICON ANTENNA PRODUCED EXPANDING PLASMA

By

SONU YADAV

PHYS06201204012

Institute for Plasma Research, Gandhinagar

A thesis submitted to the

Board of Studies in Physical Sciences

In partial fulfillment of requirements

for the Degree of

DOCTOR OF PHILOSOPHY

of

HOMI BHABHA NATIONAL INSTITUTE

July, 2019

Homi Bhabha National Institute[1]

Recommendations of the Viva Voce Committee

As members of the Viva Voce Committee, we certify that we have read the dissertation prepared by **Sonu Yadav** entitled **"Effect of inhomogeneous magnetic field on helicon antenna produced expanding plasma"** and recommend that it may be accepted as fulfilling the thesis requirement for the award of Degree of Doctor of Philosophy.

Chairman - Prof. Sudip Sengupta	27/02/2020
Guide / Convener - Prof. Prabal K. Chattopadhyay	27.02.2020
Examiner - Dr. Ramesh Narayanan	Ramesh Narayanan 27/02/2020
Member 1 - Dr. Joydeep Ghosh	Ghosh 27/2/2020
Member 2 - Dr. Devendra Sharma	Devendra Sharma 27/02/2020
Member 3 - Dr. Surya K. Pathak	27.02.20

Final approval and acceptance of this thesis is contingent upon the candidate's submission of the final copies of the thesis to HBNI.

I hereby certify that I have read this thesis prepared under my direction and recommend that it may be accepted as fulfilling the thesis requirement.

Date: 27/02/2020

Place: Gandhinagar

Prof. Prabal K. Chattopadhyay

Guide

[1] This page is to be included only for final submission after successful completion of viva voce.

STATEMENT BY AUTHOR

This dissertation has been submitted in partial fulfillment of requirements for an advanced degree at Homi Bhabha National Institute (HBNI) and is deposited in the Library to be made available to borrowers under rules of the HBNI.

Brief quotations from this dissertation are allowable without special permission, provided that accurate acknowledgement of source is made. Requests for permission for extended quotation from or reproduction of this manuscript in whole or in part may be granted by the Competent Authority of HBNI when in his or her judgment the proposed use of the material is in the interests of scholarship. In all other instances, however, permission must be obtained from the author.

Sonu

Sonu Yadav

DECLARATION

I, hereby declare that the investigation presented in the thesis has been carried out by me. The work is original and has not been submitted earlier as a whole or in part for a degree / diploma at this or any other Institution / University.

Sonu Yadav

List of Publications arising from the thesis

Journal:

1. "Effect of inhomogeneous magnetic field on plasma generation in a low magnetic field helicon discharge",

   Sonu Yadav, K. K. Barada, S. Ghosh, J. Ghosh, and P. K. Chattopadhyay, *Phys. Plasmas* **26**, 082109 (2019).

2. "Role of ion magnetization in formation of radial density profile in magnetically expanding plasma produced by helicon antenna"

   Sonu Yadav, S. Ghosh, S. Bose, K. K. Barada, R. Pal, and P. K. Chattopadhyay, *Phys. Plasmas* **25**, 043518 (2018).

3. "Formation of annular plasma downstream by magnetic aperture in the helicon experimental device"

   S. Ghosh, Sonu Yadav, K. K. Barada, P. K. Chattopadhyay, J. Ghosh, R. Pal, and D. Bora, *Phys. Plasmas* **24**, 020703 (2017).

4. "Characterization of low magnetic field and conventional helicon discharge"

   Sonu Yadav, K. K. Barada, J. Ghosh and P. K. Chattopadhyay, *to be submitted (2020)*

5. "Measurement of electron energy distribution in presence and absence of current free double layer",

   Sonu Yadav, K. K. Barada, J. Ghosh and P. K. Chattopadhyay, *to be submitted (2020)*

Conferences/ Schools:

International Participation:

1. "Formation of hollow density profile in Magnetically expanding plasma produced by helicon antenna" Sonu Yadav et al. 60th annual meeting of APS Division of Plasma Physics, 5-9 Nov, 2018, Portland, Oregon, USA
2. "Effect of non-uniform magnetic field on antenna-plasma coupling efficiency in a low magnetic field helicon discharge" 71st Annual Gaseous Electronic Conference (GEC), Sonu Yadav et al. 5-9 Nov, 2018, Portland, Oregon, USA
3. "Stochastic heating in magnetized plasma produce by helical antenna" Sonu Yadav et al. 44th EPS Conference on Plasma Physics, 26-30 June, 2017, Queen's University, Belfast, Northern Ireland.
4. "Generation of off-axially localized tail electrons in helical antenna produce cylindrical plasma" 69th Annual Gaseous Electronic Conference (GEC), Sonu Yadav et al. 10-14 Oct, 2016, Ruhr University Bochum, Germany.
5. "Controllable Location of Polarization Reversal in Nonuniform Helicon Plasma" 10th Asia Plasma and Fusion Association (APFA), Sonu Yadav et al. 14-18, December, 2015, Institute for plasma research, Gandhinagar, India.

National Participation:

1. "Measurement of Electron Energy Distribution in Presence and Absence of Current Free Double Layer in Helicon Plasma" Sonu Yadav et al. 32th National Symposium on Plasma Science & Technology 07-10 November, 2017, Institute for Plasma Research, Gandhinagar, India.

2. “Study of Helicon waves in nonuniform plasma” Sonu Yadav et al. 30th National Symposium on Plasma Science & Technology 01-04 December, 2015, Saha Institute of Nuclear Physics, Kolkata, India.
3. “Polarization Reversal of Helicon Wave in Nonuniform Plasma” Sonu Yadav et al. 29th National Symposium on Plasma Science & Technology and the International Conference, 8-11 December, 2014, Mahatma Gandhi University, Kottayam, Kerala, India.

Sonu Yadav

Dedicated

To

My Family

Especially to My Mother and Uncle

ACKNOWLEDGEMENTS

Undertaking this Ph.D. has been a truly transformative experience for me and it would not have been possible to do without the support and guidance that I received from many people. I would like to take this opportunity to extend my sincere gratitude and appreciation to all those who made this Ph.D. thesis possible.

First and foremost I wish to convey my deepest gratitude to my thesis supervisor Prof. Prabal Kumar Chattopadhyay for introducing me to an exciting field of plasma science and for his dedicated help, advice, inspiration, encouragement and immense support throughout the Ph.D. His enthusiasm, visionary view on research and his mission for providing high-quality work has made a deep impression on me. I am also thankful for his many hours of help he provided me. His expertise in experiments always helped me in learning new techniques and experimental methods I remember he used to say as 'student should judiciously use the time', this statement made me do extra hard work. He is not only an exceptional guide but a good human being too. I found his attitude always problem-solving irrespective of matter. It has been a wonderful experience for me while doing a Ph.D. under his guidance.

I would like to thank Dr. Joydeep Ghosh for his invaluable guidance in my Ph.D. thesis work. He always stood with me whenever I required support in terms of scientific and technical matters. I am also grateful to him for his reviews and advice during the writing of the thesis dissertation. His timely support and guidance helped me to complete the dissertation on time. He is a very nice personality.

I would like to extend my sincere gratitude to Prof. Rabindranath Pal for invaluable guidance in my Ph.D. thesis work.

I was fortunate enough to receive motivation and support from my senior lab members Dr. Kshitish Kumar Barada, Dr. Sayak Bose, Dr. Manjit Kaur, and Dr. Soumen Ghosh. I would also like to sincerely thanks my other lab colleagues Mrs. Renu, Mr. Buddu Ramesh and Mr. Narendar, especially Neeraj Wakde and Bhoomi Khodiyar for providing an educational and friendly environment in the Basic Lab.

I would like to thank my doctoral committee members Prof. Sudip Sengupta, Dr. Joydeep Ghosh, Dr. Devendra Sharma, and Dr. Surya Kumar Pathak for their useful suggestions and guidance during my Ph.D.

I especially thank Prof. Sudip Sengupta (Dean, Academics & Student Affairs) and Prof. Subroto. Mukherjee (Ex-Dean, Academics & Student Affairs) for their guidance in various matters and more important things related to HBNI.

I would like to thank Dr. G. Ravi, Dr. Ramasubramanian Narayanan, Prof. Subroto Mukherjee, Dr. Shantanu Kumar Karkari, Prof. Prabal K. Chattopadhyay, Dr. Pintu Bandyopadhyay, Dr. Joydeep Ghosh, Dr. Devendra Sharma, Dr. Mrityunjay Kundu, Dr. Mainak Bandyopadhyay, Dr. Nirmal K. Bisai, Dr. Daniel Raju, Dr. V. P. Anitha, Dr. Asim K. Chattopadhyay, Dr. V. Prahlad and others for their teaching to learn and understand the plasma physics and related subjects.

I want to thank my batch mates Umesh, Debraj, Narayan, Ratan, Amit, Arghya, Anup, Modhu, Rajnarayan, Ramkrishna, Bhumika and Surabhi for their support during my Ph.D. I would like to thank my all juniors Sagar, Atul, Jervis, Alamgir, Sandeep, Prabhakar, Deepak, Meenakshee, Pallavi, Harshita, Chetan, Rupak, Shivam, Avnish, Trithendu, Subrata, Arun, Gaurav, Anirban, Dipshikha, Arnab, Priti, Garima, Neeraj, Srimanta, Mayank, Yogesh, Chinmoy, Girija Shankar, Piyush, Pranjal, Satadal, Soumen, Pradeep, Devshree, Nidhi, Sanjeev, Hariprasad, Ayushi, Pawandeep, Swapnali, Tanmay, Karim, Prince, Jagannath, Satya, Lavanya, Ram, Vivek and others and seniors Dr. Neeraj Chaubey, Dr. Bibhu Prasad Sahoo, Dr. Mangilal Choudhary, Dr. Vidhi Goyal, Dr. Akanksha Gupta, Dr. Deepa Verma, Dr. Chandrashekhar Shukla, Dr. Vara Prasad Kella, Dr. Samirsinh G. Chauhan, Dr. Harish Charan, Dr. Roopendra Singh Rajawat, Dr. Meghraj Sengupta, Dr. Vikram Singh Dharodi, Dr. Aditya Krishna swamy, Dr. Rameshwar Singh, Dr. Pravesh Dhyani, Dr. Sushil Kumar Singh, Dr. Sanat Tiwari, Dr. Ujjwal Sinha, Dr. Gurudatt Gaur, Dr. Deepak Sangwan, Dr. Prabal Singh Verma, Dr. Vikram Sagar, Dr. Sita Sundar, Dr. Ashwin Joy, Dr. Rana Yadav, Dr. Dushyant Kumar Sharma, Dr. Sandeep Rimza, Dr. G. Veda Prakash, Dr. Satyananda Kar, Dr. T. Shekar Goud, Dr. Sharad Kumar Yadav, Dr. P. N. Maya, Dr. Jugal Chowdhury and others for providing friendly environment.

I am also grateful to people from the workshop, computer center, library, stores, purchase section, administration, transport section, accounts section, water plant, canteen, security staff members and hostel mess cook Jeeva and his team for their cooperation during my Ph.D. Thanks to volleyball as well.

Lastly and very most importantly I would like to express sincere gratitude towards my mother Mrs. Rajjo Yadav, uncle Mr. Rajesh Yadav and wife Mrs. Priti Yadav and brothers and sisters for their constant support and patience for the entire period. Their unconditional love and endless support helped me to make this possible. I would like to thank my hometown friends Mr. Vishal, Mr. Girish, Mr. Pintu and Mr. Arpit for their motivation words. In this continuation, I would like to include my baby girl 'Pranavi' which made me happy in any worst situation.

Finally, I would like to thank My Father Late Shri Kailash Chandra Yadav for giving me the strength and blessing during all the challenging moments in completing this thesis.

CONTENTS

SUMMARY

This thesis work has been focused on an experimental study of the effect of non-uniform magnetic field on helicon antenna produced expanding plasma. Particular emphasis has been given to understand the role of non-uniform magnetic field on enhanced helicon source plasma production efficiency at the low magnetic field, and the physics of downstream hollow density formation within the magnetic diverging region. This thesis also provides the relationship between the current free double layer (CFDL) and related electron dynamics in the diverging magnetic field configuration. Experiments are performed in the Helicon eXperimental (HeX) device at different at magnetic field strengths. The primary novelty of HeX is its unique design feature that allows the users to control the strength of magnetic field gradients at different locations of source and expansion region. This feature is fully utilized to study the helicon discharge in this thesis.

Helicon plasma is being studied over few decades. Initial studies were concentrated around phenomena related to wave excitation, propagation and absorption. This kind of plasma shows significant high ionization efficiency. Hence, it has found various applications, though the exact mechanism of power absorption is not yet understood well. Historically, conventional helicon plasma is produced in a uniform magnetic field of the order of 200 Gauss or more for 13.56 source frequency. However, there is another class of helicon mode operation where the magnetic field is of the order of 10 to 50 Gauss, usually called low B (magnetic field) helicon. This also shows high plasma production efficiency. This is an economically attractive option compared to conventional helicon plasma. In this thesis work, it is shown that for low magnetic field operation with the non-uniform magnetic field, the plasma production efficiency is even higher than a uniform magnetic field case. It is shown that the antenna-plasma power coupling efficiency increases with the increasing magnetic field non-uniformity near the antenna. It is also observed that by introducing a non-uniformity in the magnetic field results in higher density than conventional helicon. This happens due to alteration in wave performance rather than the particle confinement. The measured wavelength for a uniform magnetic field near the antenna is twice the length of antenna. This suggests that half-wavelength helicon antenna excites full wavelength helicon wave. However, for non-uniform magnetic field, the measured wavelength is shown to be approximately equal to the antenna length for which the plasma density increased by more than a half order. Fundamentally, it opens up another area of wave coupling and absorption in a non-uniform magnetic field. Present study aims to understand the enhanced plasma production efficiency in presence of non-uniformity in low magnetic field.

Since helicon plasma along with the diverging (non-uniform) magnetic field has the potential application for plasma thruster. Irrespective of the high plasma production

efficiency of helicon discharge, the formation of a hollow density radial profile in the magnetic divergence region causes a reduction of total thrust. Hence, another part of this thesis addresses the detailed mechanism behind the formation of downstream hollow density profile in the magnetic divergence region and also discusses its removal mechanism. It is observed that the magnetic divergence plays the dominant role, not the geometric expansion in formation of hollow density profile. Moreover, the total number of particles integrated over the circular cross-section after the magnetic divergence is much more than that before the magnetic divergence. Such observation implies that there must be some mechanism that increases the total number of particles after the magnetic divergence, like local ionization. In magnetic divergence, where the strong gradient in the magnetic field is present due to that moving charge particles suffers the gradient-B drift. The gradient-B drift in the expansion chamber causes the rotation of the off-axis high energetic electrons in the azimuthal direction with a speed of 2×10^{6} cm/s. The rotation confines the electrons enough so that they traverse the ionization length in much shorter distance in the axial direction causes the off-axis additional ionization and hence formed the hollow density profile. Though hot electrons and gradient-B effect produce the off-axis additional plasma, if ions not magnetized, then ions produce off-axis are lost quickly to wall and electron maintain quasi-neutrality, as results density remain center peaked. So, the presence of three conditions, namely, energetic electrons, grad-B drift, and ion magnetization are necessary for forming a hollow density profile in his experiment. This study signifies the role of the magnetic field as a control parameter for thrust output in future helicon source based thrusters.

The Final part of the thesis discusses the electron dynamics of current free double. Under certain parameter zone, helicon plasma in a diverging magnetic field is prone to excite the current free double layer (CFDL). Since it is another feature of diverging (non-uniform) magnetic field, so we also studied the formation of CFDL and electron dynamics related to it. The CFDL is formed when the magnetic field divergence and geometric expansion are co-located otherwise, CFDL vanishes under the same operating conditions. In presence of CFDL structure, at upstream the measured EEPF shows the trapped and depleted tail electron energy distribution which are separated by the ε_{break}. Electron those have energy below than ε_{break} are trapped between the CFDL potential and source end wall sheath. This group of electrons is known as a trapped electron group. Electron those energies higher than the ε_{break} (this makes the depleted tail in EEPF at upstream) overcome the CFDL potential barrier and treated as free electrons. The free electrons at downstream show the approximate Maxwellian distribution and very closely resembles the shape and magnitude of the depleted upstream population. Our measurement shows the absence of electron 'beam' component rather it shows the depleted electron energy distribution function at upstream.

SYNOPSIS

Plasma is an ionized medium of the gas which supports many types of electrostatic and electromagnetic waves. External magnetic fields introduce anisotropy in the plasma medium and magnetized plasma columns support a number of waves both in parallel and perpendicular directions. Whistler waves are a low frequency right polarized (R wave) waves propagating along the magnetic field and well known in ionosphere plasma. The pure electromagnetic character of whistler waves changes to quasi-electromagnetic when these waves are confined to a boundary. The bounded whistler wave is known as helicon wave, which has both right and left polarization. Plasma ionized by helicon wave is known as helicon plasma. These waves propagate in the frequency range of; $\omega_{ci} \ll \omega_{LH} < \omega < \omega_{ce} \ll \omega_{pe}$. Helicon plasma source is one of the radio frequency plasma source that converts the rf energy into plasma density most efficiently and generates a high density plasma at relatively low rf powers. The term "helicon" was introduced first by the Aigrain in 1960 due to helical lines of the electric field associated with this wave. Interest in this topic subsided until Boswell in 1970, found that helicon waves were unusually efficient in producing plasmas. Nowadays the helicon plasma sources are well known for their generation of high-density plasma at relatively low rf powers and magnetic field. These sources can produce a wide range of plasma density ($10^{16} - 10^{19}\ m^{-3}$) at the low electron and ion temperatures, and for these reasons, these plasma sources are advantageous for various applications such as plasma processing, tokamak pre-ionization, and current drives, neutron sources and plasma thrusters. In addition to this, these discharges are also found suitable for various basic plasma studies such as double layers, parametric decay instability, pressure-driven drift wave instability, high beta experiments, and plasma confinement experiments by studying the instability and turbulence. The helicon discharge can be controlled by various parameters such as rf frequency, system size, fill-in pressure, and rf power.

Helicon plasmas are inherently very efficient for producing high-density plasma. The study of efficient plasma sources is salient for their application as an economic plasma source. The efficiency of any plasma source depends on the power coupling mechanism from power delivering source to plasma. In helicon discharge, the coupling of power from the antenna to plasma occurs through different coupling mechanisms. At very low power and low magnetic field, it happens through capacitive mode. As power and magnetic field increases, coupling occurs through inductive mode and finally through helicon wave mode. Out of these three modes, helicon wave mode exhibits the maximum power coupling efficiency. The efficiency of plasma source is also described in terms of plasma production efficiency, which is the ratio of a total number of electrons produced to input rf power. Out of these three modes, the helicon wave mode plasma also exhibits maximum plasma production efficiency.

Conventional helicon sources are operated at a magnetic field corresponding to an electron cyclotron frequency (ω_{ce}) equal to 40 to 200 times of source frequency (ω_{rf}). This means that for normal operation of the helicon source using 13.56 MHz source, 200 -1000 G magnetic field is required. However, helicon plasma sources have also shown helicon wave excitation around a particular low magnetic field (<100 G). Here, a low magnetic field (20-30 G) means ω_{ce}~ 5-10 ω_{rf}. At the high magnetic field, in helicon plasma, the density increases monotonically with the increase of magnetic field, but this dependency is violated at the low magnetic field where density peaks around narrow magnetic field values. Most of the experiments are performed at the low magnetic field by keeping a uniform magnetic field near the antenna. In this thesis, the efficient plasma production by helicon wave in a non-uniform magnetic field near the antenna center is reported. The experiments are performed in Helicon eXperimetnal device (HeX) present at Institute for Plasma Research (IPR), India with different magnetic field non-uniformities near the helicon antenna by keeping the magnetic field value < 100 G. Antenna plasma coupling efficiencies are studied by measuring the antenna current with and without plasma. Plasma production efficiencies are also estimated in different magnetic field configurations. It is observed that coupling efficiency increases with increase in the non-uniformity of the magnetic field near the helicon antenna.

When an efficient helicon plasma source is combined with the diverging magnetic field configuration, which is similar to the magnetic nozzle, it generates plasma flows. In our experiment, a diverging magnetic nozzle is created by powering a set of electromagnets placed at required locations. Helicon plasma source with diverging magnetic field configuration attracts increasing interest due to its potential application for plasma thruster. In such a device, the efficiency of thrust generation does not only depend on efficient plasma production but also on the radial profile of plasma density. Formation of hollow density profile within the magnetic nozzle is a serious concern; it causes a reduction of total thrust. In HeX, the density profile within the magnetic nozzle is seen to be modified from centrally peaked to hollow as the external magnetic field is increased. The hollow density occurs above a characteristic field value when the ions become magnetized in the expansion region. The occurrence of hollow density profile is observed only after the magnetic divergence. The formation of hollow density profile is attributed to two main reasons, either due to additional off-axis ionization or due to radially outward plasma transport. The radially outward plasma transport in our experiments is neglected due to the absence of radial electric field. In a diverging magnetic field, the magnetic field does not only vary in the axial direction, but also in the radial direction which affects the motion of charged particles by creating the gradient-B drift. In our experiments, we observe the presence of energetic tail electrons off-axially both in the source and expansion chambers. Rotation of energetic tail electrons in the azimuthal direction due to the gradient-B drift within magnetic expansion leads to an additional off-axis ionization and forms the hollow density profile in our experiments. Although gradient-B drift and tail electrons are present, the radial density profile is still centrally peaked for unmagnetized ion case in the expansion chamber of HeX. So it is concluded that the gradient-B drift effect is an essential but not sufficient condition to form radial hollow density profile. If the ions are not magnetized, then the off-axially produced additional plasma is not confined, and the density profile retains the on-axis peaked nature. The present experimental work discusses both the source plasma production efficiency and the formation of hollow density profiles in inhomogeneous (diverging) magnetic field. This study is significant towards the design of an efficient helicon plasma-based thruster.

The diverging or non-uniform magnetic field of the expanding plasma does not only affects the density distribution but also the plasma potential. Helicon plasma source with expanding plasma geometry and a diverging magnetic field is seen to have modified plasma potential structure axially, which does not need to be Boltzmannian in nature. When a plasma is produced in the narrow source chamber, and it is subjected to diffuse into the bigger expansion chamber in the presence of the applied diverging external magnetic field, it leads to the formation of local potential structure known as a current free double layer (CFDL). In most of the work, the existence of CFDL is manifested by the presence of ion beam downstream of the CFDL; electrons also play a significant role. Few experimental observations are available of electron energy probability function (EEPF) in the presence of CFDL. This thesis also deals with the experimental measurement of EEPF in presence and absence of CFDL. In the presence of CFDL, the ion beam is observed in the HeX before, but the behavior of electrons is not yet studied. The study of electron energy distribution in the presence of CFDL is also presented in this thesis. Making use of the expansion chamber, we study the effect of diverging magnetic field on hollow radial density profile formation and double layer formation.

Experiments are performed in the helicon plasma experiments (HeX), which consists of a narrow glass tube connected to a larger stainless steel chamber. A helicon antenna is used to generate the plasma, placed around the glass tube. This antenna is also used to excite the helicon wave in the plasma. This thesis deals with the detailed study of the source and expansion chamber plasma produced by helicon antenna. In the source chamber, the effect of the non-uniform magnetic field is studied. The contents of the thesis are briefly discussed as follows;

Chapter 1 Introduction. This chapter contains the history of relevant research on helicon plasma, followed by a brief overview of helicon sources and its application. In this chapter, we discuss the research motivation and objective behind the work. The thesis issues are also highlighted in this chapter, followed by thesis organization.

Chapter 2 Theory of helicon waves. This chapter is about the theory of helicon waves in radially uniform and non-uniform density plasma. Helicon waves are low-frequency R-waves and belong to the category of whistler waves. The theoretical description of the cold plasma di-electric tensor is discussed in this chapter, followed by the dispersion of whistler and helicon waves. Since helicon waves are bounded whistler, derivation of the helicon wave under the assumption of uniform density cylindrically bounded plasma is derived where solutions of helicon wave fields are in the form of Bessel's functions. When finite electron mass is considered, the expression for dispersion relation shows second branch of dispersion along with the helicon wave mode. This second mode is called Trivelpiece-Gould (TG) mode.

When non-uniform radial density distributions are considered, the second-order differential equation of the wave field is solved numerically because the equation becomes non-linear and complex enough that only a numerical solution is possible. The solutions for the radial wave magnetic field components for different density profiles are solved numerically. The wave profile becomes steeper with sharper density profiles. The zero-crossing point of the azimuthal component (B_θ) of wave magnetic field progressively moves inward as density profile sharpens. This point also separates the inner or outer wave magnetic field patterns of helicon waves.

Chapter 3 Experimental device, diagnostics, and helicon wave characterization. This chapter describes the experimental setup in details. Implemented diagnostics, including the construction of various probes and method of data analysis are discussed. The experimental system consisting of a source and expansion chamber, vacuum pumping system, magnet system, helicon antenna, RF power, and matching system are described in detail. The diagnostics including different types of electric probes, for example, RF compensated Langmuir probe, double and triple Langmuir probe and emissive probe and also high frequency magnetic B-dot probe are developed to diagnose the plasma. The data analysis techniques for the above-mentioned diagnostics are also discussed. The functioning of rf compensated Langmuir probe, especially for moderate density rf plasma ($\sim 10^{16}\ m^{-3}$) is described in detail. A Matlab code is developed for Langmuir probe data analysis emphasizing the moderate density plasma. The knowledge of electron energy distribution has great importance in understanding the nature of current free double layer (CFDL). The double derivative of a single Langmuir probe current is proportional to the electron energy probability function (EEPF). To measure the electron energy probability function (EEPF) a double derivative circuit has been developed. The circuit design is a compromise between the better energy resolutions to low energy electrons side and high signal to noise ratio to high energy electron side. The HeX plasma is produced by powering the m = +1 helicon antenna operating at 13.56MHz frequency at various rf powers, magnetic fields and fill in pressures. The conventional helicon plasma is identified by density mode transitions along with axial helicon wave magnetic field measurement. An abrupt change in discharge regimes observed by the plasma density jump.

Chapter 4 Plasma generation in a non-uniform low magnetic field. Characterization of helicon plasma in the non-uniform magnetic field near the antenna is discussed here. The plasma is produced in different non-uniform magnetic field configurations keeping the magnetic field (< 100 G) at the center of the antenna same. The different magnetic field configurations are created by powering different combination of electromagnets. The antenna plasma coupling efficiencies are studied by measuring the antenna current with and without plasma. Plasma production efficiencies are also estimated in all magnetic field configurations. The coupling efficiencies increase with increasing the magnetic field non-uniformity near the antenna. The plasma density away from the antenna center at z = 31cm is measured by varying the magnetic field keeping the constant rf power and fill in gas pressure for all magnetic field configurations. The observation of beat wave in the axial variation of the axial wave magnetic field suggests the presence of different radial wave mode. Measurement of axial wavenumber along with the estimation of radial wavenumber suggests wave propagation near the resonance cone surface causing more absorption and hence the density peak. The absorption of the helicon wave near the resonance cone surface is correlated with excitation of electrostatic fluctuations. It is observed that the fluctuation level increases significantly at that magnetic field where density peaking occur. The density with low magnetic helicon mode in a non-uniform magnetic field is shown to be significantly higher than conventional helicon wave mode at similar power and pressure. The wavelength is measured for a nonuniform magnetic field near the antenna when the magnetic field is kept at 25 G and 50 G at the antenna center. For 25 G case, the measured axial wavelength is found to be twice the length of the antenna. This suggests that half-wavelength antenna excites full wavelength helicon wave. However, for 50 G case, the measured wavelength is shown to be approximately equal to the length of the antenna contrary to the usual observation that half-wavelength antenna produces full wavelength helicon wave. A manuscript describing the effect of nonuniform magnetic field on plasma generation is **published in Phys. Plasmas 26, 082109 (2019) Sonu Yadav et al.**

Chapter 5 Radial plasma profile and off-axial electron heating of magnetically expanding plasma. This chapter is focused on hollow density profile formation in magnetically expanding helicon antenna produced plasma. This chapter presents the study of off-axis electron heating of helicon antenna produced plasma. In the expansion chamber of Helicon eXperimental (HeX), there is a formation of hollow density profile within magnetic divergence. This profile is of serious concern as such type of structure in magnetically expanding plasma causes reduction of the total thrust and, therefore, it is necessary to study the hollowness of the radial density profile at the nozzle throat to increase the thrust efficiency. In the HeX device, the geometric aperture is fixed, but the position of the magnetic aperture can be varied. A hollow plasma density is formed downstream, always within the magnetic nozzle. This occurs irrespective of the relative position of the geometric expansion. This is contrary to the earlier propositions made by others that a radial electric field is necessary to produce a hollow plasma profile. Instead, the ionization of neutrals in the radially outer region by tail electrons, rotating fast due to gradient-B drift in the azimuthal direction, seems to account for the observed off-axis density peaking or hollow density in the present experiment. This work is published in **Phys. Plasmas 24, 020703, (2017)** S. Ghosh, **Sonu Yadav et al.**

Experiments are further performed to study in detail the hollowness within the magnetic divergence. It is found that the density profile in the magnetic nozzle of a HeX is modified from centrally peaked to hollow as the external magnetic field is varied. This change in nature occurs above a characteristic field value when the ions become magnetized in the expansion chamber. The density profile in the source chamber behind the nozzle, however, remains peaked on-axis irrespective of the magnetic field. The electron temperature is observed hollow both in source and expansion chamber. Although the tail electrons and gradient-B drift are present in the magnetic expansion, it seems, if the ions are not magnetized, then the off-axially produced additional plasma is not confined, and the density profile retains the on-axis peak nature. The present experiment is significant to the design of an efficient helicon plasma-based thruster. This work is published in **Phys. Plasmas 25, 043518, (2018) Sonu Yadav et al.**

Chapter 6 EEPF of the current free double layer. The electron energy distribution in the presence and absence of current free double layer (CFDL) is described here. The helicon plasma source with an expanding plasma geometry and diverging magnetic field can sustain a large potential drop locally. The formation of CFDL and consequential ion acceleration in geometrically and magnetically expanding rf plasmas are the subject of intense research since this type of system is useful for the development of plasma propulsive device. The measurements of electron energy probability functions (EEPF) are performed in HeX in presence and absence of double layer. The double layer vanishes when the magnetic expansion is far away from the geometric expansion. The upstream measurement of EEPF in the presence of CFDL shows a depleted electron energy distribution above the break energy. This break energy corresponds to the CFDL potential drop. The electrons having energy less than the break energy are trapped between the CFDL and the sheath at the insulating source end wall. The electron having higher energy than the break energy overcomes the double layer and act as a free electron. In previous laboratory experiments, in multiple plasma machines operated in a double plasma mode, the ions and electrons energy distributions were measured. The results showed both trapped particles (reflected by the DL) and free particles (accelerated by and overcoming the DL). The EEPF in the absence of CFDL does not show any depleted electron distribution. A manuscript describing the EEPF in presence and absence of CFDL potential is **under preparation (Sonu Yadav et al.)**.

Chapter 7: **Conclusion and future work.** This thesis deals with the study of helicon antenna produced plasma in an inhomogeneous magnetic field. The inhomogeneous magnetic field near the antenna results in efficient plasma production. This thesis established the cause behind the generation of efficient plasma in inhomogeneous low

magnetic field helicon discharge. This thesis provides detailed experimental evidence for the formation of hollow density profile in the diverging magnetic field in the expansion chamber. It also reveals the cause behind off-axis electron heating. Finally, the thesis also discusses the electron energy distribution in the presence of the current free double layer.

LIST OF FIGURES

Chapter 1
Introduction

1.1 History of helicon plasma

Plasma is an ionized gas which contains ions (positive or negative), electrons and neutral (atom or molecules). The ionized gas can be called plasma if it satisfies the following criteria: it should be quasi-neutral, and the charged particles must exhibit collective behavior. An important property of plasma is that it can support many electrostatic and electromagnetic waves. Plasma can be produced and confined with or without the application of an external magnetic field. An external magnetic field is often used in the laboratory plasma which serves two main purposes, it increases the overall plasma confinement and introduces an anisotropy due to which magnetized plasma can support a number of waves both in parallel and perpendicular directions. The classification of plasma waves is often performed based on the direction of propagation and polarization with respect to the external magnetic field. The wave modes are identified by their dispersion relations, which are the functional dependence between the wavelength and frequency. The group and phase velocity, cutoff, and resonance can be derived from dispersion relation.

The low frequency right circularly polarized electromagnetic waves (R-wave) propagating along the magnetic field are typically referred to as whistlers [1] which are well known in the ionosphere and the magnetosphere. In space science, a whistler is specifically defined as an electromagnetic wave which is excited by lightning and dispersed while propagating through the ionosphere and the magnetosphere. These waves lose their electromagnetic character and become partially electrostatic when confined in a cylinder. Their propagation and polarization also change within the boundary. These bounded whistlers are often called “helicons.” Helicons are quasi-electromagnetic waves and may have both right and left-hand polarizations, unlike whistlers, which have pure electromagnetic character and only right-hand polarization [2].

The term “helicon” was coined by Aigrain [3] in 1960, to describe the electromagnetic wave propagating in the solid metal. He called these waves helicons because of the helical lines of force associated with these waves. The helicon waves in metallic sodium were first observed by Bowers et al. [4] who also investigated their dispersion relation. They identified the waves as those proposed by Aigrain. The detailed theory for propagation and attenuation of helicon wave in gaseous plasma was derived by Klozenberg, McNamara, and Thonemann (KMT) [5] in a uniform cylindrical plasma. Experimentally, the helicons were first studied by Lehane, and Thonemann [6] in toroidal ZETA fusion device, who carried out experiments to test the theoretical prediction of KMT and the experimental results were in very good agreement with the theory. In another work, the propagation of helicon waves in a non-uniform plasma was studied by Blevin et al. [7] who gave a qualitative explanation for some of the discrepancies between the experimental results of Lehane et al. [6] and the uniform plasma theory of the helicon waves.

In 1970, Boswell [8] was first to use helicon waves as an efficient source for high density (~ 10^{19} m^{-3}) plasma production. The density obtained was higher by an order of magnitude compare to conventional RF discharges with equivalent input power. The efficient plasma production by helicon waves led to an increased interest in the helicon plasma physics. Plasma with high density and low electron (ion) temperature is useful for a practical plasma source. The helicon source has various applications such as industrial plasma processing [9,10], pre-ionization [11,12] and current drives for fusion devices [13–15], negative ion production [16,17] and space plasma thrusters [18–21]. In addition to these, the helicon sources are also useful for various basic research including double layers, parametric decay instability, pressure driven drift wave instability, high beta experiments, and plasma confinement experiments by studying the instability and turbulence.

The mechanism responsible for efficient plasma production in helicon plasma is still not comprehensively understood. In the last three decades, it was believed that several collisional and collision-less processes were considered responsible for the efficient plasma production by helicon waves. Landau damping was first considered by Chen [22] as a possible candidate for the energy transfer to the plasma. Landau damping is a collision-less phenomenon, where the wave energy is transferred to the particle traveling near the phase velocity of the wave. Molvik et al. [23] demonstrated the Landau damping of the wave by the detection of hot electrons using RF modulated emissions of Ar+ light. However, it was later discarded because of the insufficient number of fast electrons observed in the experiment [24]. Later, Shamrai et al. [25,26] suggested that the strong collisional damping of the Trivelpiece-Gould (TG) wave can explain the efficient power absorption. In this process mode conversion occurs from helicon to TG wave, TG wave with small radial wavelength is then damped strongly in the plasma due to enhanced collisional damping of the TG wave near the surface [25]. Other possible mechanisms such as the excitation of ion-sound parametric turbulence/instability [27,28], radially localized modes [29] and nonlinear trapping of electrons in helicon wave fields [30,31] were also suggested as possible mechanisms for the efficient plasma production in helicon discharge.

1.2 Motivation and Objective

Among various RF discharges, the helicon source is known to provide a highly efficient plasma source with exceptionally high density at modest input RF power compared to conventional inductive or capacitive discharge [32]. Due to their high production efficiencies, helicon sources find their applications in various places. Moreover, when used in a diverging magnetic field configuration, it is capable of producing plasma flow, which has the potential application for advanced plasma propulsion system [33]. The helicon research continues to progress in understanding and improvement on production efficiency and mechanism for flow generation when combined in a diverging magnetic field configuration in the downstream. In addition, helicon research also concentrates on various other basic studies related to wave propagation, wave heating, and instabilities. The present thesis objective is to study the production efficiency and the downstream physics.

Conventional helicon system operates at an external magnetic field where the cyclotron frequency is approximately 100 times higher than the applied RF frequency. This comes around a few hundred Gauss corresponding to applied RF frequency of a 13.56 MHz [21,30,34,35]. However, it has been observed that even at the low magnetic field [36,37] (approximately 50 Gauss) plasma production is equally efficient through a different mechanism than conventional helicon plasma production at the high magnetic field (few hundred Gauss). This kind of operation of helicon source is definitely more useful in many applications. In addition, most of the helicon studies have been performed with uniform static magnetic fields near the antenna. What happens when the magnetic field near the antenna is nonuniform? It has been previously observed that the non-uniform magnetic field plays an important role in helicon plasma production [38], i.e., the original efficiency of the helicon source can be further raised when the helicon wave is launched into a non-uniform magnetic field. However, the study of this source needs more attention when the non-uniform magnetic field is placed close to helical antenna. One of the objectives of this thesis is to address this issue of the non-uniform magnetic field near antenna with respect to the plasma production.

Another area the thesis wants to concentrate is about the downstream physics. Two phenomena related to downstream physics relevant to the present thesis are thrust generation and production of a double layer. It is observed that the hollow density profile generated in the expanding plasma in non-uniform (diverging) magnetic field causes a reduction of total thrust [39–42]. However, the role of a diverging magnetic field in the downstream plasma for the creation of hollow density formation is not comprehensively addressed. This forms another objective of the thesis, which is the physics of hollow density profile.

There has been considerable interest in the formation of current-free double layers in low-pressure RF-driven plasmas and their application to plasma thrusters for space propulsion. Hence a study of the formation of current free double layer and the physics related to ion and electron dynamics has its own importance. In most of the work, the existence of CFDL is manifested by the presence of ion beams in downstream of CFDL [43–47]. However, understanding of electron dynamics is also equally important to fully understand the behavior of CFDL. Hence, the final objective of the thesis is to study current free double layer (CFDL) with respect to the electron dynamics in expanding helicon plasma.

To summarize, the objectives of the thesis are the followings:

1. To understand the role of a non-uniform magnetic field near the antenna for plasma production efficiency.
2. To understand the physics behind the downstream hollow density profile for diverging magnetic field configuration in the expansion zone.
3. To study the relationship between the current free double layer and electron dynamics in the diverging magnetic field configuration in the expansion zone.

1.3 Review of relevant previous works

Plasma in the presence of non-uniform magnetic field is studied extensively in both astrophysical [48] and laboratory plasmas [18,20,39,49]. For example, plasma flow along the non-uniform magnetic field leading to magnetic reconnection is a well-known astrophysical phenomenon [50]. In another example, the presence of an external non-uniform magnetic field of tokamaks leads to different kinds of drifts, instabilities, and diffusions, which in turn, affect the confinement and transport mechanisms [51,52]. In the presence of a non-uniform magnetic field, the propagation and absorption mechanisms of plasma waves are very different than in the uniform magnetic field [38].

Helicon plasmas are considered to be very efficient sources for high-density plasma generation. There are at least two ways to further raise the efficiency of the helicon plasma source. First, the use of specially designed antennas like spiral [53] or phased antennas [54] which give a directional plasma production and raise the plasma density further. Another efficient way of increasing the plasma density is the operation of helicon discharge in a non-uniform but low magnetic field near the antenna. Here, a low magnetic field means that the electron cyclotron frequency (ω_{ce}) is equal to 5-10 times of the source frequency (ω_{rf}). It implies that operation using 13.56 MHz source frequency requires 20-40 G external magnetic field. The magnetic field configuration is a powerful means for the maximization of the plasma production of helicon plasma source, at fixed input power. It could be due to the alteration in the wave propagation and absorption rather than to particle confinement [55]. Few researchers [38,56–62] have observed an increase in the plasma density when non-uniform or cusp [58] magnetic field is present near the helicon antenna. The first observation of the plasma density enhancement in the non-uniform magnetic field is reported by Chevalier et al. [58] in a discharge generated by azimuthal mode, m = +1 of helicon wave. They reversed the current in the end coils to produce, a cusped magnetic field and they observed a density increase by a few times. No explanation was put forward for this kind of observation. Later, Guo et al. [62] carried out experiment with Nagoya type III antenna. For non-uniform case the magnetic field at the center of the antenna was maintained around few tens of Gauss with an axial gradient while for uniform case the magnetic field was maintained around ~900 Gauss. Measurements of axial plasma density profiles in uniform and non-uniform magnetic field were done and it was found that averaged densities were slightly higher for the non-uniform magnetic field case than for uniform magnetic field case for the same coupled power. They suggested that the “wider range of local phase velocity down to thermal values near the antenna region for the non-uniform magnetic field case could give rise to more efficient heating and acceleration of electrons and production of higher density plasma than the uniform case" [62]. Braginskii et al. used m = 0 antenna and switched off end coil to produce a non-uniform magnetic field near the antenna. They varied the magnetic field near the antenna from zero Gauss to 170 Gauss with same magnetic field gradient scale length. They observed that for non-uniform magnetic field case the density increased by a factor of three to five at a distance of 4.5 to 22 cm from the antenna in comparison to uniform magnetic field case. They showed that in a non-uniform magnetic field, the helicon phase velocity approaches the thermal velocity of electrons, enabling the trapping of the electrons in the longitudinal field of the helicon wave which causes their acceleration by Landau damping mechanism. Virko et al.[38] and Shamrai et al.[55] also observed the increase in density under the influence of non-uniform magnetic field near the antenna. They suggested that in the case of non-uniform (converging) magnetic field, the deep power deposition by helicon wave and high electron heat conduction along the magnetic field lines lead to the formation of hot electron layer which in turn improves the plasma production. Grulke et al. [63] used m = 1 helicon antenna, they switched off magnet coils near the antenna (source chamber) to create the gradient in the magnetic field near the antenna. They found a slight increase in plasma density and it was explained by a simple plasma contraction mechanism along the magnetic field lines that converged to the discharge axis. Ganguli et al. [64] and Sahu et al. [65] have used the non-uniform (mirror) magnetic field configuration near the two loop antennas to perform the study of propagation and absorption mechanism in helicon discharge but do not specifically talked about the effect of non-uniform magnetic field on propagation and absorption characteristics. Since, their work is more concentrated about to detection of hot or warm electrons, therefore they have used the mirror or non-uniform magnetic field configuration to confine the warm electrons. Also, their works do not discuss the plasma production efficiency in the non-uniform magnetic field configuration.

Spatially decreasing magnetic field, i.e. diverging or non-uniform magnetic field are widely used to expand the plasma into the etching reactors. This type of magnetic structure also causes plasma acceleration, which can be utilized for electric propulsion devices [18]. In the last few decades, the helicon sources have been recognized for their importance in the space propulsion. Helicon plasma source with diverging magnetic (or non-uniform) field configuration attracts increasing interest due to its potential application in plasma thruster [18,19]. In such devices, the efficiency of thrust generation does not only depend on the efficient plasma production but also on the radial profiles of plasma density and temperature within the region of the diverging magnetic field (magnetic nozzle). The radial profiles (plasma density and electron temperature) within the magnetic nozzle have been studied experimentally [42,49,66] and are found to depend substantially on the generation of diamagnetic current, Hall current, and the additional ionization in the diffusion chamber. In the magnetic nozzle geometry, one of the interesting aspects observed and which is also supported by particle-in-cell simulation [41] is that a hollow density profile is generated in the expansion chamber [39,40,67]. The formation of hollow density profile within a diverging magnetic field configuration is shown to have an effective loss mechanism of total thrust [42]. In the helicon plasma source with expanding plasma geometry and diverging magnetic field, an off-axis energetic electron component has been observed experimentally [39,67]. They are speculated to have a role in the formation of the hollow density profile by off-axis ionization. The formation of the hollow density structure is also explained in an alternative manner by the radial transport of plasma induced by the radial electric field generated due to the magnetized electrons and unmagnetized ions in the expansion chamber [40,41]. In this mechanism, an azimuthal current is proposed to be driven by the E×B drift (Hall current) which in presence of the axial magnetic field causes radially outward plasma transport. This explanation has been supported by experiment [40] and particle-in-cell simulation [41].

1.4 Outline of the thesis

This thesis deals with the efficient plasma production by helicon wave in a non-uniform magnetic field near the antenna center. Experiments are carried out with different non-uniformity of magnetic field near the antenna keeping the magnetic field at the center of the antenna < 100 G. This thesis also deals with the annular plasma formation downstream by magnetic divergence, in particular, the role of $\nabla \mathbf{B}$ drift and ion magnetization in the formation of radial density profile in magnetically expanding helicon antenna produced plasma keeping the source magnetic field > 100 G. The chapters of the thesis are organized as follows.

In chapter 2, the theory of helicon wave in radially uniform and non-uniform density plasma is discussed. The theoretical description of cold plasma dielectric tensor is discussed followed by a description of propagation of wave parallel to a magnetic field. Whistler wave dispersion is derived from the R-wave dispersion. The derivation of helicon waves for radially uniform density cylindrical plasma is derived where the solutions are in the form of Bessel's functions. A second wave exists when finite electron mass is included. This is known as the Trivelpiece- Gould (TG) mode. For radially non-uniform density distribution, the second-order differential equation of wave field solved numerically because the equation becomes non-linear and complex enough. The power coupling mechanism is also discussed in this chapter.

In chapter 3, details of Helicon eXperimental (HeX) system and implemented diagnostics are discussed. Various electric and magnetic probes with their data analysis techniques are discussed. The characterization of conventional helicon mode is performed by the mode transition method.

In chapter 4, efficient plasma production by helicon wave in a non-uniform magnetic field near the antenna center is discussed. Experiments are carried out with different non-uniformity of the magnetic field near the antenna keeping the magnetic field at the center of the antenna < 100 G. Coupling efficiencies are studied by measuring antenna current with and without plasma. Plasma production efficiencies are also estimated in all the different magnetic field topologies. It has been observed that coupling efficiency increases with magnetic field non-uniformity. Observation of beat wave in the axial variation of the axial wave magnetic field suggests the presence of different radial wave mode. Measurements of axial wavenumber along with the estimation of radial wavenumber suggest wave propagation near resonance cone, causing more absorption. It is found that the density obtained by introducing non-uniform magnetic field results in higher density than conventional helicon. The wavelength is measured for a nonuniform magnetic field near the antenna when the magnetic field is kept at 25 G and 50 G at the antenna center. For the 25 G case, the measured axial wavelength is found to be twice the length of the antenna. This suggests that half-wavelength antenna excites full wavelength helicon wave. However, in the 50 G case, the measured wavelength is shown to be approximately equal to the antenna length.

In Chapter 5, downstream hollow density profile and off-axis heating of electrons are discussed. In the Helicon eXperimental (HeX) device, the geometric aperture is fixed, but the position of the magnetic expansion or divergence can be varied. A hollow density is formed downstream, always in front of the magnetic divergence. This occurs irrespective of the relative position of the geometric expansion. This is in contrast to the earlier proposition made by others that a radial electric field is necessary to produce a hollow plasma profile. Instead, the ionization of neutrals in the radially outer region by the tail electrons, rotating fast due to gradient-B drift in the azimuthal direction, seems to account for the observed off-axis density peaking in the present experiment. Experiments are further performed to study in detail the hollowness within the magnetic divergence. The density profile in the magnetic divergence is seen to be modified from centrally peaked to hollow nature as the external magnetic field is varied. It occurs above a characteristic field value when the ions become magnetized in the expansion chamber. The density profile in the source chamber behind the magnetic divergence, however, remains peaked on-axis irrespective of the magnetic field. The electron temperature there is observed hollow, and this nature is carried to the expansion chamber along the field line. In the electron energy distribution near the off-axis peak location, a high energy tail exists. Rotation of these tail electrons in the azimuthal direction due to the gradient-B drift in the expansion chamber leads to an additional off-axis ionization and forms the hollow density profile. It seems if the ions are not magnetized, then the off-axis produced additional plasma is not confined and the density profile retains the on-axis peaked nature. The present chapter discusses how the knowledge of the ion magnetization together with tail electrons may significantly contribute to the design of an efficient helicon plasma-based thruster.

Chapter 6 discuss the electron energy distribution of current free double layer. The helicon plasma source with expanding plasma geometry sustain a large potential drop locally. The formation of CFDL and consequential ion acceleration in geometrically and magnetically expanding rf plasmas are the subject of intense research since this type of system is useful for the development of plasma propulsive device. The measurements of electron energy probability functions (EEPF) are performed in HeX in presence and absence of double layer. The double layer vanishes when the magnetic expansion is far away from the geometric expansion. The upstream measurement of EEPF in the presence of CFDL shows the depleted electron energy distribution above the break energy. This break energy corresponds to CFDL potential drop. The electrons having energy less than the break energy are trapped between the CFDL and sheath at the insulating source end wall. The electron having higher energy than the break energy overcomes the double layer and act as a free electron.

Finally, in Chapter 7, conclusion and future scope are presented.

References

[1] Stenzel R L 1999 Whistler waves in space and laboratory plasmas *J. Geophys. Res. Sp. Phys.* **104** 14379–95

[2] Chen F F 1996 Physics of helicon discharges *Phys. Plasmas* **3** 1783

[3] Aigrain P 1961 Proceedings of the International Conference on Semiconductor Physics, Prague (Czechoslovak Academy of Sciences) pp 224–7

[4] Bowers R, Legendy C and Rose F 1961 Oscillatory Galvanomagnetic Effect in Metallic Sodium *Phys. Rev. Lett.* **7** 339–41

[5] Klozenberg J P, McNamara B and Thonemann P C 1965 The dispersion and attenuation of helicon waves in a uniform cylindrical plasma *J. Fluid Mech.* **21** 545–63

[6] Lehane J A and Thonemann P C 1965 An experimental study of helicon wave propagation in a gaseous plasma *Proc. Phys. Soc.* **85** 301–16

[7] H. A. Blevin and P. J. Christiansen 1966 Propagation Of Helicon Waves In A Non-Uniform Plasma *Aust. J. Phys.* **19** 501

[8] Boswell R W 1970 Plasma production using a standing helicon wave *Phys. Lett. A* **33** 457–8

[9] Perry A J 1991 The application of the helicon source to plasma processing *J. Vac. Sci. Technol. B Microelectron. Nanom. Struct.* **9** 310

[10] Boswell R W and Henry D 1985 Pulsed high rate plasma etching with variable Si/SiO 2 selectivity and variable Si etch profiles *Appl. Phys. Lett.* **47** 1095–7

[11] Stubbers R, Jurczyk B, Rovey J, Coventry M, Alman D and Walker M 2007 Compact Toroid Formation using an Annular Helicon Preionization Source *43rd AIAA/ASME/SAE/ASEE Joint Propulsion Conference & Exhibit* (Reston, Virigina: American Institute of Aeronautics and Astronautics)

[12] Masters B C, Gray T K, Ruzic D N and Stubbers R 2005 Magnetic and Thermal Characterization of An ELM Simulating Plasma (ESP) With Helicon Pre-Ionization *21st IEEE/NPS Symposium on Fusion Engineering SOFE 05* (IEEE) pp 1–4

[13] Loewenhardt P, Blackwell B, Boswell R, Conway G and Hamberger S 1991 Plasma production in a toroidal heliac by helicon waves *Phys. Rev. Lett.* **67** 2792–4

[14] Prater R, Moeller C P, Pinsker R I, Porkolab M, Meneghini O and Vdovin V L 2014 Application of very high harmonic fast waves for off-axis current drive in the DIII-D and FNSF-AT tokamaks *Nucl. Fusion* **54** 083024

[15] Paul M K and Bora D 2009 Current drive by helicon waves *J. Appl. Phys.* **105** 013305

[16] Wang S J, Kwak J G, Kim C B and Kim S K 2003 Observation of enhanced negative hydrogen ion production in weakly magnetized RF plasma *Phys. Lett. A* **313** 278–83

[17] Santoso J, Manoharan R, O'Byrne S and Corr C S 2015 Negative hydrogen ion production in a helicon plasma source *Phys. Plasmas* **22** 093513

[18] Takahashi K 2019 Helicon-type radiofrequency plasma thrusters and magnetic

plasma nozzles *Rev. Mod. Plasma Phys.* **3** 3

[19] Charles C 2009 Plasmas for spacecraft propulsion *J. Phys. D. Appl. Phys.* **42** 163001

[20] Longmier B W, Bering E A, Carter M D, Cassady L D, Chancery W J, Díaz F R C, Glover T W, Hershkowitz N, Ilin A V., McCaskill G E, Olsen C S and Squire J P 2011 Ambipolar ion acceleration in an expanding magnetic nozzle *Plasma Sources Sci. Technol.* **20** 015007

[21] Takahashi K, Charles C, Boswell R and Ando A 2013 Performance improvement of a permanent magnet helicon plasma thruster *J. Phys. D. Appl. Phys.* **46** 352001

[22] Chen F F 1991 Plasma ionization by helicon wave *Plasma Phys. Control. Fusion* **33** 339–64

[23] Molvik A W, Ellingboe A R and Rognlien T D 1997 Hot-Electron Production and Wave Structure in a Helicon Plasma Source *Phys. Rev. Lett.* **79** 233–6

[24] Chen F F and Blackwell D D 1999 Upper Limit to Landau Damping in Helicon Discharges *Phys. Rev. Lett.* **82** 2677–80

[25] Shamrai K P and Taranov V B 1996 Volume and surface rf power absorption in a helicon plasma source *Plasma Sources Sci. Technol.* **5** 474–91

[26] Shamrai K P and Taranov V B 1994 Resonance wave discharge and collisional energy absorption in helicon plasma source *Plasma Phys. Control. Fusion* **36** 1719–35

[27] Krämer M, Aliev Y M, Altukhov A B, Gurchenko A D, Gusakov E Z and

Niemi K 2007 Anomalous helicon wave absorption and parametric excitation of electrostatic fluctuations in a helicon-produced plasma *Plasma Phys. Control. Fusion* **49** A167–75

[28] Akhiezer A I, Mikhailenko V S and Stepanov K N 1998 Ion-sound parametric turbulence and anomalous electron heating with application to helicon plasma sources *Phys. Lett. A* **245** 117–22

[29] Breizman B N and Arefiev A V. 2000 Radially Localized Helicon Modes in Nonuniform Plasma *Phys. Rev. Lett.* **84** 3863–6

[30] Degeling A W, Jung C O, Boswell R W and Ellingboe A R 1996 Plasma production from helicon waves *Phys. Plasmas* **3** 2788–96

[31] Degeling A W and Boswell R W 1997 Modeling ionization by helicon waves *Phys. Plasmas* **4** 2748–55

[32] Ellingboe A R and Boswell R W 1996 Capacitive, inductive and helicon-wave modes of operation of a helicon plasma source *Phys. Plasmas* **3** 2797–804

[33] Shinohara S 2018 Helicon high-density plasma sources: physics and applications *Adv. Phys. X* **3** 1420424

[34] Zhao G, Wang H, Si X, Ouyang J, Chen Q and Tan C 2017 The discharge characteristics in nitrogen helicon plasma *Phys. Plasmas* **24** 123507

[35] Sharma N, Chakraborty M, Neog N K and Bandyopadhyay M 2018 Development and characterization of a helicon plasma source *Rev. Sci. Instrum.* **89** 083508

[36] Lafleur T, Charles C and Boswell R W 2010 Plasma control by modification of

helicon wave propagation in low magnetic fields *Phys. Plasmas* **17** 073508

[37] Chen F F , X Jiang, J D Evans G T and D A 1997 Low-field helicon discharges *Plasma Phys. Control. Fusion* **39**

[38] Virko V F, Shamrai K P, Virko Y V. and Kirichenko G S 2004 Wave phenomena, hot electrons, and enhanced plasma production in a helicon discharge in a converging magnetic field *Phys. Plasmas* **11** 3888–97

[39] Charles C 2010 High density conics in a magnetically expanding helicon plasma *Appl. Phys. Lett.* **96** 051502

[40] Saha S K, Chowdhury S, Janaki M S, Ghosh A, Hui A K and Raychaudhuri S 2014 Plasma density accumulation on a conical surface for diffusion along a diverging magnetic field *Phys. Plasmas* **21** 043502

[41] Rao S and Singh N 2012 Numerical simulation of current-free double layers created in a helicon plasma device *Phys. Plasmas* **19** 093507

[42] Takahashi K, Lafleur T, Charles C, Alexander P and Boswell R W 2011 Electron Diamagnetic Effect on Axial Force in an Expanding Plasma: Experiments and Theory *Phys. Rev. Lett.* **107** 235001

[43] Charles C 2007 A review of recent laboratory double layer experiments *Plasma Sources Sci. Technol.* **16** R1–25

[44] Plihon N, Chabert P and Corr C S 2007 Experimental investigation of double layers in expanding plasmas *Phys. Plasmas* **14**

[45] Sun X, Keesee A M, Biloiu C, Scime E E, Meige A, Charles C and Boswell R W 2005 Observations of ion-beam formation in a current-free double layer

Phys. Rev. Lett. **95** 1–4

[46] Charles C and Boswell R W 2004 Laboratory evidence of a supersonic ion beam generated by a current-free “helicon” double-layer *Phys. Plasmas* **11** 1706–14

[47] Charles C 2004 Hydrogen ion beam generated by a current-free double layer in a helicon plasma *Appl. Phys. Lett.* **84** 332–4

[48] Marsch E 2006 Kinetic Physics of the Solar Corona and Solar Wind Living Reviews in Solar Physics *Living Rev. Sol. Phys* **3**

[49] Takahashi K, Charles C, Boswell R and Ando A 2014 Effect of magnetic and physical nozzles on plasma thruster performance *Plasma Sources Sci. Technol.* **23** 044004

[50] Su Y, Veronig A M, Holman G D, Dennis B R, Wang T, Temmer M and Gan W 2013 Imaging coronal magnetic-field reconnection in a solar flare *Nat. Phys.* **9** 489–93

[51] Horton W 1999 Drift waves and transport *Rev. Mod. Phys.* **71** 735–78

[52] Scott B D 2002 The nonlinear drift wave instability and its role in tokamak edge turbulence *New J. Phys.* **4** 352

[53] Shinohara S and Tanikawa T 2004 Development of very large helicon plasma source *Rev. Sci. Instrum.* **75** 1941–6

[54] Miljak D G and Chen F F 1998 Helicon wave excitation with rotating antenna fields *Plasma Sources Sci. Technol.* **7** 61–74

[55] Shamrai K P, Shinohara S, Virko V F, Slobodyan V M, Virko Y V. and Kirichenko G S 2005 Wave stimulated phenomena in inductively coupled magnetized plasmas *Plasma Phys. Control. Fusion* **47** A307–15

[56] Virko V F and Virko Y V. 2019 Influence of Nonuniform Magnetic Field on the Helicon Discharge Excited by Various Antennas *Ukr. J. Phys.* **64** 223

[57] Takechi S and Shinohara S 1999 RF Wave Propagation in Bounded Plasma under Divergent and Convergent Magnetic Field Configurations *Jpn. J. Appl. Phys.* **38** L1278–80

[58] Chevalier G and Chen F F 1993 Experimental modeling of inductive discharges *J. Vac. Sci. Technol. A Vacuum, Surfaces, Film.* **11** 1165–71

[59] Mori Y, Nakashima H, Baity F W, Goulding R H, Carter M D and Sparks D O 2004 High density hydrogen helicon plasma in a non-uniform magnetic field *Plasma Sources Sci. Technol.* **13** 424–35

[60] Chang L, Hole M J, Caneses J F, Chen G, Blackwell B D and Corr C S 2012 Wave modeling in a cylindrical non-uniform helicon discharge *Phys. Plasmas* **19** 1–11

[61] Braginskii O V., Vasil'eva A N and Kovalev A S 2001 Helicon plasma in a nonuniform magnetic field *Plasma Phys. Reports* **27** 699–707

[62] Guo X M, Scharer J, Mouzouris Y and Louis L 1999 Helicon experiments and simulations in nonuniform magnetic field configurations *Phys. Plasmas* **6** 3400–7

[63] Grulke O, Stark A, Windisch T, Zalach J and Klinger T 2007 Plasma Profiles

in a Cylindrical Helicon Discharge with Converging Magnetic Source Field *Contrib. to Plasma Phys.* **47** 183–9

[64] Ganguli A, Sahu B B and Tarey R D 2011 Investigation of absorption mechanisms in helicon discharges in conducting waveguides *Plasma Sources Sci. Technol.* **20** 015021

[65] Sahu B B, Ganguli A and Tarey R D 2014 Warm electrons are responsible for helicon plasma production *Plasma Sources Sci. Technol.* **23** 065050

[66] Takahashi K, Charles C and Boswell R W 2013 Approaching the Theoretical Limit of Diamagnetic-Induced Momentum in a Rapidly Diverging Magnetic Nozzle *Phys. Rev. Lett.* **110** 195003

[67] Takahashi K, Charles C, Boswell R, Cox W and Hatakeyama R 2009 Transport of energetic electrons in a magnetically expanding helicon double layer plasma *Appl. Phys. Lett.* **94** 191503

Chapter 2
Theory of Helicon Wave

2.1 Introduction

The seed of helicon wave theory lies in the theory of whistler wave [1] which have been studied for more than a century. Whistlers are low-frequency right hand polarized electromagnetic waves and well known in the ionosphere. Helicon waves are bounded whistlers. The pure electromagnetic character of whistler waves is lost and becomes quasi-electromagnetic helicon when these waves are confined to a boundary. This permit helicons with both right and left-hand polarizations. The frequency of helicon waves ω lies between the ion cyclotron ω_{ci} and the electron cyclotron frequency ω_{ce} and well below the plasma frequency ω_{pe}, i.e. $\omega_{ci} \ll \omega \ll \omega_{ce} \ll \omega_{pe}$. Helicon research started in solids [2–5] and soon after that in gaseous plasma [6]. Klozenberg, McNamra, and Thonemann (KMT) [7] derived the detailed dispersion and attenuation of helicon waves in uniform cylindrical plasma bounded by a vacuum. Blevin and Christiansen obtained the dispersion in a cylindrical non-uniform plasma [8]. The interest in this topic subsided until Boswell [9] in 1970, found that helicon waves were unusually efficient in producing plasmas.

This chapter is about the theory of helicon waves in radially uniform and non-uniform density plasma. The theoretical description of cold plasma di-electric tensor is discussed, followed by dispersion of whistler and helicon waves. Since helicons are bounded whistler, derivation of the helicon wave under the assumption of uniform cylindrically bounded plasma is derived where solutions of helicon wave fields are in the form of Bessel's functions. When finite electron mass is considered expression shows second branch of dispersion along with the helicon wave mode. This second mode is called Trivelpeice-Goud (TG) mode. When non-uniform radial density distributions are considered, the second-order differential equation must be solved numerically because the equation becomes non-linear and complex enough that numerical solution only valid. The solutions for radial wave magnetic field components for different density profile are solved numerically. The wave profile becomes steeper with the sharpness of density profiles. The zero-crossing point of the azimuthal component(B_θ) progressively moves inward as density profile sharpens. This point also separates the inner or outer magnetic field patterns of helicon waves. It is well known that the helicon antenna produced plasma undergo different mode transitions. The RF discharge can be sustained by the electric field of capacitive, inductive, or wave mode. The RF power coupling mechanisms in these three discharge mode is also discussed.

2.2 Cold plasma Di-electric Tensor: Waves in infinite bounded plasma

Plasma can be considered as a dielectric medium with long-range electromagnetic forces leading to collective behavior for which a perturbation at one place in plasma can affect the plasma at another place. The motion of charged particles in the presence of electric and magnetic fields created by externally applied or self consistently generated sources of charge density, and current density makes the dynamics complicated. The dispersion relation is needed to understand the properties of plasma waves. The dispersion relation is an equation that relates the frequency of a wave to its wavenumber such that $v = \frac{\omega}{k}$ is the wave phase speed, $k = \frac{2\pi}{\lambda}$ is the wave number and λ is the wavelength, $\omega = \frac{2\pi}{f}$ is wave angular frequency and f is the wave frequency. In vacuum, for an electromagnetic wave this is simple, with $\frac{\omega}{k} = c$, thus allowing the complete determination of wavelength for a given frequency. Here c is the speed of light. However, in a complex medium like a magnetized plasma with collective behavior, the medium becomes anisotropic, and a detailed derivation of the dispersion relation is tedious. To analyze the problems of the wave propagation in plasmas, two different approaches can be used. In the first approach, the plasma is characterized as medium having either conductivity or a dielectric constant and the wave equation for this medium is derived from Maxwell's equations. In the presence of an externally applied magnetic field, the plasma is equivalent to an anisotropic dielectric medium characterized by a dielectric tensor. Maxwell's equations are solved simultaneously with the fluid equations describing the particle motions. In this thesis, the derivation of the cold plasma dielectric tensor is derived using the second approach. All the information about the propagation of a given wave mode is contained in the appropriate dispersion relation. Cold plasma is one in which the thermal velocities of the particles are much smaller than the phase velocities of the waves ($v_{th} \ll \omega/k$) [10].

The dielectric tensor (ε) contains a large amount of information of different wave modes. Consider the uniform plasma immersed in a uniform magnetic field. The range of frequency perturbation in which we are going to derive the expression for the plasma di-electric tensor, in which only electrons are responding and ions are at rest. Cold plasma wave equations are derived by electron equations of motion in the electromagnetic fields and Maxwell's equation [11,12]. The momentum equation gives the evolution of the current produced in the plasma due to the applied (or self-generated) electromagnetic fields, which in turn evolve following Maxwell's equations. The solutions of these self-consistent equations yield the normal modes.

The Maxwell equation in the presence of plasma are different than the vacuum, where the source terms ρ and J, charge and current density, are present. The Maxwell's equations

$$\boldsymbol{\nabla} \cdot \boldsymbol{E} = \frac{\boldsymbol{\rho}}{\boldsymbol{\epsilon_0}} \tag{2.1}$$

$$\boldsymbol{\nabla} \cdot B = \mathbf{0} \tag{2.2}$$

$$\boldsymbol{\nabla} \times E = -\frac{\boldsymbol{\partial} B}{\boldsymbol{\partial t}} \tag{2.3}$$

$$\nabla \times \boldsymbol{B} = \mu_0 \boldsymbol{J} + \frac{\mathbf{1}}{\boldsymbol{c^2}} \frac{\partial \boldsymbol{E}}{\partial t} \tag{2.4}$$

In the above equation $\mu_{0,}$ ϵ_0 are permeability and permittivity of free space, with c as the speed of light.

Taking the curl of Eq. 2.3 and substituting into Eq. 2.4 results in a wave equation:

$$\boldsymbol{\nabla} \times \boldsymbol{\nabla} \times \boldsymbol{E} = -\frac{1}{c^2} \frac{\partial^2 \boldsymbol{E}}{\partial t^2} - \mu_0 \frac{\partial \boldsymbol{J}}{\partial t} \tag{2.5}$$

The particle current $\boldsymbol{J}$ in the presence of a plasma wave is described by the conductivity tensor, $\overleftrightarrow{\boldsymbol{\sigma}}$, where

$$\boldsymbol{J} = -n_0 e \boldsymbol{v} = \overleftrightarrow{\boldsymbol{\sigma}}.\boldsymbol{E} \tag{2.6}$$

This defines the conductivity tensor $\overleftrightarrow{\boldsymbol{\sigma}}$ for a cold, magnetized plasma. The $\overleftrightarrow{\boldsymbol{\sigma}}$ is a macroscopic variable whose nature is determined by microscopic dynamics. Maxwell's equation states that $\boldsymbol{J}$ and the displacement current combine to act as a source of a magnetic field in the medium;

If the wave electric field is $\boldsymbol{E}$ varies as $e^{-i\omega t}$ and $\mu_0\varepsilon_0 = \frac{1}{c^2}$, then above Eq. 2.4 can be written as,

$$\boldsymbol{\nabla} \times \boldsymbol{B} = -\frac{\boldsymbol{i}\omega}{\boldsymbol{c}^2}\left(\boldsymbol{I} + \frac{\boldsymbol{i}}{\boldsymbol{\varepsilon}_0\omega}\overleftrightarrow{\boldsymbol{\sigma}}\right).\boldsymbol{E} \tag{2.7}$$

Where $\mathbf{I}$ is the identity matrix. It follows that all information about the macroscopic response of the medium to applied electric field is contained in the dielectric tensor, defined by

$$\overleftrightarrow{\boldsymbol{\varepsilon}} = \left(\boldsymbol{I} + \frac{\boldsymbol{i}}{\boldsymbol{\varepsilon}_0\omega}\overleftrightarrow{\boldsymbol{\sigma}}\right) \tag{2.8}$$

Using Eq, 2.8 into Eq 2.7,

$$\nabla \times \boldsymbol{B} = -\frac{\boldsymbol{i}\omega}{\boldsymbol{c}^2}\overleftrightarrow{\boldsymbol{\varepsilon}}.\boldsymbol{E} \tag{2.9}$$

To proceed to obtain a dispersion relation, again Fourier-analysis of Eq. 2.5 in time and space with a lookout for harmonic solutions like $v, B, E = v_0, B_0, E_0 e^{i(kx-\omega t)}$;

$$\boldsymbol{k} \times \boldsymbol{k} \times \boldsymbol{E} = -\frac{\boldsymbol{\omega}^2}{\boldsymbol{c}^2}\boldsymbol{E} - i\mu_0\omega\overleftrightarrow{\boldsymbol{\sigma}} \cdot \boldsymbol{E} \tag{2.10}$$

By substituting the Lorentz force into Newton's second law (neglecting collisions and pressure term as this is a cold plasma model), one obtains the equation of motion for the electrons,

$$\boldsymbol{m}_e\frac{d\boldsymbol{v}_e}{dt} = q_e(\boldsymbol{E} + \boldsymbol{v}_e \times \boldsymbol{B}) \tag{2.11}$$

Where m_e and q_e are the charge and mass of the electron and $v_e(r,t)$ its velocity. Solving for $\boldsymbol{v_e}$ in terms of the components of $\boldsymbol{E}$, and plugging into Eq. 2.6 allows one to determine the conductivity tensor elements.

Our goal is to obtain an expression for the current $\boldsymbol{J}$ in terms of the electric field, from which we can get the components of $\overleftrightarrow{\boldsymbol{\sigma}}$**.** This relationship can be obtained by finding the velocities of the electron in terms of the electric field from the equations of motion. The motion of an electron parallel to a static uniform magnetic field is governed by the equation of motion,

$$m_e \frac{d\boldsymbol{v_z}}{dt} = -e\boldsymbol{E_z} \tag{2.12}$$

The perpendicular equation of motion,

$$m_e \frac{d\boldsymbol{v_x}}{dt} = -e(\boldsymbol{E_x} + (\boldsymbol{v} \times \boldsymbol{B}_0)_{\boldsymbol{x}})$$

$$\frac{dv_x}{dt} = \frac{e}{m}\boldsymbol{E_x} - \boldsymbol{v}_y \omega_{ce} \tag{2.13}$$

$$m_e \frac{d\boldsymbol{v_y}}{dt} = -e\left(\boldsymbol{E_y} + (\vec{\boldsymbol{v}}_{\boldsymbol{e}} \times \overrightarrow{\boldsymbol{B}_0})_{\boldsymbol{y}}\right)$$

$$\frac{d\boldsymbol{v_y}}{dt} = -\frac{e}{m}\boldsymbol{E}_y - \boldsymbol{v}_x \omega_{ce} \tag{2.14}$$

The Eq. 2.13 and 2.14 combinely can be written as

$$\frac{d\boldsymbol{v}_\perp}{dt} = -\frac{e}{m}\boldsymbol{E}_\perp + \omega_{\boldsymbol{ce}} \times \boldsymbol{v}_\perp \tag{2.15}$$

Differentiating Eq. 2.15 with respect to time and substituting from Eq. 2.15 for $\omega_{\boldsymbol{ce}} \times \dot{\boldsymbol{v}}_\perp$ we obtain

$$\ddot{\boldsymbol{v}}_\perp + \omega_{ce}{}^2 \boldsymbol{v}_\perp = -\frac{e}{m}(\dot{\boldsymbol{E}}_\perp + \omega_{\boldsymbol{ce}} \times \boldsymbol{E}_\perp) \tag{2.16}$$

Let us write $\boldsymbol{E}_{\perp} = Re(\widetilde{\boldsymbol{E}}_{\perp} e^{-i\omega t})$ and $\boldsymbol{v} = \boldsymbol{v}_{\perp\boldsymbol{0}} + Re(\widetilde{\boldsymbol{v}}_{\perp} e^{-i\omega t})$, then Eq. 2.16 becomes

$$(\omega_{ce}{}^{2} - \omega^{2})\widetilde{\boldsymbol{v}}_{\perp} = -\frac{e}{m}(-\boldsymbol{i}\omega\widetilde{\boldsymbol{E}}_{\perp} + \omega_{ce} \times \widetilde{\boldsymbol{E}}_{\perp}) \tag{2.17}$$

Combining Eq. (2.12) and (2.17)

$$v = \boldsymbol{v}_{\perp 0} + Re(\overleftrightarrow{\boldsymbol{a}}.\tilde{E}^{-i\omega t}) \tag{2.18}$$

Where,
$$\overleftrightarrow{\boldsymbol{a}} = \frac{e}{m}\begin{pmatrix} \frac{i\omega}{\omega_{ce}^2 - \omega^2} & \frac{\omega_{ce}}{\omega_{ce}^2 - \omega^2} & 0 \\ \frac{-\omega_{ce}}{\omega_{ce}^2 - \omega^2} & \frac{i\omega}{\omega_{ce}^2 - \omega^2} & 0 \\ 0 & 0 & -\frac{i}{\omega} \end{pmatrix} \tag{2.19}$$

All information about the particle drift arising from the $\boldsymbol{E}_{\perp}$is contained in $\overleftrightarrow{\boldsymbol{a}}$**.**

In Eq. (2.18) the response of the electron to the wave field is given by the second term on the right side. This is the term on which we wish to concentrate, and we shall accordingly adopt the model in which the plasma is cold so that electrons have no random thermal motion, i.e., $\boldsymbol{v}_{\perp 0} = 0.$ Then the current $\boldsymbol{J}$ associated with the response to an electromagnetic wave of the electrons contained in the unit volume of the magnetized plasma

$$\boldsymbol{J} = -n_0 e\boldsymbol{v} = n_0 e\,\overleftrightarrow{\boldsymbol{a}}.\boldsymbol{E} = \overleftrightarrow{\boldsymbol{\sigma}}.\boldsymbol{E} \tag{2.20}$$

This defines the conductivity tensor $\overleftrightarrow{\boldsymbol{\sigma}}$ for cold, magnetized plasma.

The dielectric tensor $\overleftrightarrow{\boldsymbol{\varepsilon}}$ in Eq. 2.9 for cold magnetized plasma follows the Eq. 2.8, 2.20 and 2.19

$$\overleftrightarrow{\boldsymbol{\varepsilon}} = \begin{pmatrix} 1+\dfrac{\omega_{pe}^2}{\omega_{ce}^2 - \omega^2} & -i\dfrac{\omega_{ce}\omega_{pe}^2}{i\omega(\omega_{ce}^2 - \omega^2)} & 0 \\ i\dfrac{\omega_{ce}\omega_{pe}^2}{i\omega(\omega_{ce}^2 - \omega^2)} & 1+\dfrac{\omega_{pe}^2}{\omega_{ce}^2 - \omega^2} & 0 \\ 0 & 0 & 1-\dfrac{\omega_{pe}^2}{\omega^2} \end{pmatrix} \tag{2.21}$$

For farther calculation it is convenient to introduce Stix [11] notation considering the ions are at rest;

$$S = 1+\frac{\omega_{pe}^2}{\omega_{ce}^2 - \omega^2} \tag{2.22}$$

$$D = \frac{\omega_{ce}\omega_{pe}^2}{\omega(\omega_{ce}^2 - \omega^2)} \tag{2.23}$$

$$P = 1-\frac{\omega_{pe}^2}{\omega^2} \tag{2.24}$$

$$R = S + D \tag{2.25}$$

$$L = S - D \tag{2.26}$$

The dielectric tensor in this notation can be written as

$$\overleftrightarrow{\varepsilon} = \begin{pmatrix} S & -iD & 0 \\ iD & S & 0 \\ 0 & 0 & P \end{pmatrix} \tag{2.27}$$

Here we have calculated the cold plasma di-electric tensor by considering the electron dynamics govern by the equation of motion. This tensor governs the propagation of electromagnetic waves in the magnetized plasma.

2.3 Waves in cold magnetized plasma

Deriving the plasma dispersion relation means solving Maxwell's equations self consistently including the plasma currents due to the plasma particle motions. Eq. 2.10 can be written as

$$\boldsymbol{k} \times (\boldsymbol{k} \times \boldsymbol{E}) = -\frac{\omega^2}{c^2}\overleftrightarrow{\epsilon} \cdot \boldsymbol{E} \tag{2.28}$$

$$\left(\frac{\omega^2}{c^2}\overleftrightarrow{\boldsymbol{\epsilon}} + \boldsymbol{kk} - \boldsymbol{k^2 I}\right).\boldsymbol{E} = \boldsymbol{0} \tag{2.29}$$

$$\overleftrightarrow{\boldsymbol{D}}.\boldsymbol{E} = 0 \tag{2.30}$$

$$\text{Where } \overleftrightarrow{\boldsymbol{D}} = \frac{\omega^2}{c^2}\overleftrightarrow{\boldsymbol{\epsilon}} + \boldsymbol{kk} - \boldsymbol{k^2 I} \tag{2.31}$$

The normal modes of the system are given by the determinate of $\overleftrightarrow{\boldsymbol{D}}$**,**

$$\mathrm{Det}(\overleftrightarrow{\mathbf{D}}) = 0 \tag{2.32}$$

Eq. 2.32 is the basic dispersion relation, the wavevector k and frequency ω are related to each other by the components of the di-electric tensor, which themselves contain ω and parameter ω_{ce} and ω_{pe} which described the state of the plasma. The solution of Eq. 2.32 describe the electromagnetic waves that propagate in the cold magnetized plasma. It is remarkable that all this information can be obtained using only single-particle dynamics embodied in Eq. 2.12 and 2.15, with collective behavior described by simple summation over all the electrons in Eq. 2.20.

Now we shall find the useful definition of vector $\boldsymbol{n}$ as follows, whose magnitude is given by the refractive index and direction by wavevector $\boldsymbol{k}$**.**

$$\boldsymbol{n} = \frac{c\boldsymbol{k}}{\omega} \tag{2.33}$$

Eq. 2.29 can be written as

$$(\boldsymbol{nn} - n^2 + \overleftrightarrow{\epsilon}).\boldsymbol{E} = \boldsymbol{0} \tag{2.34}$$

If we use $\boldsymbol{\theta}$, the angle between the $\boldsymbol{B_0}$ and $\boldsymbol{n}$**,** and if we assume $\boldsymbol{n}$ to be in *x, z* plane, equation (2.34) can be written as

$$\begin{pmatrix} S-n_z^2 & -iD & \boldsymbol{n_x n_z} \\ iD & S-n^2 & 0 \\ \boldsymbol{n_x n_z} & 0 & P-n_x^2 \end{pmatrix} \begin{pmatrix} E_x \\ E_y \\ E_z \end{pmatrix} = 0 \tag{2.35}$$

With $$n_x = n \sin\theta$$

$$n_z = n \cos\theta$$

$$n^2 = n_x^2 + n_z^2$$

$$\begin{pmatrix} S-n^2\cos^2\theta & -iD & n^2\sin\theta\cos\theta \\ iD & S-n^2 & 0 \\ n^2\sin\theta\cos\theta & 0 & P-n^2\sin^2\theta \end{pmatrix} \begin{pmatrix} E_x \\ E_y \\ E_z \end{pmatrix} = 0 \tag{2.36}$$

The requirement for the non-trivial solution is that the determinant of the coefficients vanishes

$$(S\sin^2\theta + P\cos^2\theta)n^4 + [RL\sin^2\theta + PS(1+\cos^2\theta)]n^2 + PRL = 0 \tag{2.37}$$

The Biquadratic Eq. (2.37) can be written as

$$An^4 - Bn^2 + C = 0 \tag{2.38}$$

with

$$A = S\sin^2\theta + P\cos^2\theta \tag{2.39}$$

$$B = RL\sin^2\theta + PS(1+\cos^2\theta) \tag{2.40}$$

$$C = PRL \tag{2.41}$$

Eq. 2.37 or 2.38 is a biquadratic equation in n and solve for n^2

$$n^2 = \frac{B \pm \sqrt{B^2 - 4AC}}{2A} \tag{2.42}$$

The interesting features of the solution are resonance and cut-offs. Resonance is characterized by the phase velocity going to zero ($v_P = \omega/k \to 0$) which is equivalent to the index of refraction $n = ck/\omega$ tend to infinity. The wave energy is absorbed by the plasma at resonance points. Cut-off is defined by $n \rightarrow 0$. At these cut-off point, the wavelength tends to infinity and waves are reflected back.

From Eq. 2.42 the general resonance condition can be found by setting the denominator to zero;

$$2(S\, sin^2\theta + P\, cos^2\theta) = 0 \tag{2.43}$$

$$\tan^2\theta = -\frac{p}{s} \tag{2.44}$$

The general cut-off condition can be found by setting the $n = 0$

$$PRL = 0 \tag{2.45}$$

If the dispersion relation is used to make statements about waves propagation in a certain direction, it is more convenient to express the Eq. 2.37 in terms of the propagation angle θ. The dispersion relation Eq. 2.37 can also be written in the form of

$$\tan^2\theta = -\frac{p(n^2-R)(n^2-L)}{(Sn^2-RL)(n^2-P)} \tag{2.46}$$

From Eq. 2.46 the two special cases of perpendicular $\left(\theta = \frac{\pi}{2}\right)$ and parallel $(\theta = 0)$ wave propagation can be studied.

2.3.1 Parallel Propagation $(\boldsymbol{k} \parallel \boldsymbol{B_0}, \boldsymbol{\theta} = \boldsymbol{0})$

In this work, waves propagating perpendicular to the magnetic field are not investigated since whistler, or helicon waves are modes propagating parallel or with some angle to the magnetic field. So only wave propagation parallel to magnetic fields is considered.

For the parallel wave propagation case ($\theta = 0$), the numerator of Eq. 2.46 has to vanish, that is:

$$P(n^2 - R)(n^2 - L) = 0 \tag{2.47}$$

There are three possible solutions;

1. Plasma oscillation: $P = 0$

This is the simplest plasma motion with $P = 0$,

$$P = 1 - \frac{\omega_{pe}^2}{\omega^2} = 0 \tag{2.48}$$

Eq. 2.48 can be written as

$$\omega^2 = \omega_{pe}^2 \tag{2.49}$$

This is not propagating wave as group velocity is zero for the all the frequencies. It represents an oscillation at the electron plasma frequency ω_{pe}.

2. R-waves: $(n^2 - R) = 0$

The dispersion relation resulting from this root is

$$n^2 = \frac{k^2c^2}{\omega^2} = 1 - \frac{\omega_{pe}^2}{\omega(\omega - \omega_{ce})} \tag{2.50}$$

The resonance is now at the electron cyclotron frequency ω_{ce}. This wave is right hand circular polarized and thus couples to the electron gyration at ω_{ce}. There is cut-off at ω_R, but there is well propagating low-frequency wave in the range ($\omega < \omega_{ce}$) as shown in Fig. 2.1. This part of the R-wave is the only electromagnetic wave mode that propagates at low frequencies.

3. L-waves $(n^2 - L) = 0$

The dispersion relation of the L-wave has an only different sign in the denominator compared Eq. 2.50, but consequences are much more far-reaching

$$n^2 = \frac{k^2c^2}{\omega^2} = 1 - \frac{\omega_{pe}^2}{\omega(\omega + \omega_{ce})} \tag{2.51}$$

The L-wave does not have a cyclotron resonance with the electrons because it rotates in the opposite sense. As seen from the Eq. 2.44 the L-wave does not have a resonance for positive ω. If we included the ion motion in our treatment, the L wave would have been found to have a resonance at $\omega = \omega_{ci}$, since it would then rotate with ion gyration. For frequencies well above the ion cyclotron frequency, the magnetic field has no influence on the ion motion. Low-frequency L-wave is called ion whistler waves.

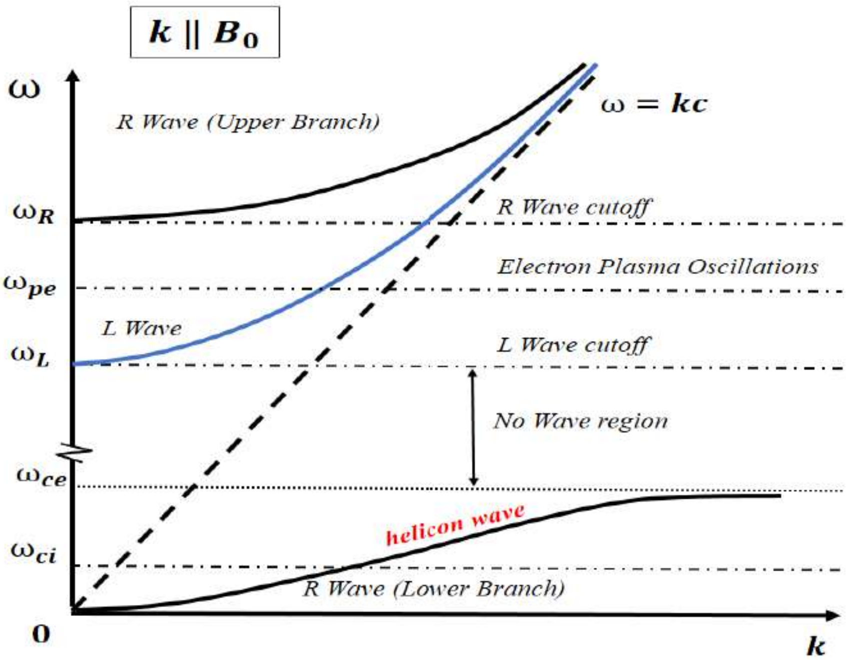

Fig. 2.1: Dispersion diagram of electromagnetic waves parallel to magnetic field showing the range of operation of Helicon waves in $\boldsymbol{\omega - k}$ diagram.

2.3.2 Whistler waves

Whistler waves are possibly one of the first wave plasma waves observed. These waves have been studied for more than a century. Early investigators [13,14] of radio emission from the ionosphere were rewarded by various whistling sound in the audio frequency range. The whistlers in the audio range in the northern hemisphere are caused by lightning in the southern hemisphere (and vice versa). These whistlers are guided by the Earth's magnetic fields, and the dispersion led to the detection of a declining tone which was heard as a whistle and hence the name whistler wave. The observation of the whistler wave led to the discovery of the existence of earth's magnetosphere and ionosphere [15]. In the ionosphere plasma, whistler waves can be used as a diagnostic tool to study the daily and annual evolution of density distribution, ion species composition, inhomogeneity ducts, etc. [1,15]. Whistler waves are right-hand circularly polarized electromagnetic waves (R-waves) in the frequency range between ion and electron cyclotron frequencies.

The R-wave dispersion Eq. 2.50 for parallel propagation simplifies at small frequencies of $\omega_{ci} \ll \omega \ll \omega_{ce} \ll \omega_{pe}$

$$n^2 = \frac{k^2c^2}{\omega^2} = \frac{\omega_{pe}^2}{\omega\omega_{ce}} \tag{2.52}$$

Above expression shows the dispersion relation for whistler waves and can be written as

$$\omega = \frac{c^2k^2\omega_{ce}}{\omega_{pe}^2} \tag{2.53}$$

The phase velocity

$$v_\phi = \frac{c}{n} = \frac{c^2 \omega_{ce} k}{\omega_{pe}^2} = c\sqrt{\frac{\omega\omega_{ce}}{\omega_{pe}^2}} \tag{2.54}$$

The group velocity

$$v_g = \frac{\partial\omega}{\partial k} = \frac{2c}{\omega_{pe}}\sqrt{\omega\omega_{ce}} \tag{2.55}$$

The group velocity ($\propto \sqrt{\omega}$) increases monotonically with increasing frequency. This means that high-frequency signals propagate faster than those with lower frequency.

2.3.3 Propagation at arbitrary angle

R-waves in unbounded plasmas do not necessarily have to propagate purely parallel to the external magnetic field. The angle between the wave vector k and the ambient magnetic field B_0 is called θ. Taking the Eq. 2.46, the dispersion reads similar to Eq. 2.50

$$n^2 = \frac{k^2 c^2}{\omega^2} = 1 - \frac{\omega_{pe}^2}{\omega(\omega - \ \omega_{ce}\cos\theta)} \tag{2.56}$$

The total wave vector is the sum of the perpendicular and parallel components $k^2 = k_\perp^2 + k_\parallel^2$ where $k, k_\parallel, and\ k_\perp$ are total, parallel and perpendicular wavenumbers. For parallel propagation ($\theta = 0$), the wave resonance frequency is again ω_{ce}, as previously derived for parallel R-wave propagation with no perpendicular component that is $k_\perp = 0$, which means $k = k_\parallel$. For increasing propagation angle, the resonance frequency decreases up to an angle $\theta_{res} = \cos^{-1}(\frac{\omega}{\omega_{ce}})$. Above θ_{res} there is no propagation possible. This means R-wave propagation restricted to a cone along the magnetic field with the angle θ_{res} called “resonance cone." This condition implies that the whistler wave is strongly guided by the ambient magnetic field. The wave is purely electromagnetic for parallel propagation and becomes purely electrostatic at the resonance cone angle whereas, at intermediate angles, the wave shows both characteristics.

In the frequency range $\omega_{ci} \ll \omega_{LH} < \omega < \omega_{ce} \ll \omega_{pe}$, of interest, taking $k^2 = k_\perp^2 + k_\parallel^2$ and $= \frac{k_\parallel}{k}$, the Eq. 2.56 can be written as

$$n^2 = \frac{k^2c^2}{\omega^2} = \frac{\omega_{pe}^2}{\omega(\omega_{ce}\cos\theta - \omega)} \tag{2.57}$$

The dispersion relation can be rearranged in terms of frequency,

$$\omega = \omega_{ce} cos\theta \frac{k^2c^2}{\omega_{pe}^2 + k^2c^2} \tag{2.58}$$

Two approximations can be derived from here. First, for short wave lengths $k \gg \omega_{pe}/c$,

$$\omega = \omega_{ce}\frac{k_\parallel}{k} \tag{2.59}$$

These waves are quasi-electrostatic and strongly damped. In helicon research, they are commonly referred to as slow mode waves or Trivelpiece-Gould modes, which are treated in the coming section. For long wave lengths, $k \ll \omega_{pe}/c$ one obtains helicon waves, and its dispersion relation becomes

$$\omega = \omega_{ce}\frac{k_\parallel k c^2}{\omega_{pe}^2} \tag{2.60}$$

As shown by Shamrai and Taranov [16], these two merge for a particular magnetic field. He finds a bi-quadratic equation by rewriting the Eq. 2.57 in term of perpendicular wave numbers,

$$k_{\perp\pm}^2 = k_{\parallel}^2 \frac{1}{2\alpha^2\beta^2}\left(1 - 2\alpha - 2\alpha^2\beta^2 \pm \sqrt{1-4\alpha}\right) \tag{2.61}$$

Where

$$\alpha = \frac{\omega_{pe}^2}{\omega_{ce}^2 N_{\parallel}^2}, \beta = \frac{\omega\omega_{ce}N_{\parallel}^2}{\omega_{pe}^2} \tag{2.62}$$

The slow-wave with $k_\perp = k_{\perp+}$ corresponds to TG wave and the fast wave with $k_\perp = k_{\perp-}$ corresponds to the helicon wave. They merge when $\alpha = 1/4$.

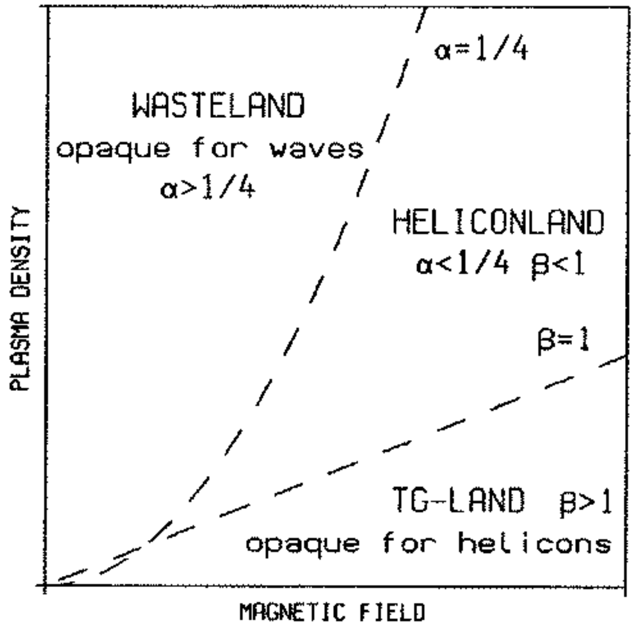

Fig. 2.2: Plasma density-magnetic field strength diagram showing the parameter space of Helicon and TG modes [16].

At low magnetic fields, the modes are indistinct, and at higher magnetic fields they are very much apart in perpendicular wave numbers. The TG modes have very short wavelengths and are confined to the plasma boundary. Fig. 2.2 shows the propagation regimes of TG and helicon modes, including the cut-off conditions in the density-magnetic field parameter space [16].

2.4 Helicon Waves in a cylindrical plasma: Uniform density

So far, we have described plasma waves that propagate in an unbounded medium. Now we will address bounded helicon waves. When the wave is bounded in either a conducting or dielectric boundary, we will see that the wave numbers are discrete and quantized. Consider a cylindrical plasma discharge of radius 'a', uniform radial density distribution $n_0(r) = n_0$, subject to an infinite homogenous magnetic field B_0 in the + $\mathbf{z}$ direction. Here we have assumed that the displacement current is neglected and the entire current carried by the $\boldsymbol{E} \times \boldsymbol{B}$ motion of electron where the driving frequency is much smaller than the electron cyclotron frequency $\omega \ll \omega_{ce}$ and much higher than lower hybrid frequency ($\omega > \omega_{LH}$) such that ion motion can be neglected. The Ohm's law expression to be evaluated is given by

$$\boldsymbol{E} = \frac{1}{en_0}\boldsymbol{J} \times \boldsymbol{B_0} \tag{2.63}$$

Returning to Maxwell's equations (2.3), (2.4) and Ohm's law (2.63), with a 1st order wave perturbations of the form $e^{i(m\theta+kx-\omega t)}$, simplifying the expression for the wave magnetic field such that,

$$i\omega\boldsymbol{B} = \nabla \times \boldsymbol{E} = \nabla \times \frac{1}{en_0}(\boldsymbol{J} \times \boldsymbol{B_0}) \tag{2.64}$$

$$i\omega \boldsymbol{B} = \frac{1}{en_0}(\boldsymbol{B_o}.\nabla)\boldsymbol{J} = \frac{ikB_0}{en_0}\boldsymbol{J} \tag{2.65}$$

$$\boldsymbol{J} = \frac{\omega e n_0}{kB_0}\boldsymbol{B} \tag{2.66}$$

Substituting in Eq. 2.67

$$\nabla \times \boldsymbol{B} = \mu_0 \boldsymbol{J} \tag{2.67}$$

$$\alpha \boldsymbol{B} = (\boldsymbol{\nabla} \times \boldsymbol{B}) \tag{2.68}$$

where α is defined as

$$\alpha = \frac{\omega}{k_z}\frac{n_0 \mu_0 e}{B_0} \tag{2.69}$$

which can be expressed in terms of the electron cyclotron frequency (ω_{ce}) and plasma frequency (ω_{pe}). α can be defined as total wavenumber.

$$\alpha = k_{total} = \frac{\omega \omega_{pe}^2}{k_z\, \omega_{ce} c^2} \tag{2.70}$$

The Eq. 2.70 is the same as for whistler wave propagation in free space.

Taking the curl of Eq. 2.68 yields a second-order differential equations for plasma wave fields,

$$\nabla^2 \boldsymbol{B} + \alpha^2 \boldsymbol{B} = 0 \tag{2.71}$$

The z component of the wave magnetic field in cylindrical coordinates is

$$\frac{\partial^2 B_z}{\partial r^2} + \frac{1}{r}\frac{\partial B_z}{\partial r} + \frac{1}{r^2}\frac{\partial^2 B_z}{\partial \theta^2} + \frac{\partial^2 B_z}{\partial z^2} = 0 \tag{2.72}$$

Applying the wave perturbation above equation reduces to

$$\frac{\partial^2 B_z}{\partial r^2} + \frac{1}{r}\frac{\partial B_z}{\partial r} + \left(T^2 - \frac{m^2}{r^2}\right) B_z = 0 \tag{2.73}$$

Where $T^2 = \alpha^2 - k_z^2$. Here T, α and k_z are the perpendicular, total and parallel wavenumbers.

The differential Eq. 2.73 is the Bessel's equation subject to finite boundary condition at the origin so that

$$B_z = AJ_m(Tr) + BK_m(Tr) \tag{2.74}$$

Where J_m is the Bessel function of the first kind. A and B are arbitrary constants. K_m is the Bessel function of second kind. $K_m(r)$ diverges at r =0 giving B=0.

$$B_z = AJ_m(Tr) \tag{2.75}$$

Similarly, the r and θ components of wave magnetic field are obtained from the Eq. 2.68 using the Eq. 2.75 as;

$$B_r(r) = \frac{iA}{T^2}\left(\frac{m\alpha}{r}J_m(Tr) - k_z J'_m(Tr)\right) \tag{2.76}$$

$$B_\theta(r) = \frac{A}{T^2}\left(\frac{mk_z}{r}J_m(Tr) + \alpha J'_m(Tr)\right) \tag{2.77}$$

With use of recursion relation 2.78

$$\frac{\boldsymbol{m}}{\boldsymbol{r}}J_m = \frac{T}{2}(J_{m-1} + J_{m+1}) \text{ and } J'_m = \frac{T}{2}(J_{m-1} - J_{m+1}) \tag{2.78}$$

Eq. 2.76 and 2.77 can be written as

$$B_r(r) = \frac{iA}{2T}[(\alpha + k_z)J_{m-1}(Tr) + (\alpha - k_z)J_{m+1}(Tr)] \tag{2.79}$$

$$B_\theta(r) = -\frac{iA}{2T}[(\alpha + k_z)J_{m-1}(Tr) - (\alpha - k_z)J_{m+1}(Tr)] \tag{2.80}$$

The boundary condition is the same for either a conducting or a dielectric boundary [12] requiring $B_r(r)|_{r=a} = 0$. This lead to the boundary condition as [12]

$$m\alpha J_m(Ta) - ak_z J'_m(Ta) = 0 \tag{2.81}$$

For given $\boldsymbol{k_z}, \boldsymbol{m}$ and density $\boldsymbol{n_0}$ and magnetic field $\boldsymbol{B_0}$ the $\boldsymbol{k_\perp or\ T}$ is set by the Eq. 2.81.

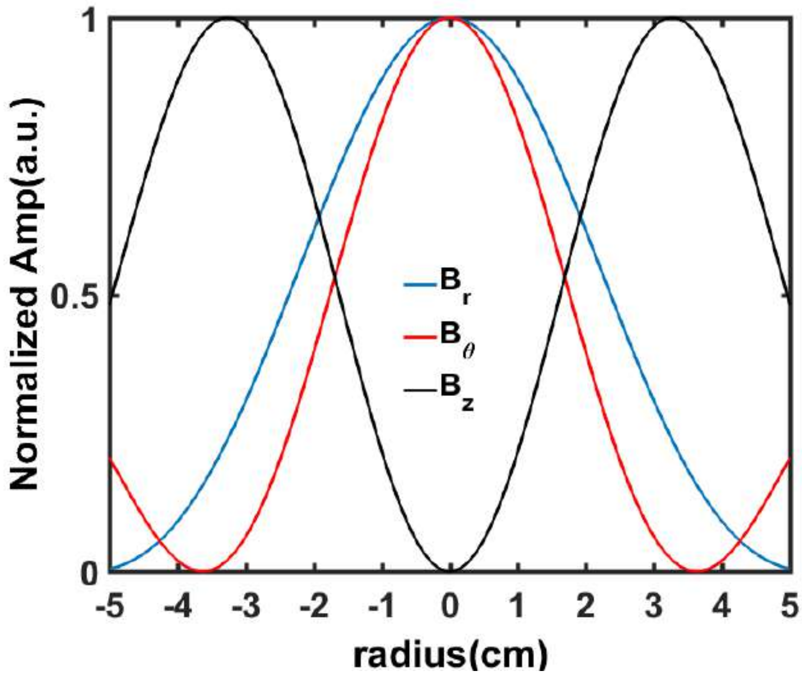

Fig. 2.3: Helicon wave magnetic field components at $6\times 10^{17} m^{-3}$, 100 G, f = 13.56 MHz, λ = 36 cm and a = 5 cm.

For example, given density at $6\times 10^{17} m^{-3}$, B_0= 100 G, f = 13.56MHz, λ = 36 cm (wavelength twice length of antenna length = 18 cm), m = +1, and a = 5 cm the value is about $k_\perp = 2.82\ cm^{-1}$. Fig. 2.3 shows the wave magnetic field component calculated for the above plasma parameters. Each component are normalized with respect to their own maximum value. The B_r component is zero at the radial boundary a = 5 cm.

2.5 Trivelpiece-Gould (TG) mode

The Maxwell's equations take on the following linearized form to derive the helicon-TG wave dispersion;

$$\nabla \times \boldsymbol{E} = i\omega \boldsymbol{B} \tag{2.82}$$

$$\nabla \times \boldsymbol{B} = \mu_0 J - i\mu_0 \omega \varepsilon_0 \boldsymbol{E} \tag{2.83}$$

Plasma current density neglecting small ion current density is given by Eq. 2.6,

$$\boldsymbol{J} = -n_0 e \boldsymbol{v_e}$$

where $\boldsymbol{v_e}$ is the electron velocity can be found using the following fluid equation

$$m_e n_0 \frac{d\boldsymbol{v_e}}{dt} = -n_0 e(\boldsymbol{E} + \boldsymbol{v_e} \times \boldsymbol{B_0}) + n_0 m_e \nu \boldsymbol{v_e} \tag{2.84}$$

Which is then converted with the current density ($\boldsymbol{J}$) equation using the equation 2.6 to find the wave electric field

$$\boldsymbol{E} = \frac{1}{en_0}\boldsymbol{J} \times \boldsymbol{B_0} - \frac{m_e \nu}{n_0 e^2}\boldsymbol{J} - \frac{m_e}{n_0 e^2}\frac{\partial \boldsymbol{J}}{\partial t} \tag{2.85}$$

Where *E, j and B* are perturbed quantity, and varying in the form $e^{i(m\theta + kx - \omega t)}$. The Eq. 2.85 can be rewritten in the form of Eq. 2.86

$$\boldsymbol{E} = \frac{1}{en_0}\boldsymbol{J} \times \boldsymbol{B_0} - \frac{im_e}{n_0 e^2}(\omega + i\nu)\boldsymbol{J} \tag{2.86}$$

Similar formulation to the previous section 2.4 can be achieved if one makes the electron mass zero in the second term of right-hand side of Eq. 2.86.

Taking the curl of Eq. 2.86 and substituting into the Eq. 2.82,

$$\nabla \times \boldsymbol{E} = \frac{\nabla \times \boldsymbol{J} \times \boldsymbol{B_0}}{n_0 e} - \frac{im}{n_0 e^2}(\omega + i\nu)\nabla \times \boldsymbol{j} = i\omega \boldsymbol{B} \tag{2.87}$$

Neglecting the displacement current and taking the curl of Eq. 2.83

$$\nabla \times \nabla \times \boldsymbol{B} = \mu_0 \nabla \times \boldsymbol{J} \tag{2.88}$$

Substituting into Eq. 2.88 into 2.87, yields

$$(\omega + i\nu)\boldsymbol{\nabla} \times \boldsymbol{\nabla} \times \boldsymbol{B} - \omega_{ce}\boldsymbol{k}\,\boldsymbol{\nabla} \times \boldsymbol{B} + \frac{\omega\omega_{pe}^2}{c^2}\boldsymbol{B} = 0 \tag{2.89}$$

Where $\omega_{ce} = \frac{eB_0}{m_e}$ and $\omega_p^2 = \frac{n_0 e^2}{m\varepsilon_0}$

Using the previous definition for $\alpha = \frac{\omega}{k}\frac{n_0\mu_0 e}{B_0}$ and defining the $\delta = \frac{\omega + i\nu}{\omega_{ce}}$.

Neglecting the collision for the time being, i.e., $\nu = 0$ and defining the $\delta_r = \frac{\omega}{\omega_{ce}}$.

The complex quantity δ can conveniently replace by its real part δ_r at any time if one wants to include the effect of the collisions. For the time being neglecting the collision and dropping the subscript "r" Eq. 2.89 can be rewritten as

$$\delta\boldsymbol{\nabla} \times \boldsymbol{\nabla} \times \boldsymbol{B} - k\,\boldsymbol{\nabla} \times \boldsymbol{B} + \alpha k\,\boldsymbol{B} = \boldsymbol{0} \tag{2.90}$$

When electron mass $m_e = 0$, the first term (highest-order term) vanishes and we are left with

$$\boldsymbol{\nabla} \times \boldsymbol{B} = \alpha\,\boldsymbol{B} \tag{2.91}$$

Which is similar to Eq. 2.68 of helicon mode only. Keeping the electron mass non-zero Eq. 2.90 can be factorized into

$$(\boldsymbol{\nabla} \times -\beta_1)(\boldsymbol{\nabla} \times -\beta_2)\boldsymbol{B} = \boldsymbol{0} \tag{2.92}$$

Where β_1 and β_2 are the roots of the algebraic equation.

$$\delta\beta^2 - k\beta + \alpha k = 0 \tag{2.93}$$

Then

$$\boldsymbol{B} = \boldsymbol{B_1} + \boldsymbol{B_2}, \quad \nabla \times \boldsymbol{B_1} = \beta_1 \boldsymbol{B_1}, \quad \nabla \times \boldsymbol{B_2} = \beta_2 \boldsymbol{B_2} \tag{2.94}$$

The solutions of quadratic Eq. 2.93 are

$$\beta_{1,2} = \frac{k}{2\delta}\left[1 \mp \sqrt{\left(1 - \frac{4\delta\alpha}{k}\right)}\right] \tag{2.95}$$

The square root terms have been Taylor series expanded for $k^2 \gg (\delta\alpha)^2$ and neglecting the higher-order term, the Eq. 2.95 can be written as

$$\beta_{1,2} = \frac{k}{2\delta}\left[1 \mp \left(1 - \frac{2\delta\alpha}{k}\right)\right] \tag{2.96}$$

Taking the 1st root with the minus sign

$$\beta_1 = \alpha = \frac{\omega}{k_z}\frac{n_0\mu_0 e}{B_0} \tag{2.97}$$

Here β_1 is the usual helicon root similar as Eq. 2.69.

Taking the second root with + sign and neglecting the

$$\beta_2 = \frac{k}{\delta} = \frac{k\omega_{ce}}{\omega} \tag{2.98}$$

The β_2 root is associated with electrostatic electron cyclotron waves called Trivelpiece-Gould modes, usually referred to as TG-waves. Fig. 2.4, $k-\beta$ diagram shows the existence and separation of helicon and and TG mode. Where, k is the axial wavenumber, and β is the total wavenumber. To plot the $k-\beta$ diagram, the Eq. 2.93 is simplified and written as

$$k = \frac{\omega}{\omega_{ce}\beta}\left(\beta^2 + \frac{\omega_p^2}{c^2}\right) \tag{2.99}$$

The $k-\beta$ diagram for various axial magnetic field strengths is plotted in Fig. 2.4

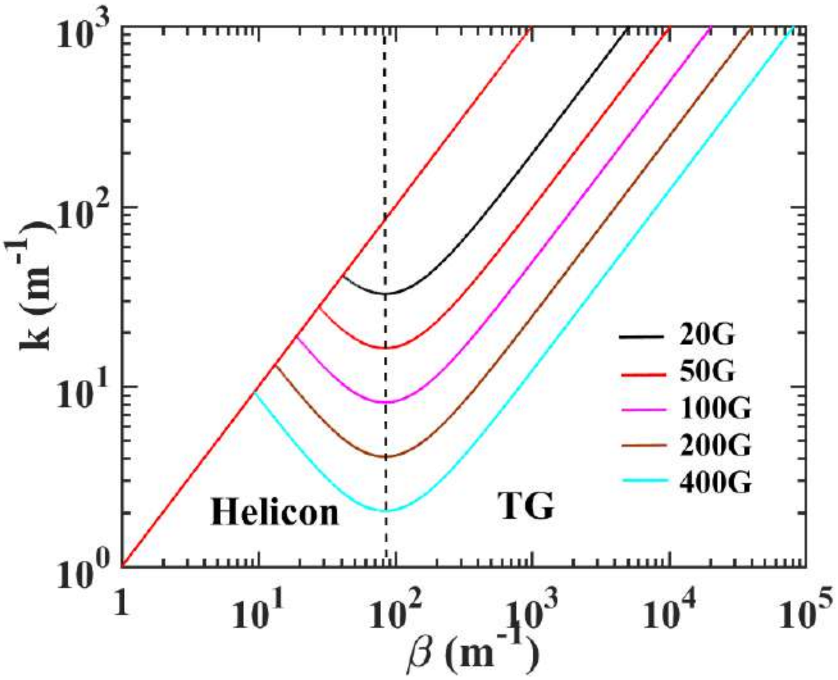

Fig. 2.4: Helicon-TG dispersion plots for different magnetic field values, keeping the operating frequency $f_{RF} = 13.56\ MHz$ and density $2 \times 10^{17} m^{-3}$. The vertical dash line separates the helicon and TG wave branch. The left side this dashed line represents the helicon wave, and the right side is the TG wave branch. Red line is $k = \beta$ line, which corresponds to pure helical with no perpendicular wavenumber. The solution on the left side of this yellow line does not exist.

2.6 Helicon in non-uniform radial density plasma

So far a uniform radial density distribution has been considered. In this subsection particular focus is dedicated to the calculation of wave magnetic field profile considering the non-uniform radial density distribution. Since plasma density is rarely uniform in the experiment, as it is in theory, we have reconsidered the helicon theory for radially non-uniform plasma. The effects of realistic non-uniform density profile are on both dispersion, and mode structures are considered.

The damping of the wave is again neglected in the following treatment to simplify the analysis. We consider the plasma in equilibrium to have an azimuthal symmetric ($\frac{\partial}{\partial\theta}$) density profile in a cylinder of radius a and uniform axial profile of magnetic field $\boldsymbol{B_z}$. The perturbation are of the form of $e^{i(m\theta+kx-\omega t)}$ so that m = +1 mode rotate clockwise when viewed along B_0, and $m = -1$ modes counterclockwise. The governing Maxwell's equations from 2.2 to 2.4 and 2.82 remain unaltered except that the displacement current will be included as;

$$\boldsymbol{\nabla} \times \boldsymbol{B} = \mu_0 \boldsymbol{J} + \frac{1}{c^2}\frac{\partial \boldsymbol{E}}{\boldsymbol{\partial t}} = \boldsymbol{\mu_0 J} - i\omega\mu_0\varepsilon_0 \boldsymbol{E} \tag{2.100}$$

Additionally Ohm's law Eq. 2.63 must change to include the radial density distribution according to

$$\boldsymbol{E} = \frac{1}{en_0(r)}\boldsymbol{J} \times \boldsymbol{B_0} \tag{2.101}$$

The analysis follows the exact formulation as the uniform density distribution except that some of the curl and vector, dot products must take into account the radial density component. Therefore, combining Maxwell's equations with Ohm's law yields

$$\alpha\boldsymbol{B} = (\boldsymbol{\nabla} \times \boldsymbol{B})_{\perp} + \gamma(\boldsymbol{\nabla} \times \boldsymbol{B})_{\boldsymbol{z}}\hat{\boldsymbol{z}} + \frac{i}{k}(k_0^2\, \boldsymbol{B} \times \hat{\boldsymbol{z}} - \alpha'(r)B_r\hat{\boldsymbol{z}}) \tag{2.102}$$

Here $\alpha(r) = \frac{\omega}{k}\frac{n_0(r)\mu_0 e}{B_0}$ and define $\gamma = 1 - \left(\frac{k_0}{k_z}\right)^2$ and $k_0 = \frac{\omega}{c}$

However, the uniform density equation can be recovered by neglecting the displacement current ($i.e. k_0/k_z \to 0$ since $v_{phase} \ll c$; which gives the $\gamma = 1$) and taking the constant radial density i.e. $\alpha'(r) = 0$. Returning to Eq. 2.102, neglecting the displacement current and assuming a constant density will give Eq. 2.68 as

$$\alpha \boldsymbol{B} = (\boldsymbol{\nabla} \times \boldsymbol{B})_{\perp} + (\boldsymbol{\nabla} \times \boldsymbol{B})_z = (\boldsymbol{\nabla} \times \boldsymbol{B}) \tag{2.103}$$

Separating the $r, \theta\ and\ z$ components of equation 2.102

$$\alpha B_r = \frac{im}{r} B_r - ik_z \gamma B_\theta \tag{2.104}$$

$$\alpha B_\theta = -{B_z}' - ik_z \gamma B_r \tag{2.105}$$

$$\alpha B_z = \gamma \left[\frac{1}{r}(rB_\theta)' - \frac{im}{r} b_r\right] - \frac{i}{k} \alpha'(r) B_r \tag{2.106}$$

Eliminating B_θ and B_r from above Eq. 2.104 and 2.105

$$\beta B_r = \frac{im}{r} \alpha B_z + ik_z \gamma {B_z}' \tag{2.107}$$

$$\beta B_\theta = -\alpha {B_z}' - \frac{m}{r} k_z \gamma B_z \tag{2.108}$$

Where

$$\beta = \alpha^2 - {k_z}^2 \gamma^2 \tag{2.109}$$

To obtain the differential equation for the plasma wave fields, Eq. (2.107) and (2.108) are substituted into (2.106) and reduced to

$${B_z}'' + f(r){B_z}'(r) + g(r)B_z(r) = 0 \tag{2.110}$$

Where

$$f(r) = \frac{1}{r} - \frac{2\alpha\alpha'}{\beta} \tag{2.111}$$

$$g(r) = \frac{\beta}{\gamma} - \frac{m^2}{r^2} - \frac{m}{k_z} \frac{\alpha'}{\gamma r}\left(1 + \frac{2{k_z}^2\gamma^2}{\beta}\right) \tag{2.112}$$

The above Eq. 2.110 is not in the form of Bessel equation as for uniform density. However, the same boundary conditions as before are utilized, namely, the wave field is finite at the origin, and the radial component $B_r(r = a) = 0$ vanishes on the boundary

[17]. If the plasma is surrounded by a di-electric so that we have the boundary condition $J_r = 0$, B_r vanishes at the plasma boundary because $\boldsymbol{J} \propto \boldsymbol{B}$ (from Eq. 2.67 and 2.102).

Therefore Eq. 2.107 can be evaluated for $B_r(r = a) = 0$

$$\frac{m}{a} B_z(r = a)\alpha(r = a) + k_z \gamma B_z{}'(r = a) = 0 \tag{2.113}$$

The radial density profiles studied for this analysis were given by

$$n(r) = n_0 \left[1 - \left(\frac{r}{f_a}\right)^s\right]^t \tag{2.114}$$

Where

$$f_a = \frac{a}{\left(1 - f_a{}^{\frac{1}{t}}\right)^{\frac{1}{s}}} \tag{2.115}$$

Taking various values of f_a, s and t the density profile can be generated. Fig. 2.5 shows the density profile for various values of t and keeping the same value for $f_a = 0.1$ and

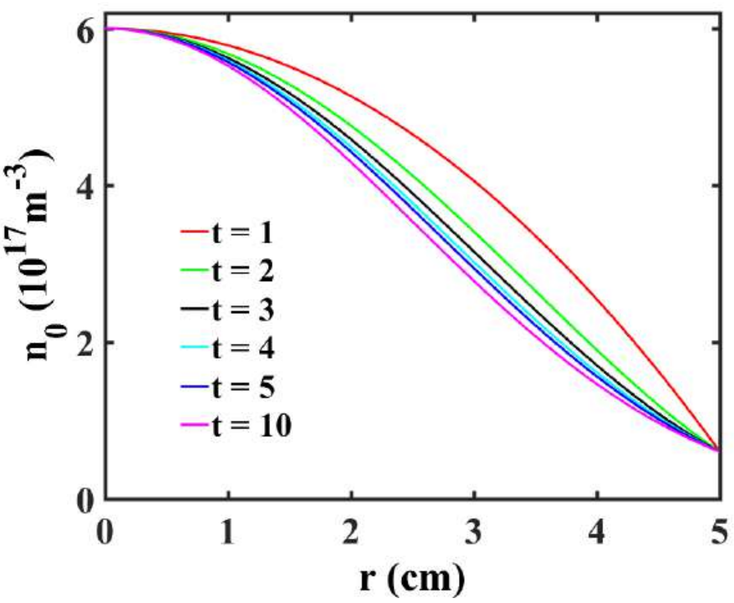

Fig. 2.5: Different density profile for various values of profile parameter t for $f_a = 0.1$ and $s = 2$. The peak density $n_0 = 6 \times 10^{17} m^{-3}$.

$s = 2$. It is clear from the Fig. 2.5 that the density profile becomes sharper as the value of t increases.

The following conditions are used to simulate the helicon wave field profiles of B_r, B_θ, and B_z according to Eq. 2.107, 2.108, and 2.110. The density $n_0 = 6 \times 10^{17} m^{-3}$, $B_0 = 100\ G, a = 5\ cm, f_{RF} = 13.56\ MHz$ and $m = +1$ mode. Since helical antenna excites the wavelength twice the length of the antenna. In our case, the antenna length is fixed, which is $l_{ant} = 18$ cm, the excited wavelength is about $\lambda = 36\ cm$, the corresponding wavenumber is k_z = 17.44 m^{-1}. The differential Eq. 2.110 was solved using Matlab ode solver for above mentioned parameters. The results of B_z from each radial density profile are given in Fig. 2.6.

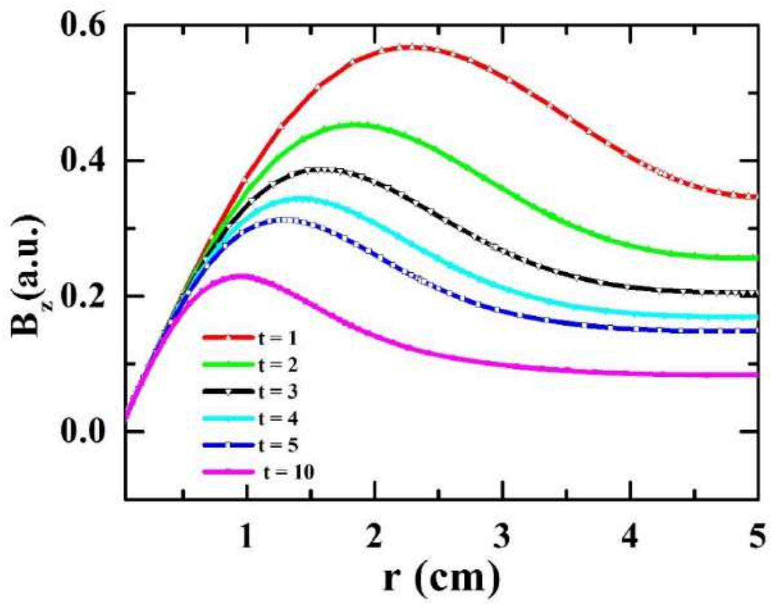

Fig. 2.6: B_z component of wave magnetic field for Fig. 2.5 density profiles. $B_0 = 100\ G, a = 5\ cm, f_{RF} = 13.56\ MHz$ and $m = +1$ mode, $k_z = 17.44\ m^{-1}$.

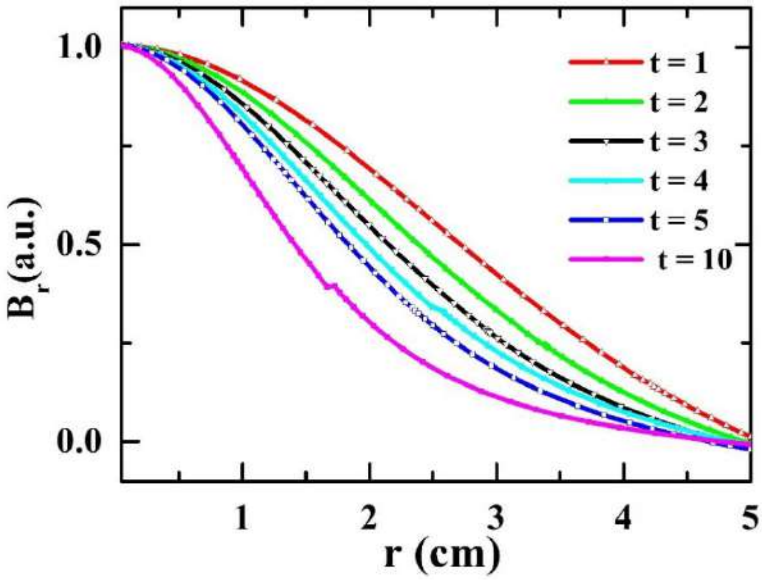

Fig. 2.7: B_r component of wave magnetic field for Fig. 2.5 density profiles. $B_0 = 100\ G, a = 5\ cm, f_{RF} = 13.56\ MHz$ and $m = +1$ mode, $k_z = 17.44\ m^{-1}$.

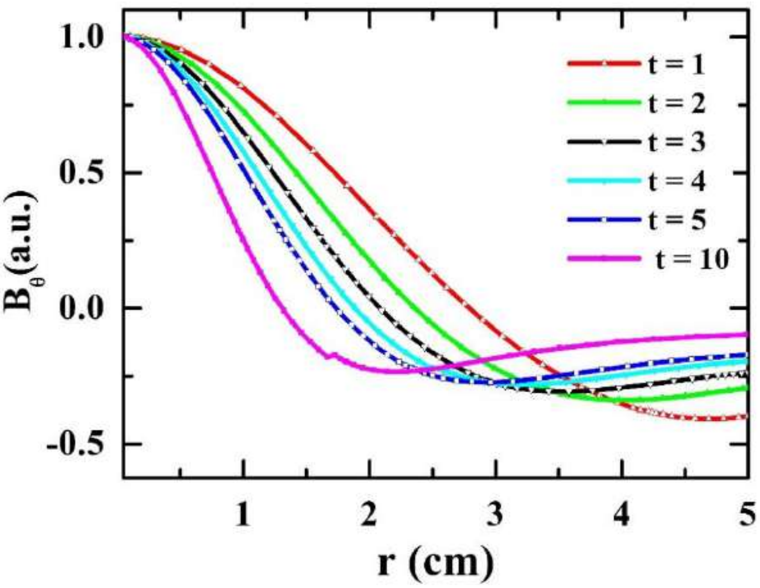

Fig. 2.8: B_θ component of wave magnetic field for Fig. 2.5 density profiles. $B_0 = 100\ G, a = 5\ cm, f_{RF} = 13.56\ MHz$ and $m = +1$ mode, $k_z = 17.44\ m^{-1}$.

The derivative of B_z was numerically solved in the same manner such that the remaining B_r and B_θ components could be solved according to (2.107) and (2.108). The results of B_r and B_θ components are shown in Fig. 2.7 and Fig. 2.8, respectively. The boundary condition is satisfied when B_z is solved for, namely, the radial component of the B_r field has to be zero for each profile, this is shown in Fig. 2.7. The Variations of B_z, B_r and B_θ for different density profiles are shown in Fig. 2.6 to Fig. 2.8. The the wave profile becomes steeper with the sharpness of density profiles. The zero-crossing point of the azimuthal component(B_θ) (Fig. 2.8) progressively moves inward as density profile sharpens. This point also separates the inner and outer magnetic field patterns of the helicon wave. The non-uniform density profile significantly affects the wave field pattern and hence, the energy deposition profile [17].

2.7 Power coupling in helicon discharge

The coupling of radio frequency (RF) power to the plasma in the helicon discharge is studied for the last several decades. Helicon discharges are well known for operation of three different discharge modes, namely capacitive (E), inductive (H) and wave (W) mode [18–21]. The E, H or W modes are named depending on the dominant electric field responsible for maintaining the discharge is of capacitive, inductive or wave nature, respectively. At low RF powers, there is a substantial amount of voltage across the antenna, so a capacitive current is driven in the plasma and a fraction of the discharge power is therefore deposited capacitively. The RF current flowing in the antenna induces electric field near the antenna that tends to excite an inductive mode. This inductive electric field drives the plasma current in order to oppose the magnetic field produced by the antenna current. At low density, the plasma is maintained by capacitive electric fields as skin depth is more so that the RF electric fields produced by high antenna voltage can couple directly. As the density is increased, the skin depth reduces and electromagnetic fields decay exponentially within a very thin layer of the plasma. Capacitive and inductive discharge do not need an external magnetic field. When an external magnetic field is applied to plasma, the dielectric of the plasma changes and can have normal modes which are of electromagnetic in nature. So, magnetized plasma allows certain frequencies depending upon parameters such as density and magnetic field for an electromagnetic wave to penetrate to the core of the plasma. The electric field of these electromagnetic waves can deposit energy through either collisional or collisional processes.

The discharge mode transitions in helicon discharge are observed by changing the operating parameters either by RF power [18–20] or external magnetic field[22,23]. At very low power and low magnetic field values, power is capacitively coupled to the plasma, and the mode of operation is known as the capacitive or E-mode. As power and magnetic field increases, the inductive electric field due to the oscillating current in the antenna adds to the ionization, and this inductive or H-mode of the operation increases the density in the edge region. Finally, when the density and magnetic field are high enough so that the helicon wave becomes a propagating normal mode of the plasma, addition power is being coupled through antenna wave field coupling to the helicon wave, and this is called the wave coupled or W-mode of operation.

2.8 Summary

Cold plasma dielectric tensor is derived from the equation of motion and Maxwell's equations. Whistler wave dispersion relation and its bounded version known as helicon wave dispersion relation are derived. Helicon wave field structure is calculated from generalized Ohm's law and Maxwell's equations. Finite electron mass effect is shown to give another solution as TG modes along with the normal quasi electromagnetic helicon modes. When non-uniform radial density distributions are considered, the second-order differential equation solved numerically because the equation becomes non-linear and complex enough that numerical solution only valid. The solutions for radial wave magnetic field components for different density profile are solved numerically. Mode transition in helicon discharge is explained for capacitive, inductive, and helicon wave mode.

References

[1] Stenzel R L 1999 Whistler waves in space and laboratory plasmas *J. Geophys. Res. Sp. Phys.* **104** 14379–95

[2] Aigrain P 1961 Proceedings of the International Conference on Semiconductor Physics, Prague (Czechoslovak Academy of Sciences) pp 224–7

[3] Legéndy C R 1964 Macroscopic Theory of Helicons *Phys. Rev.* **135** A1713–24

[4] Kanai Y 1963 Helicon Waves in PbTe *Jpn. J. Appl. Phys.* **2** 137–42

[5] Harding G N and Thonemann P C 1965 A study of helicon waves in indium *Proc. Phys. Soc.* **85** 317–28

[6] Lehane J A and Thonemann P C 1965 An experimental study of helicon wave propagation in a gaseous plasma *Proc. Phys. Soc.* **85** 301–16

[7] Klozenberg J P, McNamara B and Thonemann P C 1965 The dispersion and attenuation of helicon waves in a uniform cylindrical plasma *J. Fluid Mech.* **21** 545–63

[8] H. A. Blevin and P. J. Christiansen 1966 Propagation Of Helicon Waves In A Non-Uniform Plasma *Aust. J. Phys.* **19** 501

[9] Boswell R W 1970 Plasma production using a standing helicon wave *Phys. Lett. A* **33** 457–8

[10] Bittencourt J A 2004 *Fundamentals of Plasma Physics* vol 16 (New York, NY: Springer New York)

[11] Stix T H 1992 *Waves in Plasmas* vol 49

[12] Dendy R O 1990 *Plasma Dynamics*

[13] PREECE W H 1894 Earth Currents *Nature* **49** 554–554

[14] Barkhausen H 1930 Whistling Tones from the Earth *Proc. IRE* **18** 1155–9

[15] Al'pert Y 1980 40 years of whistlers *J. Atmos. Terr. Phys.* **42** 1–20

[16] Shamrai K P and Taranov V B 1996 Volume and surface rf power absorption in a helicon plasma source *Plasma Sources Sci. Technol.* **5** 474–91

[17] Chen F F, Hsieh M J and Light M 1994 Helicon waves in a non-uniform plasma *Plasma Sources Sci. Technol.* **3** 49–57

[18] Ellingboe A R and Boswell R W 1996 Capacitive, inductive and helicon-wave modes of operation of a helicon plasma source *Phys. Plasmas* **3** 2797–804

[19] Chi K K, Sheridan T E and Boswell R W 1999 Resonant cavity modes of a bounded helicon discharge *Plasma Sources Sci. Technol.* **8** 421–31

[20] Franck C M, Grulke O and Klinger T 2003 Mode transitions in helicon discharges *Phys. Plasmas* **10** 323–5

[21] Perry A J 1991 The application of the helicon source to plasma processing *J. Vac. Sci. Technol. B Microelectron. Nanom. Struct.* **9** 310

[22] Boswell R W 1984 Very efficient plasma generation by whistler waves near the lower hybrid frequency *Plasma Phys. Control. Fusion* **26** 1147–62

[23] Blackwell D D and Chen F F 1997 Two-dimensional imaging of a helicon discharge *Plasma Sources Sci. Technol.* **6** 569–76

s

Chapter 3
Experimental device, diagnostics, and helicon characterization

3.1 Introduction

The Helicon eXperimental (HeX) device is a linear plasma device which is developed for the study of, basic helicon plasma physics, waves and instabilities, plasma generation in a non-uniform magnetic field, profile formation from the point of view of helicon plasma thruster, and study of current free double layers. HeX device is capable to produce a wide range of plasma densities which vary from 10^{15} to 10^{18} m^{-3}. This can be done by adjusting various operating parameters such as the fill-in gas pressure, RF power, and applied magnetic field. In HeX, although plasma parameter can be controlled by various operating parameters, increasing the magnetic field non-uniformity in the source has a significant effect over plasma generation, which will be discussed in the next chapter. This chapter describes the different parts of the experimental apparatus and diagnostics that have been developed for measuring the plasma parameters. The diagnostics including Langmuir probe for the measurement of plasma density, electron temperature, plasma potential, floating potential and EEDF; emissive probe for direct measurement of the plasma potential and a magnetic field probe for wave amplitude and phase measurement. One of the specialties of the HeX device is the provision for varying the magnetic field non-uniformity in the source and expansion region; this is also discussed in this chapter along with the identification of helicon mode using the density mode transition.

This chapter is organized as follows; section 3.2 describes the subsystems of HeX. In section 3.3, implemented plasma diagnostics are discussed. Section 3.4 discusses the characterization of Helicon mode using the density mode transition.

3.2 Helicon eXperimental (HeX) device

The Helicon Experimental device (HeX) is a linear plasma device which consists of the vacuum chambers, electromagnets, a helical antenna, and RF generator and matching network. Details of each of these subsystems are described in the following subsections.

3.2.1 Vacuum vessel

The schematic of the linear helicon experimental (HeX) device is shown in Fig. 3.1. The vacuum system of HeX consists of a source and an expansion chamber. The plasma is produced in the source chamber and diffuses into the expansion chamber. The source chamber is made of the borosilicate glass tube and has a 9.5 cm inner diameter and 70 cm length. The left end of the source chamber is terminated by an insulating pyrex plate to make the plasma current free. The source tube needs to be made of insulator so that the electromagnetic fields produced from the antenna can penetrate inside the tube to interact with the plasma. The other end of the source tube is contiguously attached to a 51 cm long stainless steel (SS) expansion chamber of 21 cm inner diameter. The right end of the SS chamber is closed with the SS plate. Both the chambers are facilitated with few diagnostic ports through which the whole plasma can be diagnosed using various electric and magnetic probes.

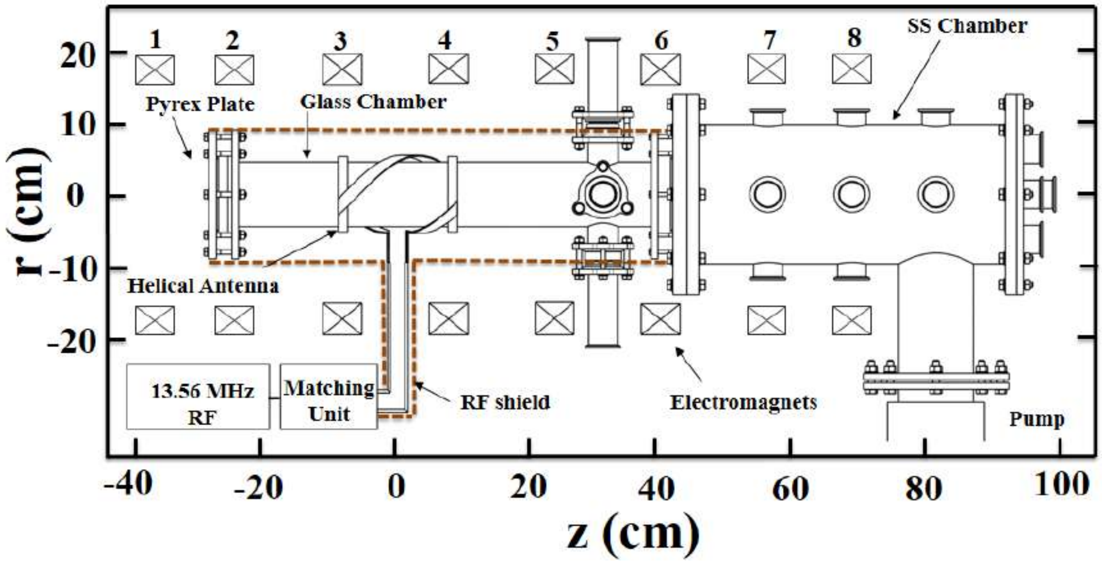

Fig. 3.1: Schematic of Helicon eXperimental (HeX) device.

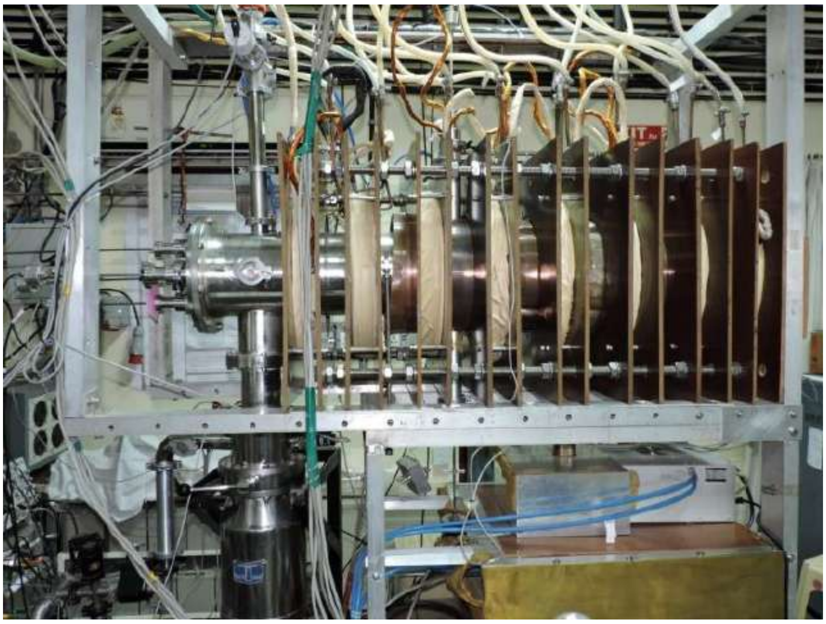

Fig. 3.2: Picture of Helicon eXperimental (HeX) device.

The whole chamber is evacuated to a base pressure of 1×10^{-6} mbar by a diffusion pump (1000 lit/sec pumping speed) connected to the bottom of the expansion chamber, backed by a rotary pump. The pressure is measured by two compact full-range pressure gauge model no. PKR 251 made by Pfeiffer-vacuum placed at the top of the expansion chamber. The positions of pressure gauges are chosen such that they will not be influenced by both the ambient magnetic field and the RF radiation. Argon gas is used for all the experiments and fed through using a gas-dosing valve (Pfeiffer make) which is connected to the side port of the expansion chamber, and allows fine changes in the gas pressure of the chamber. A picture of HeX is shown in Fig. 3.2.

3.2.2 Helicon Antenna

Various antennas can be used to produce the helicon plasma [1,2]. The helical antenna is the most economical antenna in the sense that the wave energy propagates mainly in one direction along the magnetic field [3]. The helical antenna is the best choice for an RF plasma source in which the antenna is to be located at one end of the plasma. This may be favorable for plasma application where the helicon plasma is injected into a reaction chamber. As a consequence, the discharge becomes axially asymmetric. Since helicon waveforms are helices that rotate in both space and time, power coupling to the wave is better with antennas that are themselves helices. As the half-wavelength antenna is shown to be more efficient than full wavelength antenna [4] and due to above mentioned features of the helical antenna, a right hand polarized half-wavelength m = +1 helical antenna is used for our experiments. In the direction of the magnetic field, helical antenna excites the helicon modes with positive azimuthal mode number m, whereas on the other side or in the reverse direction of magnetic field this antenna exites $m < 0$ mode. The postive or negative azimuthal mode corresponds to the right or left hand polarization convention of the wave propagtion which depends on the direction of the axial magnetic field and propagation wave vector $\boldsymbol{k}$ [2,5]**.** If positive $\boldsymbol{k}$ denotes the propagation along the magnetic field direction then right-hand polarization means ($m > 0$), the wave electric field vector rotate clockwise in time when viewed along the magnetic field direction [5]. The right hand helical or R antenna has 180^0 helical twist in horizontal legs in a counterclockwise direction when viewed along the magnetic field direction same as wave propagation direction. Conversely, if the legs are twisted in the clockwise direction along the $\boldsymbol{k}$ the antenna is called L or left helical antenna [2] . Plasma is produced by using the right helical antenna, having a length of 18 cm and diameter 12 cm, placed concentrically around the glass tube. Antenna is placed on two teflon spacers of about 3 mm thick at the antenna ends fixed from the outside of the glass tube. A right helical antenna is made using the copper (Cu) strips of width 2.5 cm and thikness 0.3 cm. Picture of the antenna is shown in Fig. 3.3.

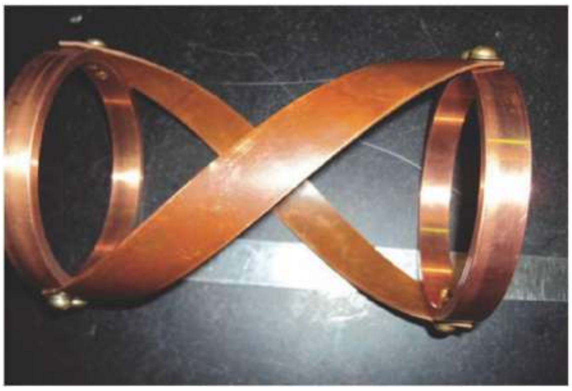

Fig. 3.3: Picture of the helical antenna of HeX.

3.2.3 RF generator and matching network

A fixed frequency 13.56 MHz RF power generator (CESAR^{TM} generator model 1325 Advance energy) is used to power the antenna. The water-cooled RF generator can supply RF power upto 2.5 kW with 1 W power variation and has a 50 Ohm characteristic output impedance. The forward and reflected powers are displayed at the control panel. Since the plasma typically has an impedance of the order of ≤ 2 ohms, while the rf power generator has a standard impedance of 50, a matching network is needed to adjust the antenna-plasma load for maximum power transfer. A commercial impedance matching network (type VM5000W) is employed to match the antenna-plasma load with RF source load. The impedance is adjusted by making use of the two vacuum variable capacitors and inductors placed in the matching box. The different experimental requirements can be fulfilled by the use of suitable inductors in series with the capacitors. Note that the antenna has a non-negligible inductance, which plays an important role in the matching of the antenna-plasma load. If the antenna-plasma load is not matched, then a significant amount of the input power is reflected back to the generator, which can result in damage to the generator and make the poor power transfer efficiency to the plasma also. When there is no plasma, the resistance is the electrical

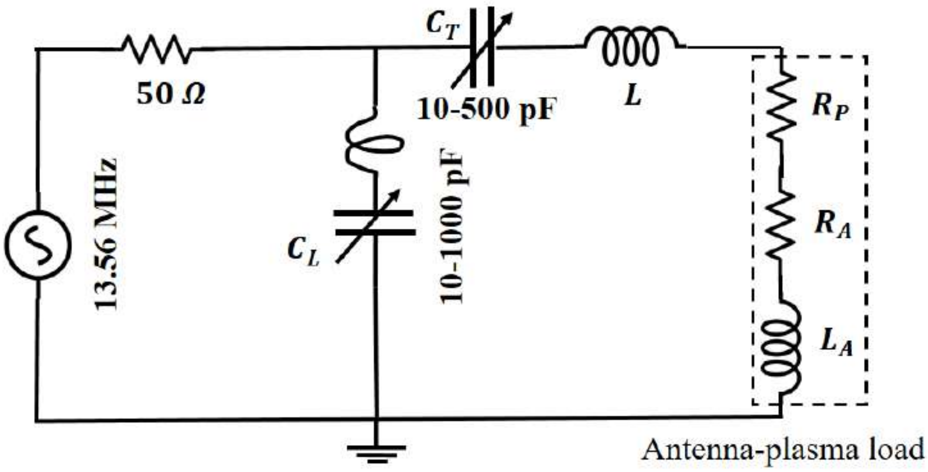

Fig. 3.4: Schematic of the L-type matching network attached to an RF generator and a load composed of the antenna and plasma.

resistance of the antenna. Once the plasma is formed, the resistance will increase. An L-type matching network (the equivalent circuit is shown in Fig. 3.4) is employed with two vacuum variable capacitors: one is load, and other is tune capacitor. The load capacitor (C_L) and tune capacitor (C_T) can be tuned from 10 to 1000 pF and 10 to 500 pF, respectively, so that zero reflection matching can be done for plasma resistance, R_P

= 0.1 Ohm to 2 Ohm. Both the capacitors are mounted inside the tuning box, which is made of silver-coated copper so that it acts as a Faraday cage. On the top side of the tuning box, a fan is mounted to ensure cooling for the two capacitors.

It is essential to shield the antenna, transmission line along with all interlocking from the source, to minimize undesired electromagnetic radiation falling onto the other equipment. A copper (Cu) sheet of 0.2 mm thickness has been chosen for the shielding purpose, as shown in Fig. 3.2. Initially, the brass mesh has been used for shielding purpose. However, the use of Cu sheet (thickness 0.2 mm) for our 13.56MHz RF source improved the RF shielding significantly compared to brass mesh. The radiation strength 30 cm away from the Cu enclosure is measured ~ 5 V /m using the power meter at power 500 W.

3.2.4 Electromagnets

Eight axisymmetric forced water-cooled electromagnet coils, shown in Fig. 3.1 are used to generate the axial magnetic field (B_0) in helicon experiments. These electromagnet coils in different combinations are used to generate uniform and non-uniform axial magnetic fields in the HeX. The copper pipes having inner diameter = 0.6 cm and outer diamerter = 0.8 cm are used to make these electromagnets coils. The forced water flow through the hollow copper pipes allows us to make the operation steady state. For all the magnets, a copper pipe is wrapped on to a PVC pipe of 30 cm inner diameter supported on both sides by rectangular hylem block of 60 × 60 cm of 1.6 cm thickness. Out of eight coils, the first seven coils (from the left in Fig. 3.1) have the same number of turns. In the first seven coils, there are six layers, each having six turns making a total of 36 turns. It makes the inner diameter, outer diameter, and width of coils ~ 31.5, ~43.5 cm and ~6 cm respectively. The last (the eight) magnet has a total of 30 turns in 5 layers. Layer to layer insulation is achieved by the self-adhesive cotton tape of 500 micron thickness, which provides insulation up to 1.5 kV. The electromagnets are placed on aluminum stand, which is shown in Fig. 3.2. The axis of all the electromagnets are collinear with axis of the vaccum chamber. These electromagnets are powered by a DC variable power supply (60 V, 250 A, Sorensen^{TM} make) to generate the variable magnetic field with maximum value of ~ 500 G.

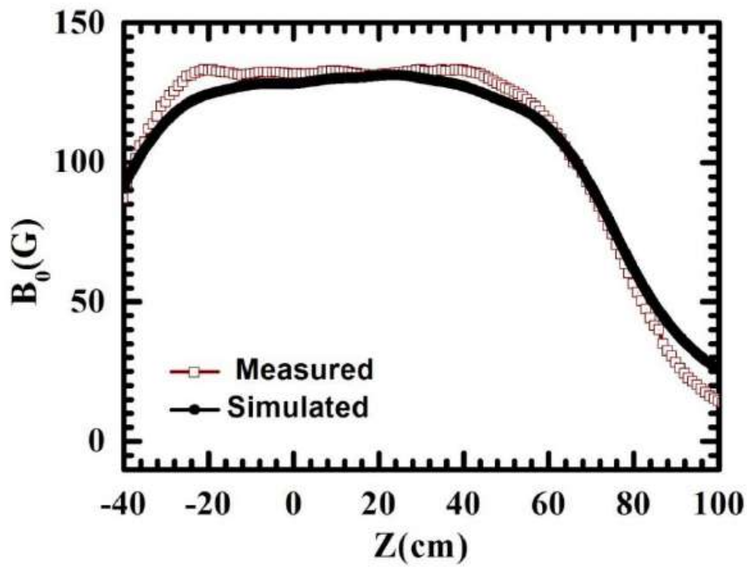

Fig. 3.5: Comparison of measured and simulated magnetic field at r = 0 cm when 52 A DC current is passed through all the electromagnet coils.

The different non-uniform magnetic field configurations over the different regions of source and expansion chambers can be produced by passing the direct current (DC) through a different set of electromagnets. Fig. 3.6(a) and 3.6(b) shows the axial variation of the simulated magnetic field when 1 A DC current is passed through different electromagnet combinations to produce different magnetic field configurations in the source and expansion chamber, respectively.

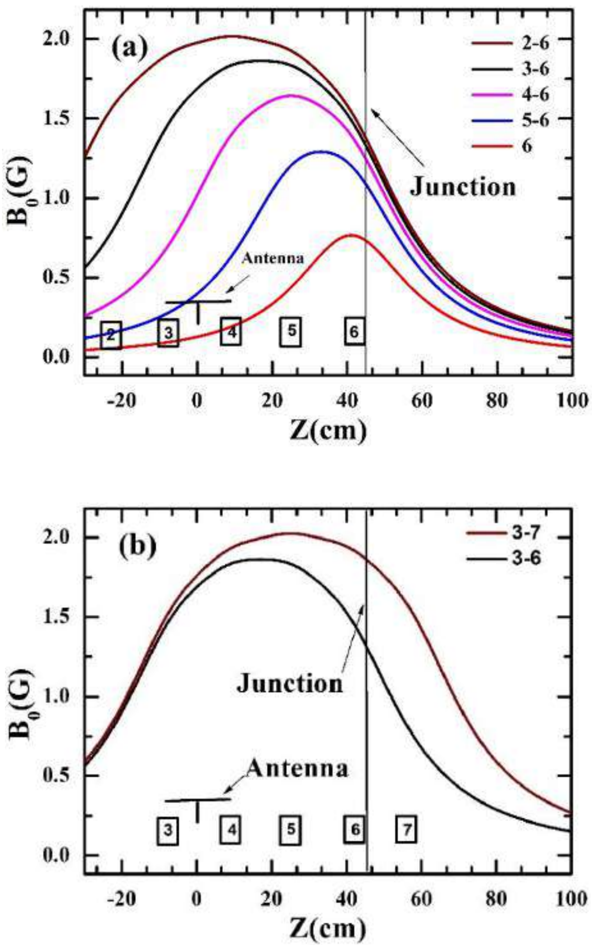

Fig. 3.6: Simulated axial non-uniform magnetic field profile in (a) source and (b) expansion chamber when 1 A DC current passed through different sets of magnets. The vertical straight line shows the location of source and expansion chamber junction.

3.3 Diagnostics

Various plasma diagnostics have been used in the HeX setup, namely single Langmuir probe, RF compensated Langmuir probe, emissive probe, high-frequency B-dot probe, and RF current probe. The details of each of these are described in the following subsections.

3.3.1 Single Langmuir probe

Single Langmuir probe [7–9] is the most basic and important plasma diagnostic used to measure the local plasma density, electron temperature, plasma potential, and electron energy probability function (EEPF). Langmuir probe is a biased electrode that is immersed in the plasma and draws a current when biased with respect to the reference electrode (vessel ground). The current drawn by the probe is measured as a function of biased voltages; this current versus voltage (I-V) characteristic contains the information of the plasma parameters. If the probe is biased at more negative voltage than the plasma potential the ion current starts to saturate, this region is called ion saturation region. The reverse is true for electron saturation when the probe is biased sufficiently positive than the plasma potential.

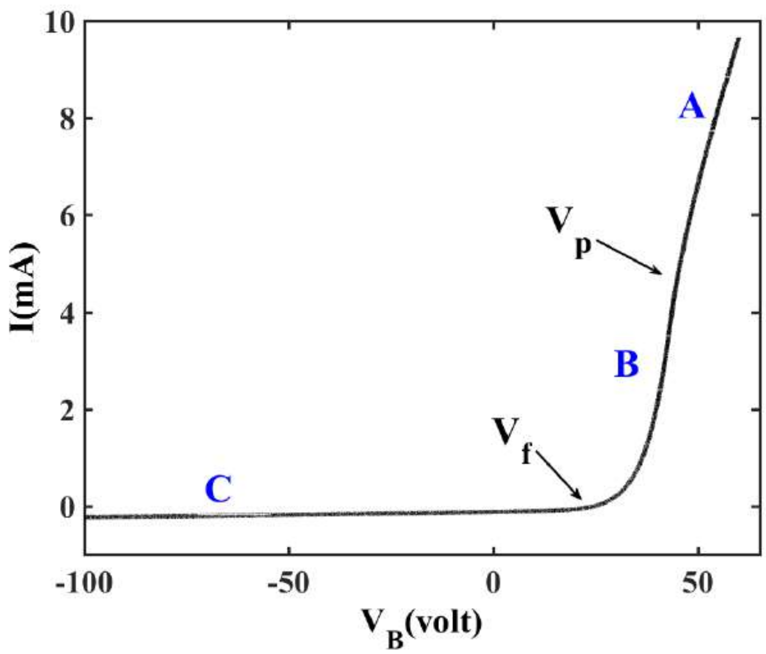

Fig. 3.7: Typical I-V characteristic obtains in HeX.

Fig. 3.7 shows a typical I-V characteristic obtain in HeX. The electron current collected by the probe is considered to be positive and the ion current negative. Vp is the potential of the plasma with respect to the probe reference, which in this case is the grounded vessel. When the probe is biased at plasma potential, there is no electric field between the probe and the plasma. Electrons and ions impinge on the probe surface with their thermal velocities. The electron flux to the probe is much higher than the ions owing to the lower mass of the electrons ($me \ll mi$) and higher electron temperature ($Te > Ti$). As a result, the current collected by the probe is predominantly electron current. If the probe voltage is increased above the plasma potential, a sheath is formed around the probe, and the sheath electric field attracts the plasma electrons entering the sheath to the probe. The probe current drastically increases on increasing the probe potential above the plasma potential as shown in the region A of Fig. 3.7. This is because of the sheath expansion around the probe resulting in an increase in the collecting area.

When $V_{\mathrm{B}} < Vp$, the probe becomes negatively biased with respect to the surrounding plasma and increasing fraction of the impinging electrons is reflected by the negative potential, this region is called electron retardation region, region B, in Fig. 3.7. The total probe current is zero when the electron current is equal to the ion current ($I_e = I_i$) at the floating potential V_f. Decreasing the potential further, entering the region C, eventually, all the electrons are repelled, and the probe collects only ion current. The ion current varies very slowly with the probe potential, and this region is termed as the ion saturation region.

The plasma density is estimated from the saturation parts of the probe current. In this thesis, the plasma density is estimated from the ion saturation current measured by a single RF compensated Langmuir probe (which is described in the next subsection). One can estimate the plasma density from the electron saturation also, but the current collected by the probe is so large that it drains the plasma and can the change the equilibrium properties (if one assumes the ideal Langmuir probe characteristic) [9]. However, the ideal situation is rarely found in practice, and sheath [10] formed around the probe tip expands on both the side with increasing bias voltage (very negative and positive than the plasma potential) as shown in Fig. 3.7. If sheath effect is not considered, the collecting area of the probe is underestimated, and plasma density is overestimated. Finding the actual collecting area in RF plasma and in the presence of magnetic field is not simple but can be estimated as [8,11],

$$\frac{x_s}{\lambda_D} = \frac{2}{3}\left[\frac{2}{\exp(-1)}\right]^{1/4}\left[\left(-\frac{eV_B}{T_e}\right)^{\frac{1}{2}} - \frac{1}{\sqrt{2}}\right]^{1/2}\left[\left(-\frac{eV_B}{T_e}\right)^{\frac{1}{2}} + \sqrt{2}\right] \tag{3.1}$$

Above equation can also be written as;

$$x_s = 1.02\,\lambda_D\left[\left(-\frac{eV_B}{T_e}\right)^{\frac{1}{2}} - 0.7\right].\left[\left(-\frac{eV_B}{T_e}\right)^{\frac{1}{2}} + 1.41\right] \tag{3.2}$$

For cylindrical probe, $A_S \approx A_P\,(1 + x_s/r_p)$, where r_p is the probe radius, x_s is the sheath thickness, A_s is the probe-sheath collection area and A_p is the probe area. This can be used in the following formula to give the ion saturation current:

$$I_{is} = 0.61en_i v_{Bohm} A_s = 0.61en_i\sqrt{\frac{KT_e}{m_{iAr}}}A_s \tag{3.3}$$

Where $I_{is}$the ion saturation current, v_{Bohm} is the Bohm velocity, e is electron charge, n_i is the ion density, and m_{iAr} is the mass of Argon ion.

For dense plasma (plasma density $> 10^{18} m^{-3}$) where thin sheath [12] approximation ($\lambda \gg r_p \gg \lambda_D$, where λ, r_P and λ_D are the electron-neutral mean free path, probe radius, and Debye length, respectively) is valid, ions enter the sheath with Bohm velocity and density can be easily determined using the Eq. 3.3 for given value of ion saturation current. However, in low density ($< 10^{16} m^{-3}$) plasmas, the sheath expansion effect is more prominent and thin sheath approximation fails, and density determination using the Eq. 3.3 gives an overestimate of the ion density, as shown in Fig. 3.8(a). Fig. 3.8(a) shows the comparison between the ion density calculated using Eq. 3.3 with and without sheath correction for increasing RF power. Fig. 3.8(a) clearly shows the overestimating of the ion density when the probe area is treated the same as the sheath area. Fig. 3.8(b) shows the calculated sheath thickness using Eq. 3.2, as density increases the sheath thickness reduces, and sheath thickness approaches towards the probe radius. Fig. 3.8(c) shows the percentage of overestimation if sheath correction is not taken care of. It is clear that the ion density is highly overestimated at low density compared to high density. As sheath thickness x_s is proportional to λ_D which depends on the $n_i^{-1/2}$, for higher density plasma, the sheath area approaches the probe area, $A_s \approx A_p$. Hence sheath correction is more important while working with low density.

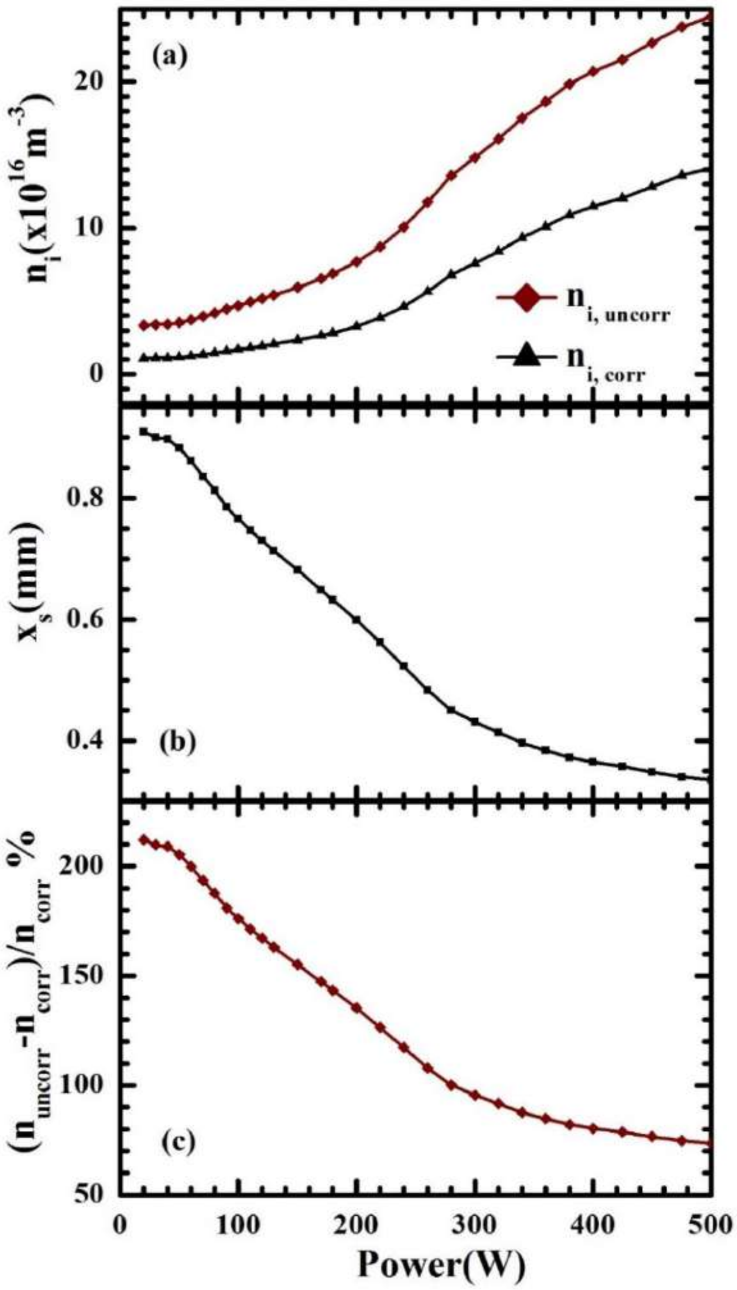

Fig. 3.8: (a) Comparison of variation of the ion plasma density calculated using the Eq. 3.3 with (solid triangle) and without (solid diamond) sheath correction for increasing RF powers. (b) Variation of sheath thickness for uncorrected ion density (c) variation of the difference in the ion density determined with and without sheath correction. Plasma at $2 \times 10^{-3} mbar$ fill in pressure, 220 G source magnetic field, Langmuir probe location $(r, z) = (0\ cm, 0\ cm)$.

The Biasing scheme of Langmuir probe for ion collection is shown in Fig. 3.9. The probe tip biased at some negative bias (using a number of batteries connected in series) with respect to vessel ground. In experiments to measure the probe current, a shunt resistance R_m is a current sensor, and the voltage drop across it is measured. This shunt resistance has to be chosen carefully as it becomes a part of the Langmuir probe circuit. In low-density plasmas, this resistance cannot be very small because in that case, the current signal will be comparable to the noise level of a practical Langmuir probe circuit. At the same time to quantify the response of plasma, all the probe bias voltage should drop in the sheath for which the sensing resistance should not be large enough that a significant portion of the bias voltage drops across R_m only.

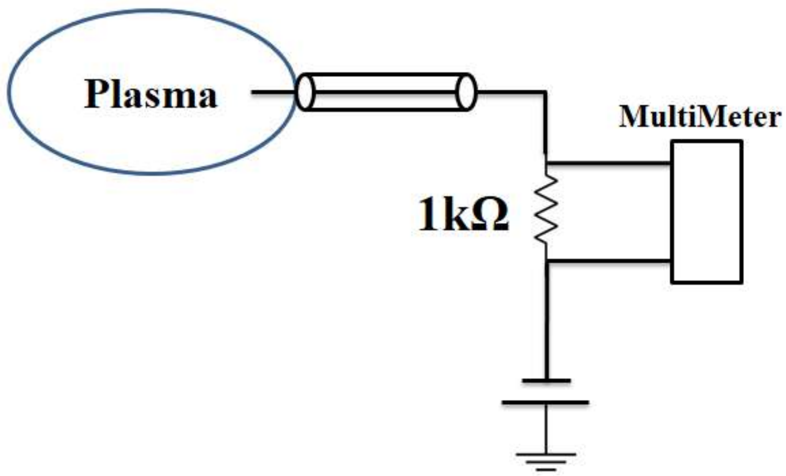

Fig. 3.9: Biased Langmuir probe in ion collection mode and the measured current is found from the voltage across the 1 kΩ sense resistance.

There are two different methods which we have adopted to determine the ion density from the ion saturation current. In one method, the probe is biased at fixed DC voltage in ion saturation regime (as discussed above) and current is measured through the sensing resistance as shown in Fig. 3.9. The plasma density is estimated using Eq.

3.3 by considering the sheath expansion effect (Eq. 3.2). Another method which we have used to determine the plasma density is Laframboise method. In this method, the RF compensated Langmuir probe is swept with bias voltage, and Langmuir probe characteristic is acquired using the data acquisition system.

3.3.2 RF compensated Langmuir probe

In plasmas produced by RF power coupling, RF interference significantly affects the Langmuir probe characteristics. In DC discharges the plasma potential is not varying with time, whereas the plasma potential in RF discharge fluctuates with time often with an amplitude as large as the electron temperature, T_e/e, (T_e is in eV) [13,14]. The Langmuir probe analysis requires that for each value of biased voltage, the collected probe current should be collected at a fixed difference of potential across the probe-plasma sheath. If the plasma potential fluctuates with time while the probe is at a constant voltage, the current measured is an average of the fluctuating probe-plasma sheath potential [10]. The I-V characteristics that are obtained in this situation are smeared out due to oscillations in plasma potential at operating source frequency. It has the effect of distorting the electron retardation region of Langmuir probe characteristic and shifting the floating potential towards more negative voltages which gives incorrect (overestimated) value of electron temperature and hence underestimation of the density. To have information of plasma parameters, the conventional Langmuir probe analysis of this distorted characteristics leads to erroneous results. The reason for this is illustrated in Fig. 3.10, which shows the instantaneous $I - V_B$ probe curves for various values of oscillating plasma potential $V_p(t)$.

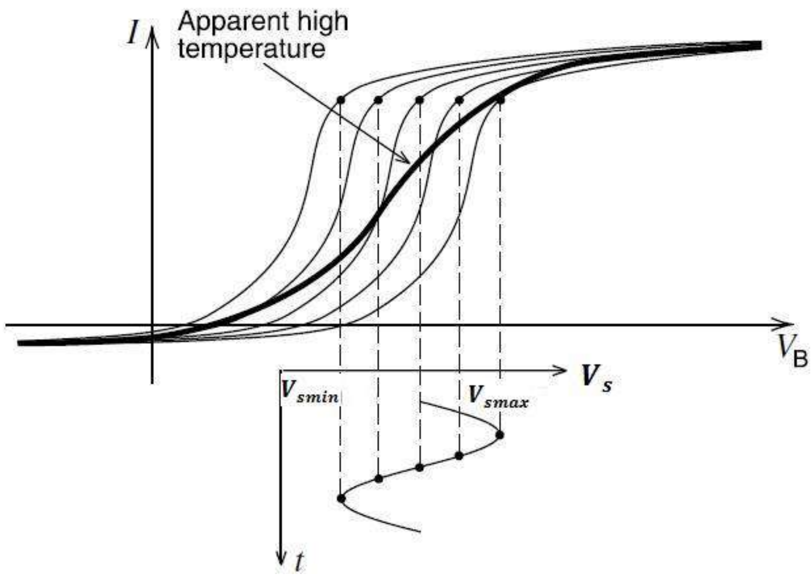

Fig. 3.10: Langmuir probe characteristics in a plasma with an oscillating plasma potential $V_p(t)$. Time-averaged probe characteristic (heavy solid line) shown the apparent electron temperature higher than the actual one. The figure is taken from reference no. 10 [10].

As plasma potential (the knee of probe curve marked with a vertical dashed line) oscillates in time as shown in Fig. 3.10, the probe curve oscillates horizontally back and forth. The time average of this motion, indicated as the heavy line gives the apparent "probe curve." It is clear from the figure that the electron temperature determined from this curve will be much higher than the actual T_e.

The rf compensation removes the RF distortion of the Langmuir probe characteristics; so that plasma parameters can be determined using the DC plasma theories. There are various techniques [14–19] adopted by the researchers to remove the RF effects from the probe characteristics so that DC Langmuir probe theory can be applied. There are mainly two ways to achieve RF compensation [16].

- **Active compensation**

Active compensation [18,19] method consists of biasing the probe tip with additional RF fluctuating voltage where the amplitude and phase of the RF bias are varied to optimize the probe I-V trace; usually by maximizing the floating potential. This way, the RF potential difference between the probe tip and plasma potential is again minimized. Since the sheath has a finite capacitance, higher harmonics of RF signal from the plasma can be generated, and the probe needs to be fed with harmonic frequencies and also the probe needs to be compensated for every change in the plasma conditions. Such techniques are the difficult and expensive method to implement.

- **Passive compensation**

Passive compensation consists of a tuned RF filter which is placed outside the probe [17], or set of self-resonating inductors built inside the probe support [14,20]. In either case, this setup creates a very high impedance of the probe tip for the RF frequency. This forces the probe tip to follow the RF oscillation in the plasma, and the probe current is equivalent to the current that would be measured in dc discharge. Often it is also required to capacitively couple to additional large area electrode to the probe tip to further reduce the probe sheath impedance. As the additional electrode is kept near to the probe, the compensation need not be changed every time.

3.3.2.1 RF compensated Langmuir probe for HeX:

As discussed above that the fluctuation of RF can distort the I-V characteristic, to overcome this problem, the passive compensation technique, as suggested by Sudit et al. [14] is adopted for our measurements. An RF compensated Langmuir probe consists of a measuring probe tip, reference floating electrode or compensated electrode and RF filters or self-resonating chokes, as shown in Fig. 3.11. The measuring probe tip is made up of a cylindrical tungsten wire of 1 mm diameter and 4 mm length, inserted into the 1 mm inner diameter and 2 mm outer diameter ceramic probe holder of 50 mm length. In the plasma, not only the choice of measuring probe tip is important, but insulated probe holder holding the probe tip is also crucial. Otherwise, the probe characteristic is distorted due to local plasma disturbance near the probe holder. In our case, the choice of ceramic probe holder also dictates the diameter of the floating reference electrode. For RF compensation, another floating reference or compensating electrode is placed near the probe tip to sample the same local plasma potential fluctuations as seen by measuring probe tip. The compensating electrode of 2.7 mm diameter and 20 mm length is made of several closed windings of 0.125 mm tungsten wire over the ceramic holder of the cylindrical probe tip. The compensating electrode dimension is a compromise between small plasma disturbance near the probe tip and large surface area for better fulfillment of compensation criteria, discussed below. The compensating electrode feeds the RF plasma fluctuations to the probe tip through a 10 nF capacitor. Two tiny self-resonating chokes (at the working frequency, f_1 = 13.56 MHz and it's second harmonic $2f_1$ = 27.12MHz) and the compensated electrode are placed as close as possible to the probe tip to minimize the stray capacitance at RF frequencies. These self-resonating chokes are used to block any RF current entering the probe current measurement circuit. The dimensions of the compensated electrode are chosen such that it produces minimum disturbance to the local plasma as well as works in a moderate plasma density of ~ 10^{16} m^{-3} in the limit of tiny self-resonating RF chokes. The physical pictures of RF compensation Langmuir probes are shown in Fig. 3.11. Fig 3.12 shows the measured impedance of self-resonating chokes connecting in series.

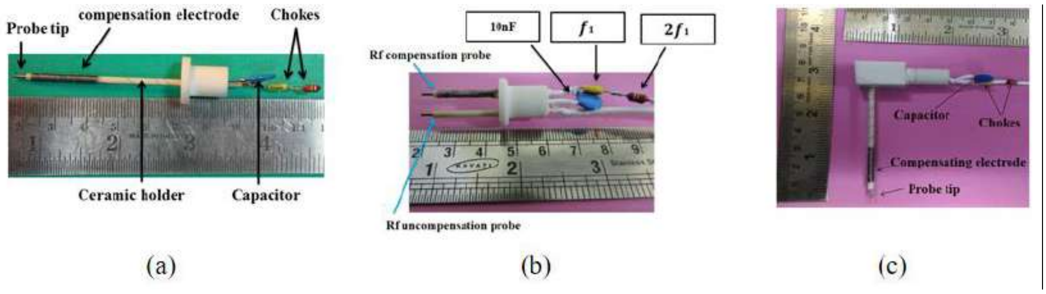

Fig. 3.11: Physical dimensions of the probe tip, the compensation electrode, and the self-resonating chokes.

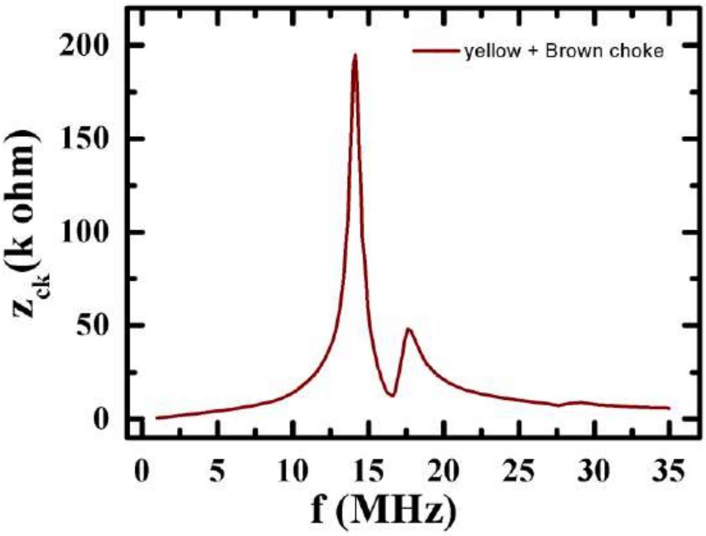

Fig. 3.12: Impedance curve for two self-resonating chockes connection in series.

3.3.2.2 Working principle

Langmuir probe measurement in RF environments is complicated due to the presence of the RF fluctuations in the probe sheath. The RF fluctuation must be eliminated to obtain reliable electron temperature measurements. The influence of RF potential fluctuation in the plasma can be compensated by special probe designs. The probe compensation technique suggested by Sudit et al. [14] is shown in Fig. 3.13. However, their technique employed for high-density plasma ($10^{19} m^{-3}$), but can be extended to moderate or low density ($\sim 10^{16} m^{-3}$) also. By suitable choice of the compensated electrode and tiny-self resonating chokes, one can achieve RF compensation for moderate density also. For the RF compensation the amplitude $V_P - V_{probe}$ of the RF voltage across the probe sheath must satisfy $\left(V_P - V_{probe}\right)/T_e \ll 1$ [10,14]. Where space or plasma potential is given by $V_P = V_{DC} + V_{rf}$ [9] and V_{probe} is the potential of the probe, V_B the probe bias voltage, V_{rf} is the rf oscillation of plasma potential about the mean value of V_{DC}. For compensation we require [14] $Z_{ck} \geq Z_{sh}$ $\left(\frac{eVrf}{KTe} - 1\right)$.

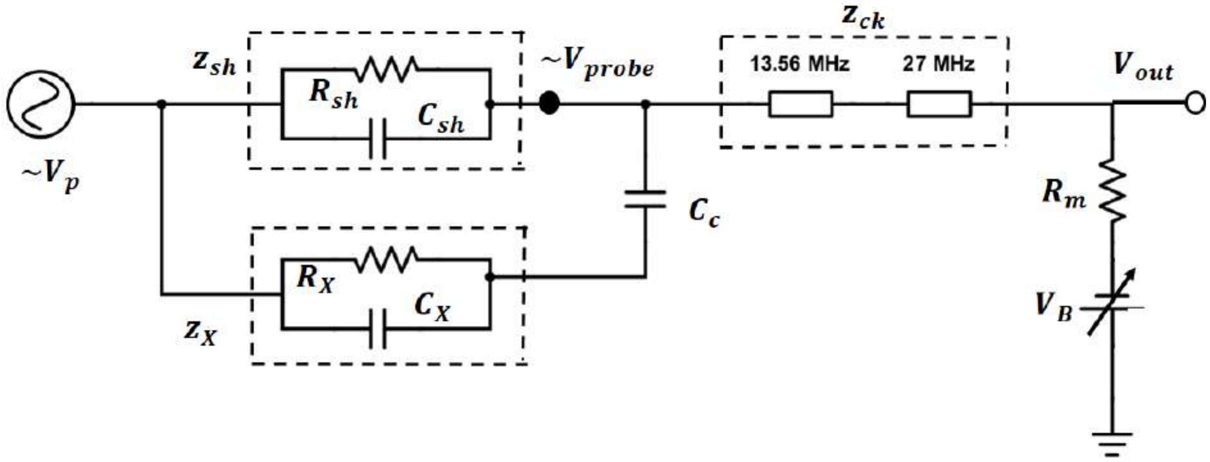

Fig. 3.13: Equivalent RF compensation circuit

Fig. 3.13 shows the equivalent circuit of Langmuir probe, sheath, and associated auxiliary electrode. The equivalent circuit is made to reject both 13.56 and 27.12 MHz oscillations. The sheath impedance consists of an equivalent resistance R_{sh} in parallel with an equivalent capacitance C_{sh}. The series of chokes is represented by impedance Z_{ck}. The auxiliary floating electrode has an impedance Z_X consisting of R_X in parallel with the capacitance C_X and is coupled to the probe tip by the coupling capacitor C_C. Choice of C_C is depending on the source frequency. This capacitor has values so large that it is a short circuit for RF signals but small enough that it does not pass low-frequency signals. V_{0ut} is the output voltage across the resistor R_m.

In our case the sheath resistance is $R_{sh} = \left(2\frac{\lambda_D^2}{\varepsilon_0 A_p v_b}\right) \approx 49\ k\Omega$, sheath capacitive reactance $X_{sh} = (1/\omega C_{sh}) = 123\ k\Omega$, where $C_{sh} = \frac{\varepsilon_0 A_p}{2^{\frac{7}{4}}\lambda_D}\left[\frac{e(V_{DC}-V_{probe})}{KT_e}\right]^{\frac{-3}{4}} = 0.095pF$ for $T_e = 6\ eV$ temperature and number density, $n_0 = 3\times10^{16}m^{-3}$. We get sheath impedance as

$$Z_{sh} = \frac{R_{sh}X_{sh}}{(R_{sh}^2 + X_{sh}^2)^{1/2}} = 45\ k\Omega.$$

In this situation, $Z_{sh}\left(\frac{eVrf}{KTe} - 1\right) = 332k\Omega$, without having a choke of impedance $Z_{ck} = 332\ k\Omega$, it is very difficult to block the RF modulation. But in our case, we have tiny chokes of few $k\Omega$. Since the choke must be placed in the probe shaft, it is critical to find chokes that are small enough to fit and have large impedance to the oscillating rf voltage.

So to satisfy the criterion, we either need to reduce Z_{sh} by placing an additional floating electrode in parallel with the probe or to obtain another tiny high impedance choke which is not readily available. Sheath resistance relation shows that the sheath resistance is inversely proportional to the density and the collection area. Therefore, at low densities R_{sh} increases and takes Z_{sh} away from fulfilling the RF compensation criterion. Placing an auxiliary electrode of diameter 2.7 mm and length 22 mm, close to the probe tip having a larger area than the probe area ($A_X \gg A_p$) reduces the effective sheath impedance. Placing this additional electrode near the probe tip also minimizes the stray capacitance between the probe wire and the grounded shaft. The careful selection of the additional electrode area is made such that it should work in the available present value of resonant choke and also be less disturbing to local plasma. Choice of a large area is limited by the disturbance of local plasma parameters. Since our measurements are perpendicular to the magnetic field, the length of the additional electrode (in our case 22mm) should not be larger than the ion larmor radius, to avoid the shorting of different regimes of the plasma column. Inserting the big electrode size much larger than the Debye length will also cause the local disturbance of plasma.

The chosen auxiliary electrode area $A_X = 1.92 \times 10^{-4} m^2$, is nearly 15 times larger than the area of Langmuir probe which is about $A_p = 1.33 \times 10^{-5}\ m^2$. With these parameters, the sheath impedance for the auxiliary electrode in the same plasma is calculated using R_X = 3.39× $10^3\ k\Omega$, $X_{cX}(1/\omega\ C_X) = 8.53\ k\Omega$, where $C_X = 1.37 \times 10^{-12} F$, giving $Z_X = 3.15\ k\Omega$ for V_{rf} = 50 *V*. Hence, effective parallel equivalent sheath impedance ($Z_{sh} \parallel Z_X$) is reduced to 3 $k\Omega$ which is much less than the impedance of the available self-resonating choke and satisfies the necessary RF compensation criteria. We have an impedance of choke around 150 $k\Omega$, as shown in Fig 3.12. The coupling capacitor has been chosen 10 *nf*, which allows the high-frequency 13.56MHz ($X_c = 1/\omega C_{cp} = 11.74\Omega$) to pass, but stops the low frequencies. This coupling capacitor plays an important role by stopping the low frequency or the dc current collected by the large auxiliary electrode. Otherwise, it will distort the entire single Langmuir probe characteristics.

3.3.3 Probe Circuit and Data Acquisitions:

The Langmuir probe is biased by triangular voltage waveform, which can be varied from -150 to +100 Volt. This voltage is generated by high voltage amplifier PA 85 with a function generator at its input. The probe current is measured by measuring the voltage drops across the resistance using an isolation amplifier. In our measurement, we have used a galvanic isolation amplifier (AD215) to acquire probe signal with respect to the grounded data acquisition system. The current measuring resistance can be varied from 100 ohms to 500 ohms depending on the plasma operating conditions. The coaxial cables are used to carry the signal with a grounded outer shield to reduce the noise pickup. The Langmuir probe bias voltage is swept at a low frequency of 2.2 Hz. This is done to ensure that the displacement current between the center conductor and outer shield of coaxial cable much less than the ion saturation current. To obtain the electron energy distribution function (EEDF), the output of the isolation amplifier is fed to two-stage analog differentiator circuit. The details of the EEPF using double derivative analog circuit is discussed below. The schematic of the probe biasing scheme is shown in Fig. 3.18.

Fig. 3.11 shows that the physical picture of three different (but same collection area) RF compensated Langmuir probes. Fig. 3.11(b) shows the picture of compensated and uncompensated Langmuir probes. The uncompensated Langmuir probe is kept only for comparison purpose. After installation of the compensated and uncompensated probe assembly inside the expansion chamber, probe characteristics have been obtained. Current-voltage (I-V) characteristics of the Langmuir probe is obtained by sweeping the probe bias voltage from -90V to +90V at a frequency of 2.2Hz. The data is acquired using a 14-bit data acquisition system (NI 6133) with the sampling rate of 100 kHz with a record length of 50k samples using current measuring resistance of 200 ohms. Fig. 3.14(a) and Fig. 3.14(b) shows a typical I-V trace and semi-logarithmic plots of the RF compensation and uncompensated Langmuir probes taken in the expansion chamber at Argon fill pressure of 1×10^{-3} mbar, RF power of 200 W, and source magnetic field value 50 G. The measurements are performed at the location of (r, z) = (0, 50) cm in the expansion chamber. It is seen from Fig. 3.14 that the compensated Langmuir probe shows the more positive floating potential and less electron temperature compared to uncompensated probe.

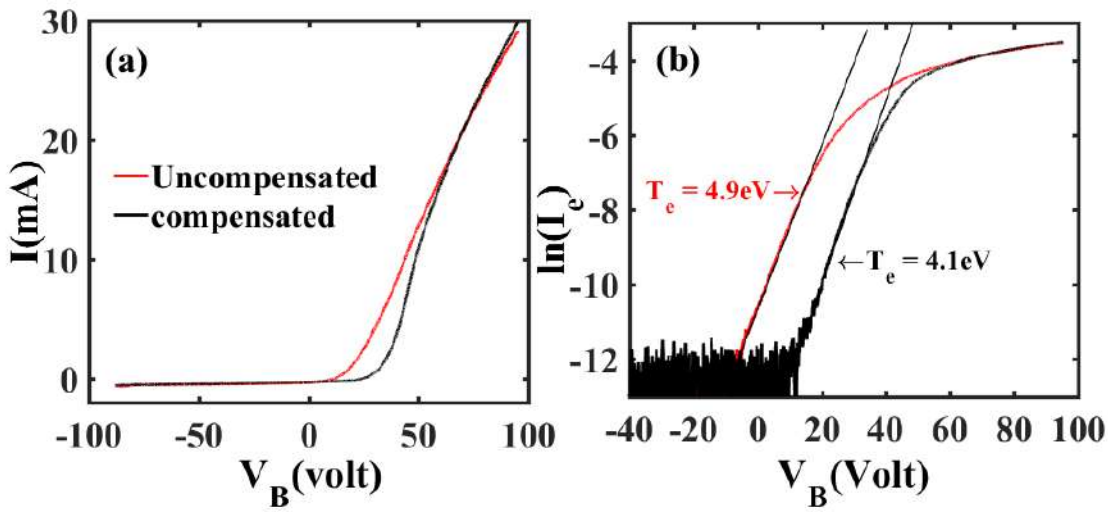

Fig. 3.14: (a) Langmuir probe I-V trace and (b) Semi-logarithm of I-V trace in the expansion chamber at (r, z) = (0,50) cm with 200 W RF power, I(3-6) = 30A (50 G) coil current, and Argon fill pressure of $1\text{x}10^{-3}$ mbar. The compensated (black curve) and uncompensated (red curve).

After the comparison, the uncompensated Langmuir probe was removed and only compensated probe was kept to avoid unnecessary disturbance to the plasma. Fig. 3.11(a) and Fig. 3.11(c) show the physical picture of only RF compensated Langmuir probe one straight and other L shaped. An L-shaped RF compensation Langmuir probe is used in the expansion chamber; by rotation and translation of the probe, it has been possible to position it at various radial and axial locations, respectively.

3.3.4 Langmuir probe data analysis

Plasma is produced by powering the helical antenna at 13.56 MHz frequency and only compensated Langmuir probe is inserted from the source or expansion chamber diagnostic ports in order to measure the plasma parameters. Data analysis of raw (I -V) trace determines the floating potential, plasma potential, electron temperature (T_e) and ion density. A MATLAB code has been written to analyze the Langmuir probe data. The code is capable of providing all the above information from the raw I-V data. The code has been written emphasizing the moderated plasma density ($10^{16} m^{-3}$).

The Langmuir probe data is loaded, and appropriate smoothing is done by moving smoothing method, this removes the electronic and digital noise. The first numerical value obtained from the probe characteristic is the floating potential $V_f = V_B(I_p = 0)$.

The space potential or the plasma potential may be easily determined from the I–V characteristics using the tangent or the derivative method. In the tangent method, the space potential is estimated from the point of intersection of tangents drawn in the electron retarding and electron saturation region in the semi-logarithmic curve of probe current versus probe potential. Here the plasma potential is determined from the derivative methods as it is more sensitive to changes in the probe current. The plasma potential determined from the maximum of the first derivative and zero-crossing point of the second derivative of the probe current is shown in Fig. 15(b) and Fig. 15(c), respectively. The first and second derivatives are acquired using the analog differentiator circuit, which will be discussed in the next subsection. Typical I-V characteristic is shown in Fig. 15(a).

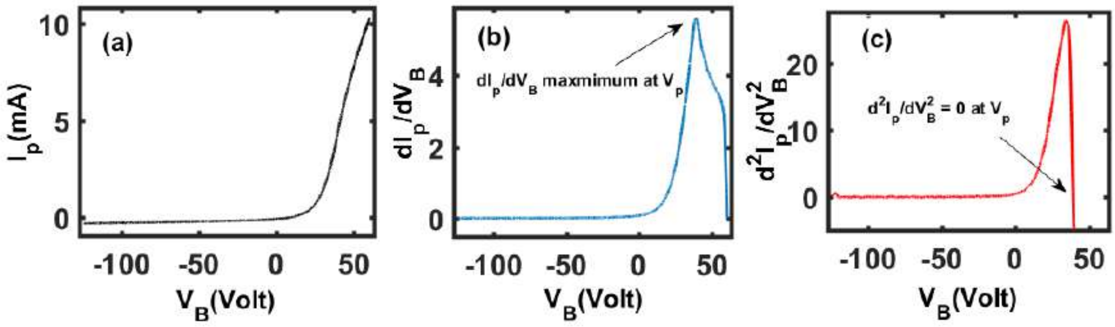

Fig. 3.15: (a) The I-V characteristic acquired using the Langmuir probe (b) First derivative using the analog differentiator (c) Second derivative using analog differentiator. Plasma at 200 W, 220 G source magnetic field and pressure 1×10^{-3} mbar at $(\mathrm{r, z}) = (5\ \mathrm{cm}, 50\ \mathrm{cm})$.

Next step is the determination of electron temperature; for this ion current has to be removed from the total probe current. For that, the ion current which varies weakly with the probe potential is subtracted from the probe current. This is done by making use of linear dependence of the square of the probe current on the probe potential. The reason that we have a plot $I_i^2 - V_B$ rather than $I_i - V_B$ is that measured $I_i^2 - V_B$ tend to be linear over a large range of density [9,21,22]. The ion saturation part of the I-V characteristic at sufficiently negative probe potential is fitted with the equation $I_i = \{A(V_B - V_P) + B\}^{\frac{1}{2}}$ and extrapolated to V_P where V_P is plasma potential and A and B is the slope and initial value for line fit. This is shown in Fig. 3.16. The fitted curve then subtracted from the total probe current this shown in Fig. 3.16.

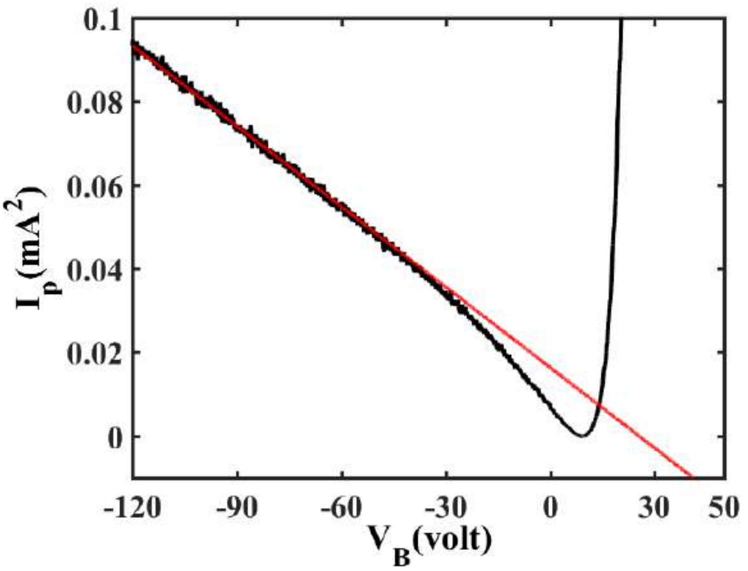

Fig. 3.16: Squared current as a function of probe voltage. Red line shows the I_i^2 fitting.

After subtraction of square fitted ion current from the total probe current as shown in Fig. 3.17(a) the electron temperature is determined from the semi-logarithmic plot of the electron current (I_e) Fig. 3.17(b). The $\ln I_e$ Vs V_B plot has two distinct linear regions. Each linear region of $\ln I_e$ Vs V_B plot contains the information of a separate group of the electron temperature. The temperature of the high energy tail electrons (T_h) is determined by fitting a straight line in the linear region of the semi-logarithmic plot for probe biases much more negative than the plasma potential. This fitted line is extrapolated to plasma potential (red dash line in Fig. 3.17(b)) and subtracted from the total electron current to obtain the bulk electron current. Fitting the remaining trace to another straight line yields the bulk electron temperature (T_c) as shown by a blue dotted line in Fig. 3.17(b). The bulk and high energy tail electron densities are found by the respective electron currents at the plasma potential. The fraction (α) of electrons in the high energy tail is calculated from the current at the plasma potential due to the tail electrons divided by the electron saturation current [23,24] taking into account of their temperature ratio. Based on the kinetic definition of electron temperature,

$$T_e = \frac{1}{3}\, m_e \int_{-\infty}^{\infty} v^2 f(v) dv \tag{3.4}$$

an effective electron temperature ($T_{e,eff}$) can be derived, shown in Eq. 5, by assuming the electron energy distribution to be a bi-Maxwellian {22} $f(v) = (1-\alpha) f_c(v) + \alpha\, f_h(v)$, where, v is the electron velocity, $f_c(v)$ is the bulk electron Maxwellian distribution and $f_h(v)$ is another Maxwellian distribution function due to the enhanced tail of the electron distribution.

$$T_{e,eff} = (1-\alpha) T_c + \alpha T_h \tag{3.5}$$

From Fig. 16(b), we get T_c = 5.2 eV, T_h = 12.7 eV and α = 0.21, the resulting effective electron temperature is then $T_{e,eff}$ ~ 7 eV.

The next step is to determine the ion density. The numerical results of Laframboise theory were used to estimate the plasma (ion) density from the collected ion saturation current of I-V characteristic, assuming the ion temperature(T_i) is less than the electron temperature (T_e). For the ion density of the order of $\sim 10^{16} m^{-3}$, the Debye number ($D_\lambda = \frac{r_p}{\lambda_D}$) is varied from the $3 < D_\lambda < 10$, where r_p and λ_D probe radius and debye length. Eq. 3.3, $I_{is} = 0.61 e n_i \sqrt{\frac{KT_e}{m_{iAr}}} A_p$ cannot be applied easily to calculate the ion density, since it applicable for thin sheath or high-density plasma ($D_\lambda \gg 1,$). The constants have their usual meaning. For the low ion density case, the ion density is evaluated from the Lamframboise method, which is applicable for a wide range of Debye number. The detail of ion density estimation from the probe data using Lamframboise method is given in reference [12].

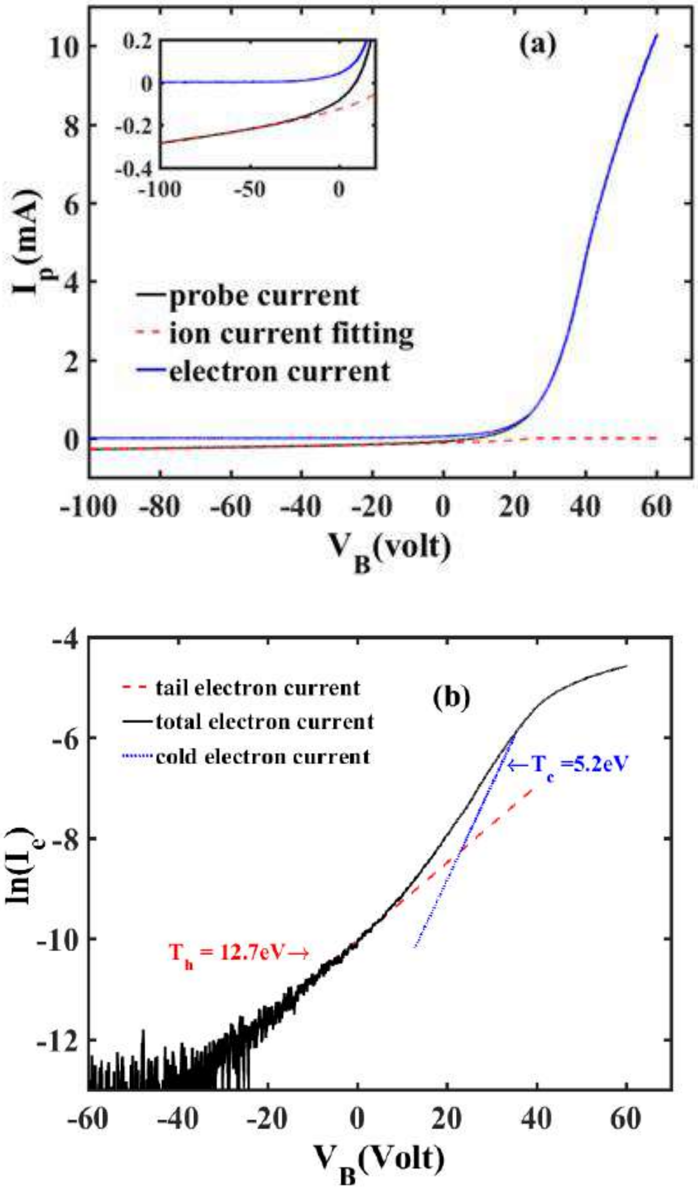

Fig. 3.17: (a) Typical Langmuir probe I-V trace using RF compensated probe. The contributions of ion (red dashed line) and electron (blue solid line) currents to the probe current for a probe bias in the range of −100 V to +20 V are shown in the inset. (b) Semi-logarithm of the I-V trace and the linear fit of hot (red dashed line) and cold (blue dotted line) electron populations.

3.3.5 Langmuir probe in magnetized plasma

In the plasma, the magnetic field often introduced mainly for two reasons, enhancement of plasma (such as in electron cyclotron resonance (ECR) or helicon plasma source) and plasma confinement. The presence of a magnetic field affects the motion of charged particles in a perpendicular direction. In the presence of the magnetic field, the electrons and ions gyrate around the magnetic field line with gyration radius of $r_L = \frac{mv_\perp}{qB_0}$, where m and q is mass and charge of the electron or ion, $v_\perp$ is the thermal velocity of the particle and B_0 is the ambient magnetic field. The motion of charged particle across the field is greatly restricted; however motion along the field lines is similar to the magnetic field-free case. The presence of the magnetic field affects the motion of electrons more than the ions because the Larmor radius of the electron is lower than that of ion since the electron has a lower mass than the ions. The influence of the magnetic field to the probe measurement can be divided into three categories (i) $r_P \gg r_{L\,i,e}$ weak magnetic field case, i.e., the probe radius is larger than both electron and ion gyroradius. For weak magnetic fields, no significant effect on probe characteristic has to be expected in comparison to zero magnetic fields. (ii) $r_{Li} > r_P > r_{Le}$ moderate magnetic field case. In a moderate magnetic field, case anisotropy can appear, in particular in the electron component of probe characteristic. The mobility of the electrons perpendicular to magnetic field lines significantly reduces and so the orientation of the probe tip with respect to field lines changes the probe characteristic. In moderate magnetic field case, experimentally it has been found that the estimated electron temperature from slope of electron retardation region in I-V is agreed with temperature measured using three gridded energy analyzer [25] and velocity measurement of an ion-acoustic wave propagating along the magnetized plasma column. In a moderate magnetic field, the electron saturation current may be affected, whereas the ion saturation current is basically not influenced by the magnetic field. The ratio of electron to ion saturation for planar probe in Argon plasma is around 180, and it decreases between 15 to 30 depending on magnetic field strength. (iii) $r_P > r_{Li} >> r_{Le}$ very strong magnetic field case i.e., electron and ion have Larmor radius smaller than the probe dimension. In this case, ion saturation current also affected by the magnetic field, and tedious interpretation is required to determine ion density.

Our experiments are confined to moderate magnetic field case where the ion density can be determined using unmagnetized collisionless plasma theory. The Langmuir probe is always perpendicular to the magnetic field until otherwise noted. The temperature measured from the linear region of the ln I_e vs V_B curve and density is obtained from the ion saturation current.

3.3.6 Electron Energy Probability Function (EEPF):

The RF plasmas are widely used in the semiconductor industry and material processing applications. The study of electron energy probability function (EEPF) in such plasma is extremely important for understanding physical processes and calculating reaction rates [10,26]. Langmuir probe diagnostic methods are suitable for measuring plasma parameters, including the EEPF in low-pressure gas discharges. The EEPF is inferred from the second derivative of the probe current-voltage characteristic, has been used for the last several years to measure EEPFs in many different kinds of gas discharge plasma [20,27]. In this thesis, the RF compensated Langmuir probe are used to find the EEPFs and subsequently to study the electron dynamics with regards to double layer physics. Following approach in ref [10] are used to show the dependency of EEPF on the double derivative. The electron current I_e collected by the planar probe in retarding potential region $V_p - V_B > 0$ can be written as

$$I_e = eA\int_{-\infty}^{\infty} dv_x \int_{-\infty}^{\infty} dv_y \int_{v_{min}}^{\infty} v_z f_e(\boldsymbol{v}) dv_z \tag{3.6}$$

Where $f(v)$ is the electron velocity distribution function, v is the electron velocity with component v_X, v_y and v_z and $v_{min} = \left[\frac{2e(V_p - V_B)}{m}\right]^{1/2}$, V_p the plasma potential, V_B probe bias voltage, A probe collection area, e electron charge, and m is the electron mass. For isotropic distribution, introducing spherical coordinates (in velocity space) letting $V = V_p - V_B$ and performing a change of variables using $\varepsilon e = \frac{1}{2}mv^2$, eq. (6) becomes,

$$I_e = \frac{2\pi e^3 A}{m^2}\int_V^{\infty} \varepsilon\left(1 - \frac{V}{\varepsilon}\right) f[v(\varepsilon)] d\varepsilon \tag{3.7}$$

Where $v(\varepsilon) = \sqrt{\frac{2e\varepsilon}{m}}$. By then, differentiating Eq. 3.7 twice with respect to V

$$\frac{d^2 I_e}{dV^2} = \frac{2\pi e^3 A}{m^2} f[v(V)] \tag{3.8}$$

Defining the electron energy distribution function (EEDF), $g_e(\varepsilon)$, as

$$g(\varepsilon)d\varepsilon = 4\pi v^2 f(v) dv \tag{3.9}$$

and using the relation between v and ε in Eq. 3.9 we find ;

$$g(\varepsilon) = 2\pi\left(\frac{2e}{m}\right)^{3/2} \varepsilon^{\frac{1}{2}} f[v(\varepsilon)] \tag{3.10}$$

By then multiplying both side by $\varepsilon^{-1/2}$, the electron energy probability function (EEPF) is defined as $g_p(\varepsilon) = \varepsilon^{-1/2} g(\varepsilon)$. Then using Eq. 3.10 to eliminate f from Eq. 3.8, we get

$$g_p(\varepsilon) = \frac{\sqrt{8}m_e}{e^{3/2}A_P}\ \frac{d^2I_e}{dV^2} \tag{3.11}$$

Which gives EEPF $g_p(V)$ directly in terms of the measured value of $\frac{d^2I_e}{dV^2}$. Where $\varepsilon = e(V_p - V_B) = eV$ is the electron energy in equivalent voltage units. If the distribution function is Maxwellian, then Eq. 3.11 becomes

$$g_p(\varepsilon) = \frac{2}{\sqrt{\pi}} n_e kT_e^{-\frac{3}{2}} e^{-\varepsilon/kT_e} \tag{3.12}$$

Where T_e is the electron temperature. If the natural logarithm of Eq. 3.11 and Eq. 3.12 are taken then natural logarithm of EEPF is directly proportional to the inverse of the temperature as shown in Eq. 3.13;

$$\ln g_p(\varepsilon) = \ln\left(\frac{d^2I_P}{dV_B^2}\right) + constant = \ -\left(\frac{\varepsilon}{KT_e}\right) + constant \tag{3.13}$$

Where the inverse slope in the semi-logarithmic plot double differentiation with electron energy gives the electron temperature.

The knowledge of electron energy distribution has great importance in understanding the nature of current free double layer (CFDL) [28,29]. The double derivative of a single Langmuir probe current is proportional to the EEPF. To measure the EEPF the double derivative circuit is developed. The circuit design is the compromise between the better energy resolutions to low energy electrons and high signal to noise ratio to high energy electrons. The EEPF is directly measured by differentiating twice the collected probe current using a series of two-stage analog double differentiator circuit. There is another way to do the differentiation that is numerical differentiation, but sometimes it is less effective, especially in RF plasma where different frequency's noise is already present.

Numerical differential enhances the noise which is already present in the raw Langmuir probe characteristic, which is ignorable in many cases. To avoid a large amount of data smoothing and filtering, which often introduces error, an analog differential approach is adopted here.

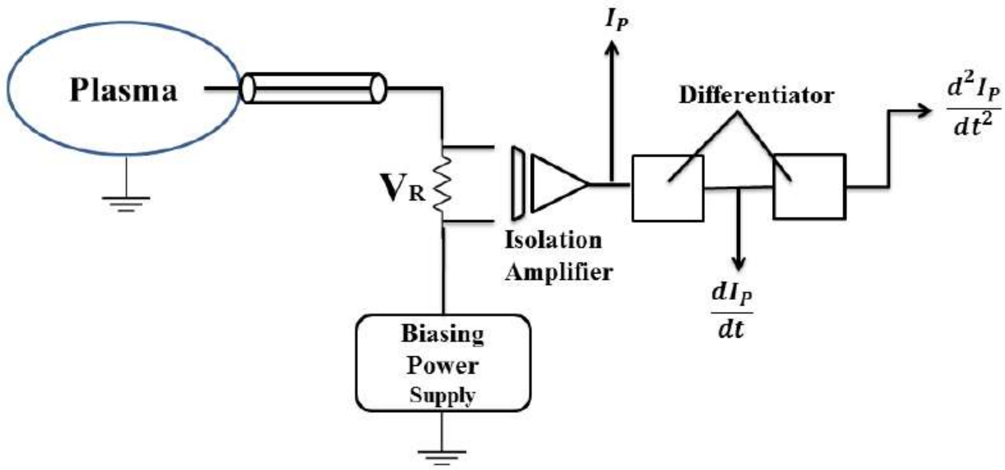

Fig. 3.18: The scheme for the measurement of the double derivative using analog differentiator.

To measure the EEPF, the L-shaped RF compensated Langmuir probe inserted in the expansion chamber at (r,z) = (5 cm, 50 cm). Plasma is produced at 200 W, 1×10^{-3} mbar pressure and source magnetic field of 220 G. The scheme used to measure the EEPF is shown in Fig. 3.18. A triangular waveform (ramp bias voltage) shown in Fig. 3.19(a) is generated using the Agilent 33220A function generator at a frequency of 2.2 Hz and amplified using the power amplifier PA 85. The signal from the RF compensated Langmuir probe is fed to the two-stage differentiator through the isolation amplifier with unity gain. Output signal of the probe and differentiator are acquired using the NI 6133 data acquisition system with a sampling rate of 100 kS/s and 50 k samples. Fig. 3.19(b) shows the RF compensated Langmuir probe characteristic.

Corresponding to bias voltage, the 1st and 2nd derivative signals are also simultaneously acquired and shown in Fig. 3.19(c) and Fig. 3.19(d).

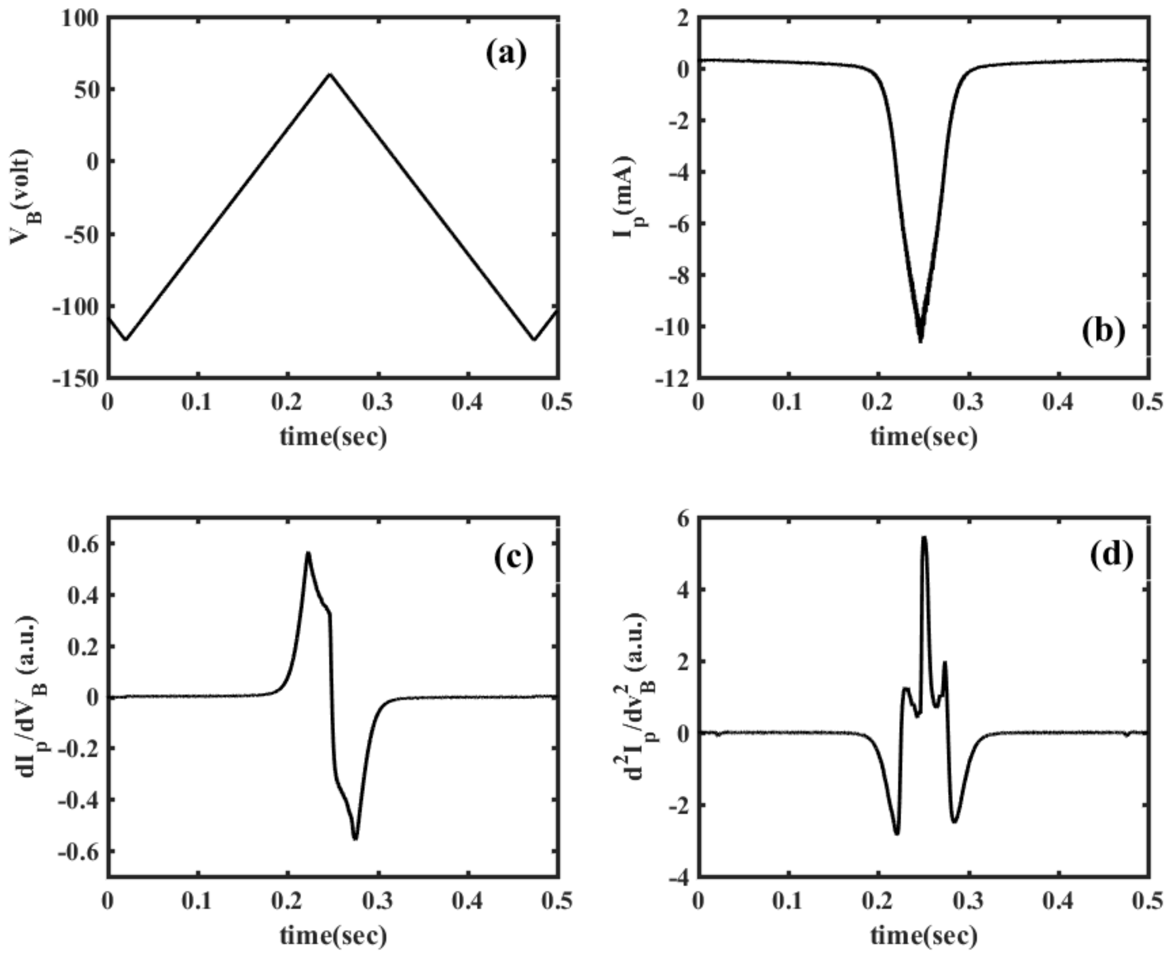

Fig. 3.19: Raw data for simultaneously measured (a) triangular bias voltage (b) RF compensated probe signal (c) first derivative (d) second derivative for plasma at 200W, 1×10^{-3}mbar pressure, source magnetic field 220 G and $(r, z) = (5\ cm, 50\ cm)$.

The second derivative of the current-voltage trace contains the EEDF and the local V_P, the latter being taken as the zero crossing of the curve and the EEDF being the section of the curve to the left of V_P . This is because the electrons in the plasma see the local plasma potential as a zero reference for the EEDF and the sweeping voltage of the probe uncovers more and more of the EEDF as it approaches V_P from below. Hence, the zero reference of the local EEDF actually represents the local V_P.

The presence of tail Maxwellian electrons is further verified by analyzing the double differentiated signals. The electron temperature is obtained from the semi-logarithmic plots of EEPF with the electron energy, as shown in Fig. 3.20. As Fig 3.17 (b), Fig. 3.20 also shows two distinct linear regions which correspond to the two-electron population with different temperatures. The slope near the low energy electrons represents cold or bulk Maxwellian electrons, and slope in another linear region represents the high energy tail electron temperature.

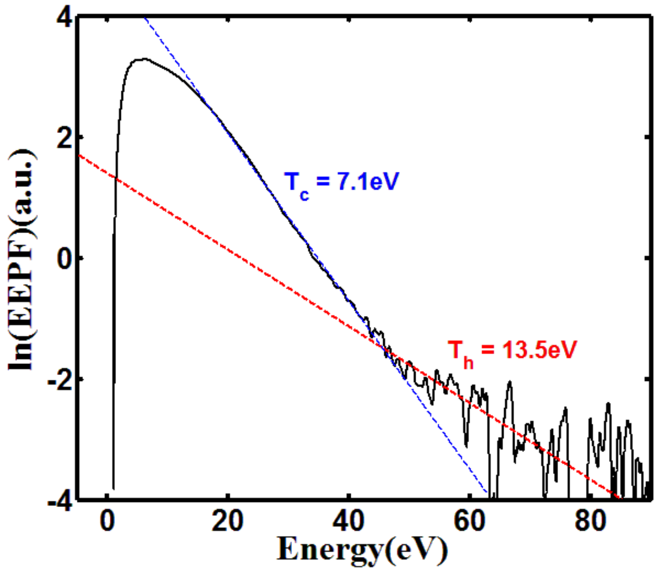

Fig. 3.20: EEPF deduced using an active analog differentiator in the expansion chamber at (r, z) = (5,50) cm with 200 W RF power, 220 G source magnetic field and argon fill pressure of 1×10^{-3} mbar. The blue and red line represent the bulk and tail electron contributions.

3.3.7 Emissive Probe

Along with plasma density and electron temperature, plasma potential is one of the most important parameters of plasma. Direct measurement of plasma potential can be obtained by using an emissive probe [30]. Electron emission from the probe provides an opportunity for direct measurement of the plasma potential. Although several techniques [30] have been developed for interpreting emissive probe characteristics, they all are based on one principle. When the probe is biased more positive than the local potential, electrons emitted from the probe are reflected back to the probe. When the probe is biased negative with respect to the local plasma potential, electrons can escape to the plasma and appear as an effective ion current. This process is not sensitive to plasma flow because it depends directly on plasma potential rather than electron kinetic energy, and it is less sensitive to probe surface contamination when heated surface provide electron emission [31]. Unlike collecting probes, emissive probes do not give useful data on plasma density or electron temperature. Initially, without heating current, the emissive probe is similar to a normal Langmuir probe, and sits at the floating potential. As the current increases, more electrons are emitted from the filament, and the potential difference between the probe and plasma decreases. As the current is further increased, the potential begins to saturate to a roughly constant value. Since the floating potential cannot rise to potentials larger than plasma (unless space charge effects are present), this provides a simple means to finding the plasma potential. This method of measuring plasma potential is known as floating potential method with large emission current. An example of this is shown in Fig. 3.21 where the potential reached to the saturation at $\sim 2.8\ A$ filament current and the plasma potential is 55 V.

There are other methods such as inflection point method [32] and separation technique [33]. In inflection point method filament is heated below its maximum emission current and take the current-voltage characteristic like single Langmuir probe and its first differentiation shows a peak near the knee of the electron saturation is called the plasma potential. This method is useful to reduce the space charge effects associated with the maximum emission floating potential method. Taking the similar I-V characteristic with the various moderate heating current in inflection point of the emitting probe and extrapolate a straight line fit to the zero-emission gives a more accurate measurement of plasma potential. However, it is difficult to identify inflection points when noise or RF oscillations re present. The inflection point method cannot measure temporal variations easily and is difficult to use in high energy density plasmas. Moreover, this method is very time consuming to measure plasma potential at one location, compared to the floating potential method.

Typical separation point method is based on the fact that the I-V characteristics of an emitting (hot) probe and collecting (cold) probe tend to separate from each other near the plasma potential. The bias voltage corresponding to the separation can be taken as the plasma potential. Plasma potential measured using this method is focused to be higher compared to the other two methods. The floating point method can measure the potential in a sheath and in the presence of beam and double layer plasma. In this method, the floating potential is measured across a high ($\sim M\Omega$) resistance connected between the emissive probe and ground. This measurement is accurate as the probe floats at the floating potential and no current is drawing to the ground because of this high resistance in the path.

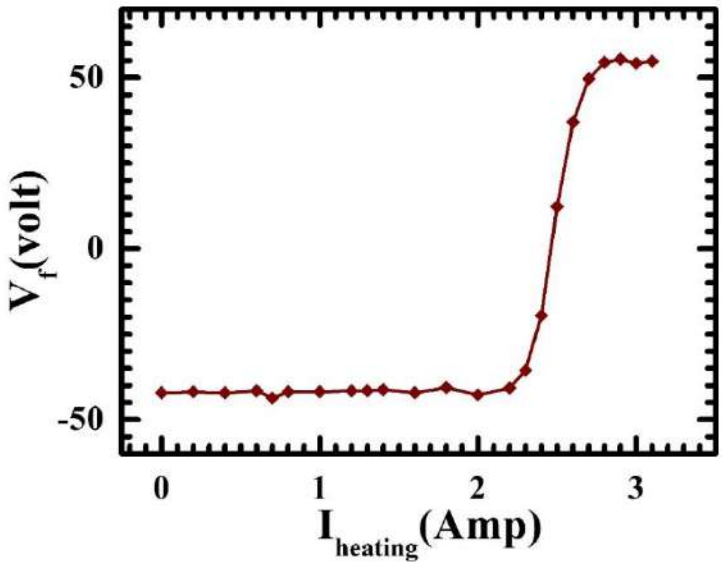

Fig. 3.21: Floating potential variation of an emissive probe versus filament heating current measured at z = 32 cm for 400 G source magnetic field, 200 W RF power and 2×10^{-4} mbar pressure.

3.3.7.1 Construction and operation of emissive probe

A tungsten wire of diameter 0.125 mm with a loop of less than 5 mm is used to make the emissive probe. The wire was bent in the form a hairpin and inserted in a miniature double bore ceramic. The tungsten filament is push-fit into two copper (Cu) tube via two tiny ceramic beads. The opposite end of this Cu tube is pressed against to two current-carrying wire inside the double bore ceramic, as shown in Fig. 3.22(a) and (b) to fit tightly in bores of ceramic tube, to make good electric contact. This Cu push-fit armament provides the flexibility on ease of replacement of tungsten filament after it burns during the plasma operation. The ceramic beads between the tungsten filament and Cu tube prevent the direct coating of Cu over the tungsten, making its life longer. The bad electric contact (whole electric connection resistance > 0.5 ohm) makes the emissive probe lifetime poor. In our case, the contact resistance is always less than 0.5

ohm. Plasma potential has been measured using the floating potential method as it is not affected by the magnetic field, and a large number of measurements can be carried out using this method very quickly. The potential difference between the floating hot emissive probe and the grounded vessel is measured using two resistance of value of 10 $M\Omega$ and 100 kΩ in the potential divider method. The emissive probe circuit is shown in Fig. 3.22 (c).

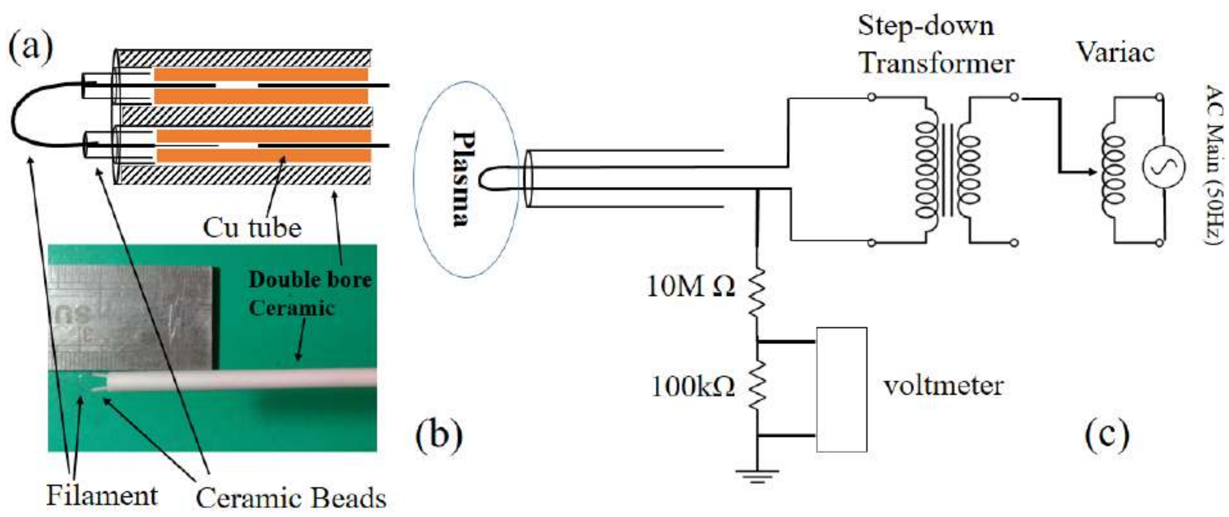

Fig. 3.22: (a) Emissive probe construction, (b) Physical picture of an emissive probe (c) emissive probe measurement circuit.

3.3.8 B-dot Probe

Magnetic fluctuation probes (B-dot probes) have been widely used to measure the oscillating magnetic field in the plasma [34–36]. B-dot probes consist of a pickup coil of n windings of a wire enclosing an area A. The time varying magnetic fluxes through an area A induce a voltage;

$$V_{ind} = -n\,A\frac{\partial B}{\partial t} \tag{3.14}$$

For a sinusoidal fluctuation, $B(t) = B_0 sin\omega t,$ the induced voltage is;

$$V_{ind} = -n\,A\,B_0\omega\cos\omega t \tag{3.15}$$

The fundamental problem of B-dot probe is their AC (alternating current) coupling to electrostatic potential fluctuations, so-called capacitive or electrostatic pickup. In RF generated plasma, large fluctuating potential difference occur between the plasma and the magnetic probe. This partially coupled capacitively into the leads of the B-dot probe giving undesired non-inductive signal component. This pickup signal depends on the potential amplitude, the capacitance between the probe and plasma, and the terminating resistance. Often a 50 Ohm terminating resistance is used to reduce the electrostatic pickup. But sometimes this is not enough at least when the wave field amplitudes are small. In such a case, precaution should be taken to reduce the capacitive pickup in comparison to the actual magnetic fluctuation signal. To get rid of this capacitive pickup some techniques like hybrid combiners or baluns are often used. Another method that has an inherent capacitive pickup rejection can be used is a single loop B-dot probe made of a coaxial cable, as shown in Fig. 3.23(a). The use of this kind of probe is limited to higher frequencies though.

The helicon wave magnetic field detection was performed by measuring the amplitude and phase of axial wave magnetic field, B_z using a single loop high-frequency B-dot probe [2]. The B-dot probe is a single loop of ~ 6 mm diameter made from the shielded coaxial cable, RG 178 (F196, flu-tef industries) of 1.8 mm outer diameter and shown in Fig. 3.23(a)

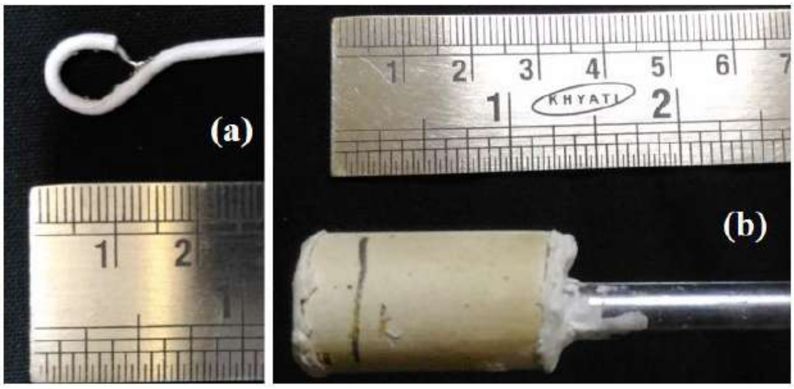

Fig. 3.23**:** Picture of the high-frequency B-dot probe (a) single loop of a coaxial cable, (b) ceramic cover.

The design of B-dot probe is not intended to pick up any electrostatic pickup. The single loop B-dot probe made using coaxial cable is known for inherent electrostatic pickup rejection. At the one end, the co-axial cable is looped, and after the loop, the center conductor is connected to the nearest shielding of the loop. Electrostatic pick up is reduced in this design. The similar types of the probes are checked for electrostatic pickup noise by rotating the probe by 180 degrees. When the probe axis rotated by 180 degree as shown in Fig 3.24, it shows a phase variation of 180 degree and also the signal amplitude is same (< 10 %) as 0 degree as expected for a voltage output induced in the probe due to magnetic field oscillations only. This confirms the inherent capacitive pickup rejection of this single-loop coaxial B-dot probe. The shielding helps in two ways. One it forms a part of the loop and at the same time acts as a shield for electrostatic signals inside the plasma, which are present because of the high RF voltage fluctuations of the plasma potential. Also, the low-frequency signals in the kHz range of frequencies cannot induce enough voltage more than the noise level of the probe to get detected.

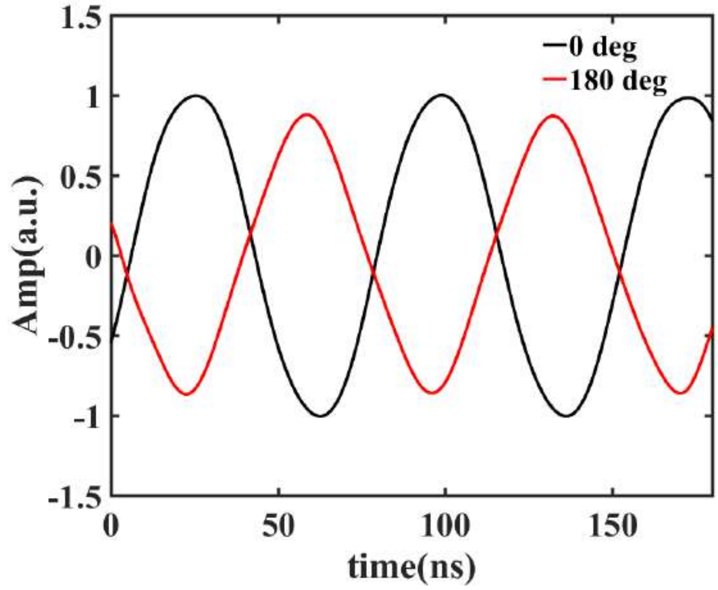

Fig. 3.24: shows the inherent electrostatic pickup rejection by use of a single loop B-dot probe. The probe output for 0 deg (black curve) and 180 deg (red curve) showing the capacitive pickup is negligible.

3.3.9 RF Current probe

An RF current probe (CT) is used to measure the antenna RF current flowing in the antenna circuit. The antenna current is a measure of antenna-plasma resistance and RF power transfer efficiency in any RF plasma system when the reflected power is negligible when compared to the forward power. A CT (model no. CM-10-P, Ion Physics make) is inserted around the antenna transmission line leg just after the match box. This is kept within the RF shielding enclosure. The output of this CT has a calibration factor or sensitivity of 0.1 V/A. The CT has a BNC output which is connected to a 50 Ohm BNC and subsequently the output is monitored with a digital oscilloscope of 1 M-ohm input impedance which necessitates a termination of 50 Ohm before connecting to the oscilloscope. Using the above mentioned calibration factor, the output voltage is noted and later converted to current values. Knowing the values of forward power P_{for}, reflected power P_{ref}, the RMS current value the total antenna resistance can be written as for reflections <1% as

$$R_{tot} = \frac{P_{for} - P_{ref}}{I_{rms}^2} \tag{3.16}$$

Here $R_{tot} = R_A + R_P$ is the sum of the antenna vacuum resistance R_A and the antenna-plasma resistance R_P. The antenna vacuum resistance is calculated by powering the antenna without plasma and noting down the RMS value of antenna current. This vacuum current is used to drive the antenna resistance which is actually the sum of skin resistances (of the antenna, transmission line, and match box inductors), contact resistances of all the frictional electrical connections and eddy current losses. Once R_A is known, the plasma resistance R_P is calculated by subtracting the value of R_A from R_{tot} which is obtained in the presence of the plasma. R_P is the sum of all the plasma processes leading to heating, ionization, and maintaining the plasma thus is a sum of all the capacitive, inductive, and wave coupling depending upon the discharge conditions. The power transfer efficiency η is the ratio of absorbed power P_{abs} and the total supplied RF power P_{tot} and is expressed as follows

$$\eta = \frac{P_{abs}}{P_{tot}} = \frac{R_P}{R_P + R_A} \tag{3.17}$$

The efficiency and plasma resistance both increase when the discharge transitions from a capacitive to inductive to Helicon wave mode.

3.4 Helicon Characterization

Experiments are performed in a HeX device, which has already been described in the previous section (section 3.2). In this thesis basically, two types of helicon modes are studied: one which conventional helicon mode, other the low B helicon mode. The conventional helicon source operates at a magnetic field which corresponds to an electron cyclotron frequency (f_{Ce}), which is $\sim 40\ to\ 200$ times the source frequency (f_{RF}). This means conventional helicon wave mode operation requires the magnetic field around 200 G to 1 kG. The low magnetic field helicon, which is described in the next chapter requires low magnetic field around 20-30 G. The low magnetic field means $f_{ce} \sim 5$ times the source frequency. This section deals with the conventional helicon operation. The conventional helicon mode is identified by the density mode transition.

3.4.1 Antenna Efficiency

The helical antenna serves two purposes, one for RF plasma production and other is helicon wave excitation. The excitation of helicon wave depends on the density production by the antenna through helicon wave dispersion for given magnetic field. Therefore it is required to find out the efficiency of the antenna and its associated circuitry to deliver significant power to the plasma.

To estimate the RF power coupling to the plasma, the power transfer efficiency is calculated using the the Eq. 3.17. Fig. 3.4 shows the equivalent circuit of antenna, which incorporates circuit resistance which includes all the contanct and ohmic resistance and eddy current losses, mathching network and transmission line, and effective inductance, L_A. All the power losses attributed to plasma is included in the plasma resistance, R_P, which includes the power loss due to capacitve, inductive and wave coupling. For every measurement condition the antenna-plasam load should be matched with RF source load, for that reflection power < 1-2 %, the total input power from the RF source must be dissipated in the antenna-plasma system.

The total effective antenna loading resistance, which is related to antenna current is given by, $R_{eff} = R_A + R_P$, and the net power flow to the antenna is given by

$$P_{for} - P_{ref} = I_{rms}^2 R_{eff} \tag{3.18}$$

Where P_{for} and P_{ref} are the forward and reflected powers, respectively and $I_{rms} = I_{RF}/\sqrt{2}$ with I_{RF} is the amplitude of the sinusoidally varying current measured by an RF current probe coaxially held around the reference leg of the transmission line. The external circuit resistance R_A is estimated by measuring the antenna current in the absence of plasma.

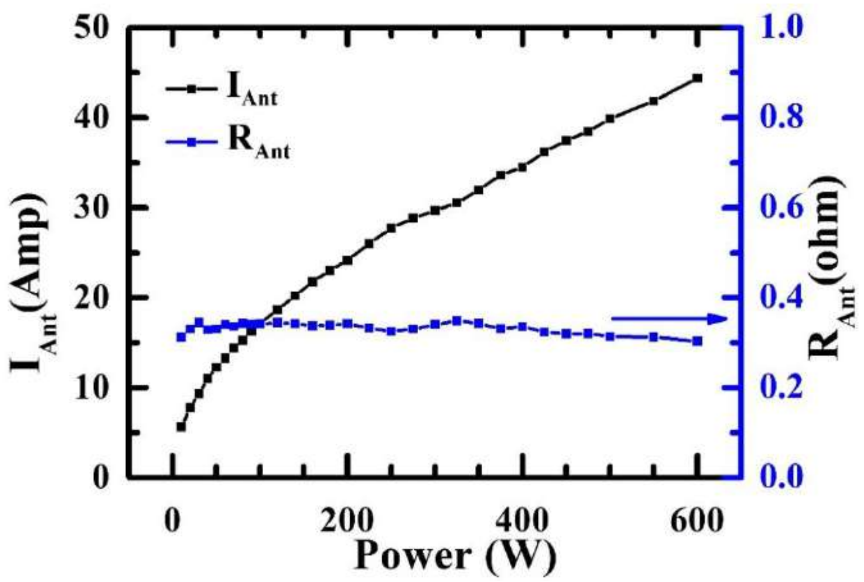

Fig. 3.25: Variation of antenna RMS current and antenna resistance with RF power in vacuum at 1×10^{-5} mbar.

Fig. 3.25 shows the variation of antenna current in a vacuum with RF power at $1 \times 10^{-5}\ mbar$. The estimated value of the antenna resistance R_A is ≈ 0.32 Ohm. Here, all input power is utilized in the matching network-antenna system only.

3.4.2 Discharge mode transition

It is well known that the discharges produced by helicon antenna can operate in capacitive (E), inductive (H) or Helicon wave (W) mode [37–39]. In helicon discharge [3] the modes are named E, H or W, depending whether the dominant electric field responsible for maintaining the discharge is of capacitive, inductive, or of wave origin, respectively. E-H-W mode transitions in helicon discharges are observed by changing the source parameters either of RF power [40–42] and ambient magnetic field [43,44]. These transitions are observed by monitoring the density [37,41,43,44], the Q-factor of matching circuit [37], plasma potential [45], or antenna plasma resistance [40]. To characterize discharge mode transitions, central plasma density, load capacitor, and antenna current were measured for different power at 1×10^{-3}mbar pressure. The source magnetic field is kept at 160 G. The E-H-W mode transitions inferred from the above mentioned measurements are shown in Fig. 3.26. The center plasma density measured in both the source chamber at z = 31 cm (Fig. 3.26(a)) and in the expansion chambers at z = 50 cm (Fig. 3.26(b)) shows the gradual and abrupt changes near 50 W and 700W. The discharge mode transitions evident with the change of the slope of plasma density as well as of antenna current. This kind of change in density is associated with E-H and H-W transitions. The discharge mode transitions are also associated with a discrete change in values of load capacitor (C_L), Fig. 3.26(c) with optimized reflected power less than 2% by keeping the fixed value of tune capacitor (C_T) in the matching network [46].

It should be noted that changes in C_L represent changes in the plasma resistance R_P as $C_L \propto 1/\sqrt{R_P}$ [47]. As evident from the figure, the transitions in density values of Figure 3.26 (a and b) are magnified in C_L plots with clear and distinct transitions well visible. The load capacitance which also measure the antenna plasma loading resistance is nearly constant in each mode. The reason for which the antenna-plasma resistance or C_L are more sensitive to external plasma parameters because it represents a global change, but the density measurement is a single point measurement, which reperesents a local change. The measured values of rms antenna current (I_{ant}) as a function of rf power is shown in Fig. 3.26(d). This measurement also reflects the mode transitions near 50 W and 700 W. It is concluded that discharge mode transition from H to W happens for power ≥700 W. Note that the E-H transition is not very strong in this case. Even H to W transition is not most prominent as some researchers (not all) have seen. These transitions don't always happen to be most prominent especially at low magnetic field < 200 G and at low pressure $< 1 \times 10^{-3}$ torr. These transitions become more prominent at higher magnetic field and at the higher pressure. It is even less prominent when density is measured far from the antenna. In our case, density is measured 30 cm away from the antenna center. Moreover, the magnetic field and operating pressure are lower in the present experiment. In addition to this, the effect of capacitive coupling cannot be neglected in both H and W mode until one uses the Faraday shield. The presence of a significant part of capacitive coupling gives the gradual E-H transition in our experiment.

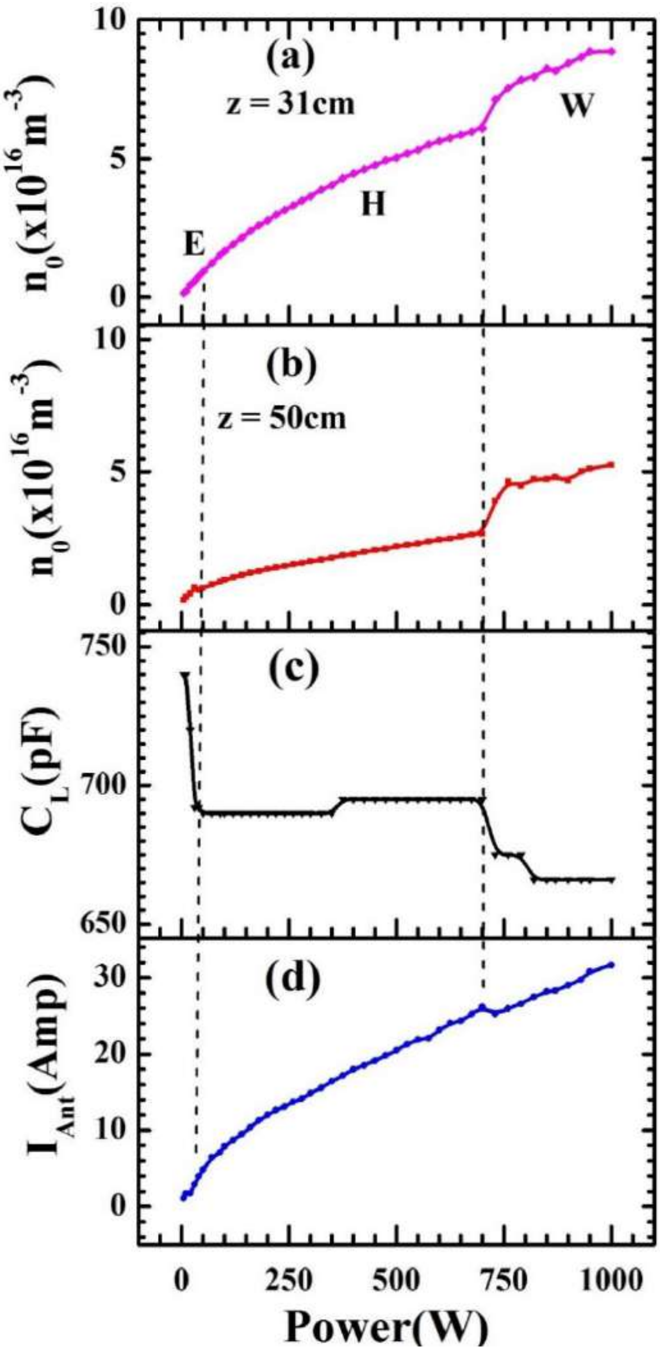

Fig. 3.26: Helicon discharge mode transitions. Langmuir probe measurement of center plasma density at (a) z = 31 cm, (b) z = 50 cm and (c) Value of load capacitor (C_L) and (d) Antenna rms current as function of rf power, measured at 1×10^{-3} mbar and $B_0 \approx 160$ G (I_B = 87 A). Dash lines show the capacitive (E) to inductive (H) and inductive (H) to helicon wave (W) mode transitions.

To prove the above discussed points that prominent discharge mode transitions need the higher magnetic field and higher pressure, the discharge mode transitions are measured at the antenna center at z = 0 cm for higher fill pressure 2×10^{-3} mbar and 200 G magnetic field. The result is shown in Fig. 3.27. At the antenna center, the transitions are clearly evident in the plasma density (Fig. 3.27(a)) as well as in the load capacitor (Fig. 3.27 (b)) and antenna current (Fig. 3.27(c)). Two dash lines indicate the transitions from E-H and H-W.

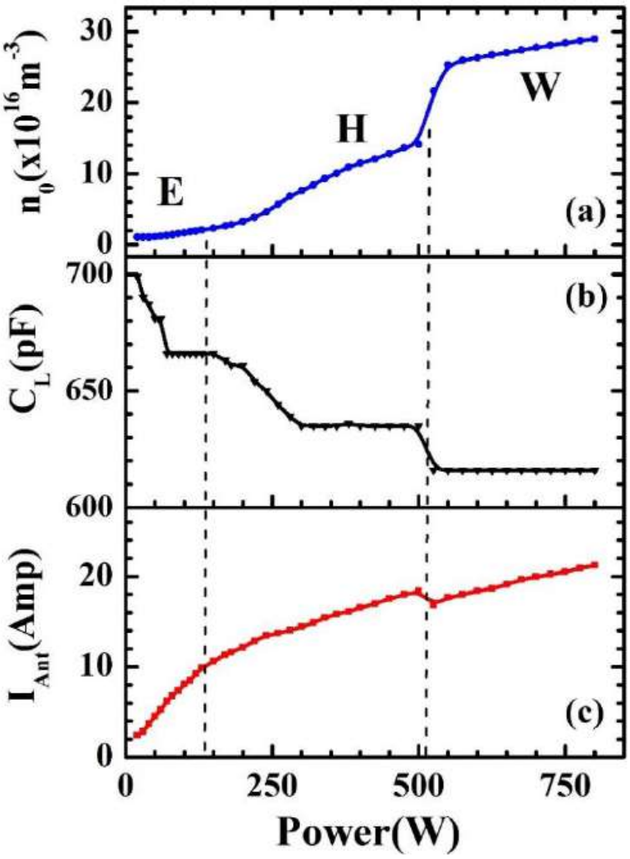

Fig. 3.27: Helicon discharge mode transitions. Langmuir probe measurement of center plasma density at (a) z = 0 cm (b) Value of load capacitor (C_L) and (c) Antenna rms current (I_{ant}) as function of RF power, measured at 2×10^{-3} mbar and $B_0 \approx 200$ G

Further measurements are performed with different fill pressures; the plasma density is measured at z = 31 cm along with load capacitor value. The results are shown in Fig. 3.28. The E-H transition is not very clear in density due to measurement performed far away from the antenna. However, the transition for H-W is clearly seen in the density. The load capacitor also indicates the transitions for E-H and H-W. As pressure increases the power requirements to H-W transition decreases.

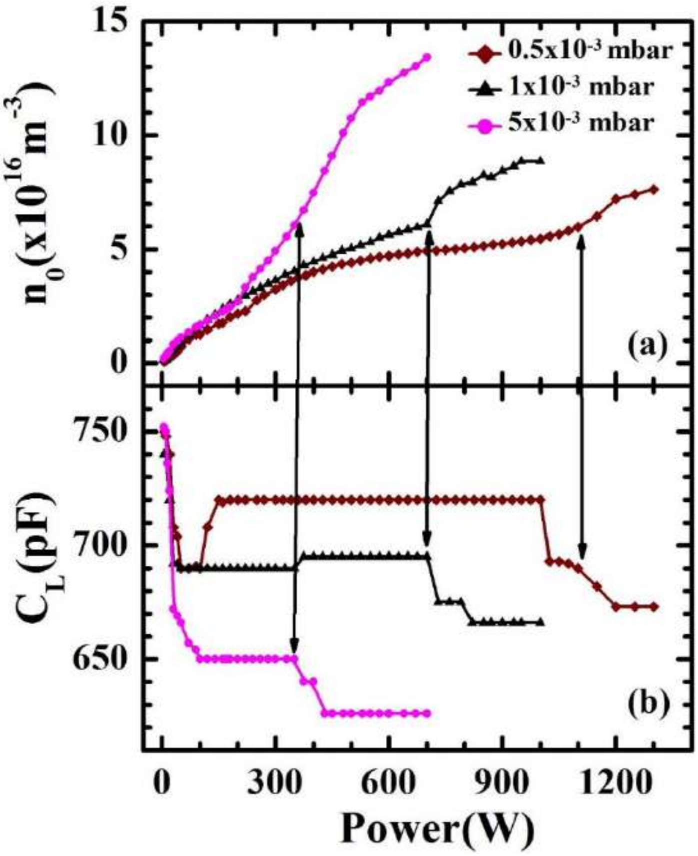

Fig. 3.28: Mode transitions observed at 160 Gauss for different Argon pressures by varying the RF power. Transitions are observed in (a) density at z = 31 cm and (b) in load capacitor values of the matching network.

3.5 Summary

The Helicon Experimental device (HeX) is discussed in detail. Various electric and magnetic probes with their electronics are designed, developed and tested in the plasma. Working principles of all the diagnostics are discussed. Antenna vacuum resistance measured without plasma using the current probe. The helicon mode is characterized using the mode transition method. Discharge mode transitions observed at the center of the antenna is more prominent than away from the antenna. Mode transitions are also observed at different discharge pressure. The power required to obtain the helicon mode decreases as pressure increases.

References

[1] Melazzi D and Lancellotti V 2015 A comparative study of radiofrequency antennas for Helicon plasma sources *Plasma Sources Sci. Technol.* **24** 025024

[2] Light M and Chen F F 1995 Helicon wave excitation with helical antennas *Phys. Plasmas* **2** 1084–93

[3] Kamenski I V. and Borg G G 1996 An evaluation of different antenna designs for helicon wave excitation in a cylindrical plasma source *Phys. Plasmas* **3** 4396–409

[4] S M Yun D A and F F C L P 2003 Superiority of half-wavelength helicon antennae *Plasma Sources Sci. Technol.* **12** 287–93

[5] Miljak D G and Chen F F 1998 Helicon wave excitation with rotating antenna fields *Plasma Sources Sci. Technol.* **7** 61–74

[6] R. F. Holsinger and K. Halbach 2013 Download Area for Poisson Superfish *Los Alamos Natl. Lab.*

[7] Mott-Smith H M and Langmuir I 1926 The Theory of Collectors in Gaseous Discharges *Phys. Rev.* **28** 727–63

[8] Hutchinson I H 2002 *Principles of Plasma Diagnostics: Second Edition* vol 44

[9] Chen F F 2003 Langmuir Probe Diagnostics *Mini-Course on Plasma Diagnostics, IEEE-ICOPS meeting, Jeju, Korea* (Elsevier)

[10] Lieberman M A and Lichtenberg A J 2005 *Principles of Plasma Discharges and*

Materials Processing (Hoboken, NJ, USA: John Wiley & Sons, Inc.)

[11] Batani D, Alba S, Lombardi P and Galassi A 1997 Use of Langmuir probes in a weakly ionized, steady-state plasma with strong magnetic field *Rev. Sci. Instrum.* **68** 4043–50

[12] Bose S, Kaur M, Chattopadhyay P K, Ghosh J, Saxena Y C and Pal R 2017 Langmuir probe in collisionless and collisional plasma including dusty plasma *J. Plasma Phys.* **83** 615830201

[13] Jeon S J, Eom G S, Kim J H and Choe W 2002 Multichannel rf-compensated Langmuir probe array driven by a single bias supply *Rev. Sci. Instrum.* **73** 277–82

[14] Sudit I D and Chen F F 1994 RF compensated probes for high-density discharges *Plasma Sources Sci. Technol.* **3** 162–8

[15] Wendt A E 2001 Passive external radio frequency filter for Langmuir probes *Rev. Sci. Instrum.* **72** 2926–30

[16] Oksuz L, Soberón F and Ellingboe A R 2006 Analysis of uncompensated Langmuir probe characteristics in radio-frequency discharges revisited *J. Appl. Phys.* **99** 013304

[17] Paranjpe A P, McVittie J P and Self S A 1990 A tuned Langmuir probe for measurements in rf glow discharges *J. Appl. Phys.* **67** 6718–27

[18] Annaratone B M and Braithwaite N S J 1991 A comparison of a passive (filtered) and an active (driven) probe for RF plasma diagnostics *Meas. Sci. Technol.* **2**

795–800

[19] Braithwaite N S J, Benjamin N M P and Allen J E 1987 An electrostatic probe technique for RF plasma *J. Phys. E.* **20** 1046–9

[20] Godyak V A, Piejak R B and Alexandrovich B M 1992 Measurement of electron energy distribution in low-pressure RF discharges *Plasma Sources Sci. Technol.* **1** 36–58

[21] Chen F F 1965 Saturation Ion Currents to Langmuir Probes *J. Appl. Phys.* **36** 675–8

[22] Chen F F 2001 Langmuir probe analysis for high density plasmas *Phys. Plasmas* **8** 3029–41

[23] Sheehan J P, Raitses Y, Hershkowitz N, Kaganovich I and Fisch N J 2011 A comparison of emissive probe techniques for electric potential measurements in a complex plasma *Phys. Plasmas* **18** 073501

[24] Umair Siddiqui M and Hershkowitz N 2014 Double layer-like structures in the core of an argon helicon plasma source with uniform magnetic fields *Phys. Plasmas* **21** 020707

[25] Brown I G 1971 Response of a Langmuir Probe in a Strong Magnetic Field *Phys. Fluids* **14** 1377

[26] Sugai H, Ghanashev I, Hosokawa M, Mizuno K, Nakamura K, Toyoda H and Yamauchi K 2001 Electron energy distribution functions and the influence on fluorocarbon plasma chemistry *Plasma Sources Sci. Technol.* **10** 378–85

[27] Neumann G, Kammeyer M and Schneemann B 1995 Personal-computer-based control and evaluation of Langmuir probe characteristics *Meas. Sci. Technol.* **6** 391–9

[28] Takahashi K, Charles C, Boswell R W and Fujiwara T 2011 Electron Energy Distribution of a Current-Free Double Layer: Druyvesteyn Theory and Experiments *Phys. Rev. Lett.* **107** 035002

[29] Takahashi K, Charles C, Boswell R, Lieberman M A and Hatakeyama R 2010 Characterization of the temperature of free electrons diffusing from a magnetically expanding current-free double layer plasma *J. Phys. D. Appl. Phys.* **43** 162001

[30] Sheehan J P and Hershkowitz N 2011 Emissive probes *Plasma Sources Sci. Technol.* **20** 063001

[31] Hershkowitz N 1989 *Plasma Diagnostics* (Elsevier)

[32] Smith J R, Hershkowitz N and Coakley P 1979 Inflection-point method of interpreting emissive probe characteristics *Rev. Sci. Instrum.* **50** 210–8

[33] Hoffmann C R and Lees D J 1971 A differential method of measuring plasma potential *Plasma Phys.* **13** 689–91

[34] Reilly M P, Lewis W and Miley G H 2009 Magnetic field probes for use in radio frequency plasma *Rev. Sci. Instrum.* **80** 053508

[35] Franck C M, Grulke O and Klinger T 2002 Magnetic fluctuation probe design and capacitive pickup rejection *Rev. Sci. Instrum.* **73** 3768–71

[36] Everson E T, Pribyl P, Constantin C G, Zylstra A, Schaeffer D, Kugland N L and Niemann C 2009 Design, construction, and calibration of a three-axis, high-frequency magnetic probe (B-dot probe) as a diagnostic for exploding plasmas *Rev. Sci. Instrum.* **80** 113505

[37] Perry A J 1991 The application of the helicon source to plasma processing *J. Vac. Sci. Technol. B Microelectron. Nanom. Struct.* **9** 310

[38] Degeling A W, Jung C O, Boswell R W and Ellingboe A R 1996 Plasma production from helicon waves *Phys. Plasmas* **3** 2788–96

[39] Chen F F and Boswell R W 1997 Helicons-the past decade *IEEE Trans. Plasma Sci.* **25** 1245–57

[40] Chi K-K, Sheridan T E and Boswell R W 1999 Resonant cavity modes of a bounded helicon discharge *Plasma Sources Sci. Technol.* **8** 421–31

[41] Ellingboe A R and Boswell R W 1996 Capacitive, inductive and helicon-wave modes of operation of a helicon plasma source *Phys. Plasmas* **3** 2797–804

[42] Franck C M, Grulke O and Klinger T 2003 Mode transitions in helicon discharges *Phys. Plasmas* **10** 323–5

[43] Boswell R W 1984 Very efficient plasma generation by whistler waves near the lower hybrid frequency *Plasma Phys. Control. Fusion* **26** 1147–62

[44] Blackwell D D and Chen F F 1997 Two-dimensional imaging of a helicon discharge *Plasma Sources Sci. Technol.* **6** 569–76

[45] Perry A, Conway G, Boswell R and Persing H 2002 Modulated plasma

potentials and cross field diffusion in a Helicon plasma *Phys. Plasmas* **9** 3171–7

[46] Barada K K, Chattopadhyay P K, Ghosh J, Kumar S and Saxena Y C 2012 A linear helicon plasma device with controllable magnetic field gradient *Rev. Sci. Instrum.* **83** 063501

[47] Chen F F 1992 *Capacitor tuning circuits for inductive loads. pdf UCLA Rept.*

Chapter 4
Low magnetic field helicon in non-uniform magnetic field

4.1 Introduction

Helicon plasmas are inherently very efficient for producing high-density plasma. These plasma sources are extensively studied for their application as an economic plasma source for micro-electronics industry [1], negative ion production [2], neutron generation [3] and space propulsion [4]. Coupling of power from helicon antenna to plasma occurs through different coupling mechanisms. At very low power and low magnetic field, the coupling happens through capacitive mode. As power and magnetic field increases, coupling happens through inductive mode and finally through helicon mode. Out of these three modes, the helicon mode exhibits the maximum production efficiency [5,6]. Conventional helicon sources operate at a magnetic field which corresponds to an electron cyclotron frequency (f_{ce}), which is ~ 40 to 200 times of source frequency. This means the wave mode of operation requires 200 G to 1 kG of magnetic field at 13.56 MHz source frequency [7–10]. The necessary power to achieve helicon wave mode is moderately high (> 800 W) depending upon the diameter of plasma (~10 cm) and neutral pressure (~ 10^{-3} Torr). However, even at a low magnetic field (20-30 G) and at low power (~ 100 W for plasmas with 10 cm of diameter) wave mode can be excited[11]. In this operational regime, helicon sources have shown resonance absorption, even around a particular low magnetic field (20-30 G). Here, low magnetic field means f_{ce} ~ 5 times the source frequency. Since the generation of low magnetic field requires less electric power for the electromagnets and less physical weight of the source, these types of low-field helicon sources are attractive for space propulsion [12–14]. It can also be used as a source for semiconductor applications [15], which can drastically reduce the cost of the magnet power supply.

Resonance absorption at low magnetic fields [10,16–23] less than 100 G in a helicon discharge creates a local density peak around a narrow window of magnetic field values contrary to its behavior of monotonically increasing densities at higher magnetic fields[24]. It is important to note here that all these experiments are carried out using uniform magnetic fields near the antenna. Few previous works [25–28] have also been reported with a non-uniform magnetic field near the antenna. In those experiments, non-uniformity in a magnetic field has been created by different combinations of magnetic-coil currents, and a substantial increase in plasma density with the nonuniform magnetic field has been reported. Previous experiments in our device have also reported observations of low-magnetic field (low-B) helicon plasmas[23]. In general, the power coupling and absorption mechanism are complicated, and different theoretical explanations have been proposed to explain the low-B helicon plasmas. Wave-particle trapping [10,11], heating of electrons by Travelpiece-Gould (TG) [29–31] and parametric decay of helicon mode into ion acoustics and TG modes [32] are proposed as different possible schemes for helicon mode coupling. Our earlier results [23] on the density peaking phenomena, in a uniform low magnetic field near source, showed that density increase was due to the resonance behavior when helicon wave propagates near resonance cone boundary. Signature [23] of excitation of low-frequency electrostatic fluctuations supports this hypothesis. We have also observed multiple density-peaks at different values of a low magnetic field.

This observation has been explained by the existence of different eigen-modes in the system [23].

Though right helical antenna predominantly excites helicon waves with a wavelength twice the antenna length, it also excites other wavelengths. This is the case when the magnetic field is uniform. In the uniform magnetic field, there are some studies on wave absorption which depends on the antenna spectrum in a plasma with nonuniform radial density profile [33]. No theoretical studies have yet been reported for antenna spectrum and corresponding absorption for a non-uniform magnetic field near the antenna. For a non-uniform magnetic field, the relative dominance of antenna spectrum may be different. This might lead to different coupling efficiency and might lead to higher production efficiency. Hence, experimentally studying of density peaking behavior in non-uniform magnetic fields are addressed in this chapter.

In the present work, plasma production efficiency is studied by applying different non-uniform magnetic field configurations near the helicon antenna. The density increases with increasing non-uniformity of the applied magnetic field near the antenna. The plasma density is found to be highest at particular non-uniform magnetic field configuration at low B conditions in our experiments. These results are presumably due to different antenna spectrum and absorption efficiency in the presence of non-uniform magnetic fields near the antenna.

The rest of the chapter is organized as follows. Section 4.2 describes the way to produce different non-uniform magnetic field configurations. This section is followed by experimental results and discussion of results in section 4.3. Finally, a summary is presented in section 4.4.

4.2 Magnetic field configurations

The experiments reported here are performed in a HeX device [34,35] and the schematics of which is shown in Fig. 4.1. The whole chamber is evacuated to a base pressure of 1×10^{-6} mbar by a diffusion pump connected to the expansion chamber. Argon is used as the working gas and experiments are carried out at a pressure of around 1×10^{-3} mbar. The axial location of the antenna center is defined as z = 0 cm, and all other axial locations are with reference to this antenna center, as shown in Fig. 4.1.

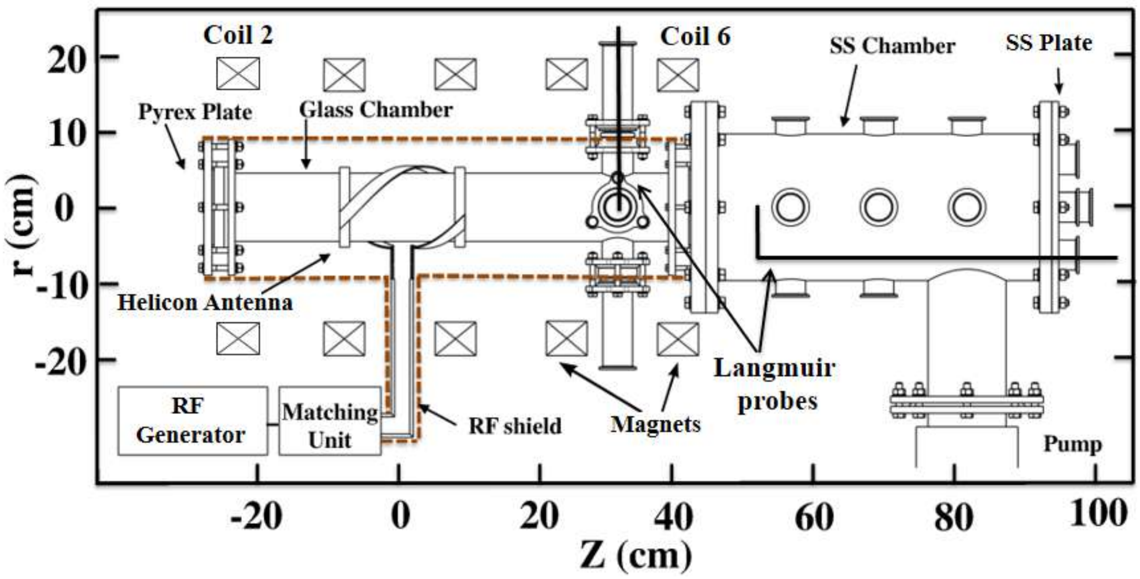

Fig. 4.1: Schematic diagram of the Helicon eXperimental (HeX) device.

Out of eight, five water-cooled electromagnet coils, as shown in Fig. 4.1 are used to generate an axial magnetic field (B_0). Four different magnetic field configurations are used in our experiments, produced by passing direct current (DC) through different electromagnet combinations. These four magnetic configurations are entitled by Case A, B, C, and D. The leftmost coil, as shown in Fig. 4.1, is the second coil, and the rightmost coil is the sixth coil. Case A corresponds to a magnetic field profile when 1 A current is passed through 2-6 coils. Case B magnetic field is produced by excluding the second coil and keeping 3-6 coils. Case C magnetic field is obtained by excluding the second and third coils from left and keeping the 4-6 coils. Case D magnetic field corresponds to 1 A current in the fifth and sixth coils. Fig. 4.2(a) shows the axial variation of the simulated magnetic field when 1 A DC current is passed through different electromagnet combinations to produce four different magnetic field configurations. Fig. 4.2(b) shows the axial variation of the normalized magnetic field with respect to field value at the antenna center and also indicates the magnetic field inhomogeneity in each configuration.

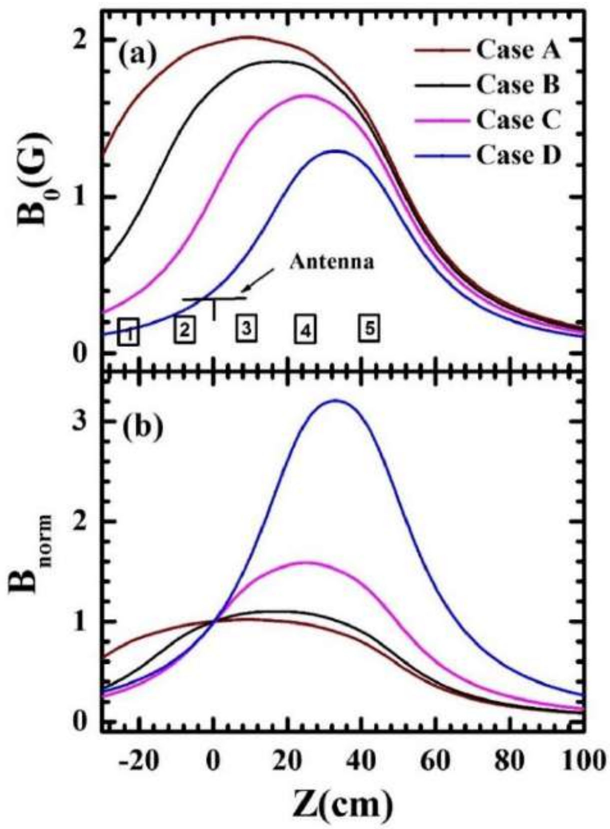

Fig. 4.2: Axial variation of (a) magnetic field when 1 A current is passed in the coils and (b) normalized magnetic field with respect to field value at the antenna center for cases A-D.

Two single RF compensated Langmuir probes [35], as shown in Fig. 4.1, are used to measure the plasma density, n_0. One straight probe, inserted from the top radial port in the source chamber at z = 31 cm and other L-shaped, inserted off-axially from the end flange of the expansion chamber at z = 50 cm. These axial probed locations also correspond to before and after the magnetic and geometric expansion. The helicon wave field detection is performed by measuring the amplitude and phase of axial wave magnetic field, B_z using a single loop high frequency B-dot probe [36]. These measurements start from z = 10 cm with a 2 cm axial increment downstream. To measure the axial phase variation, the antenna current was simultaneously measured using a high-frequency Rogowski coil around the antenna leg, which acts as a phase reference. Antenna current and B-dot probe signals are fed to separate channels of a digital oscilloscope through a high-frequency 9-15 MHz minicircuits® bandpass filter.

4.3 Results and Discussion

The density peaks at critical low magnetic fields have already been observed in our experimental device when a uniform magnetic field is applied near the antenna in the source chamber [23]. In the present experiment, the phenomenon of density peaking at the low magnetic field is further explored by changing the non-uniformity of the axial magnetic field near the antenna location. The n_0 is measured for the four different axial magnetic field configurations. These different magnetic field configurations are labeled by case A, B, C, and D, as shown in Fig. 4.2. For the all presented cases (A, B, C, and D) the values of the magnetic field at abscissa are taken at the antenna center, i.e. z = 0 cm.

Fig. 4.3(a) and 4.3(b) show the variation of n_0 as a function of the magnetic field for case B for different RF powers at z = 31 cm and z = 50 cm respectively. As the magnetic field is slowly increased from 0 G, the density rises monotonically till 15 G (at 300 W) to 25 G (at 600 W), before falling sharply to about half of its peak value near 50-60 G in the source chamber, at z = 31 cm (Fig. 4.3(a)). The signature of low magnetic field density peaking phenomena is also present in the bigger expansion chamber (see Fig. 4.3(b)). The density rise in the expansion chamber (far away from the antenna) is monotonic till 25-40 G, but the fall is rather gradual than that in the source chamber.

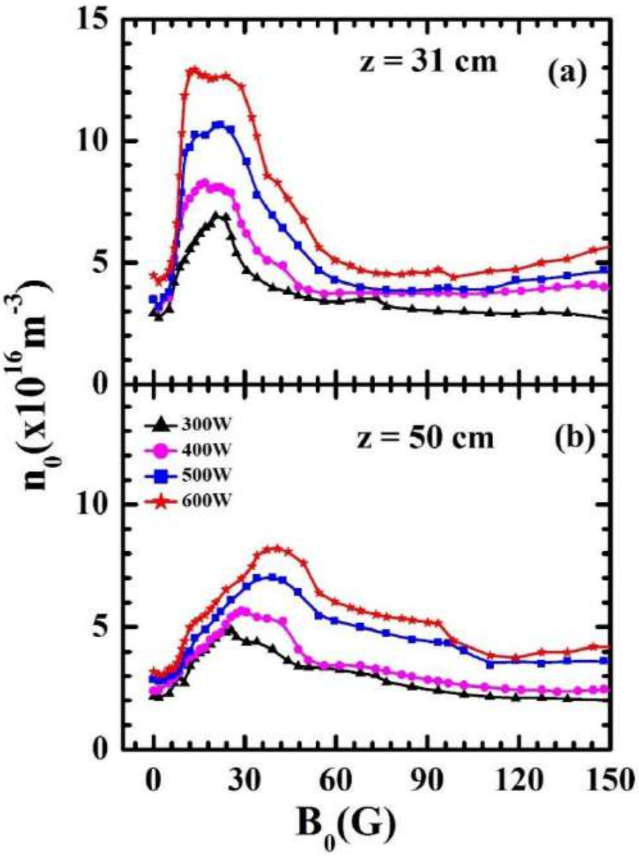

Fig. 4.3: On-axis plasma density variations with magnetic field at antenna center for case B measured in (a) the source chamber at z = 31 cm and (b) the expansion chamber at z = 50 cm, for different values of RF powers 300 W (solid triangles), 400 W (solid circle), 500 W (solid square), and 600 W (solid star).

The value of the peak density increases and the n_0 vs B_0 profiles become broader for increased RF powers both in source and diffusion chambers. It should also be noted that the density peak is shifted to larger magnetic field values when RF power is increased. Similar observations are also found in previous experiments [11,21,29].

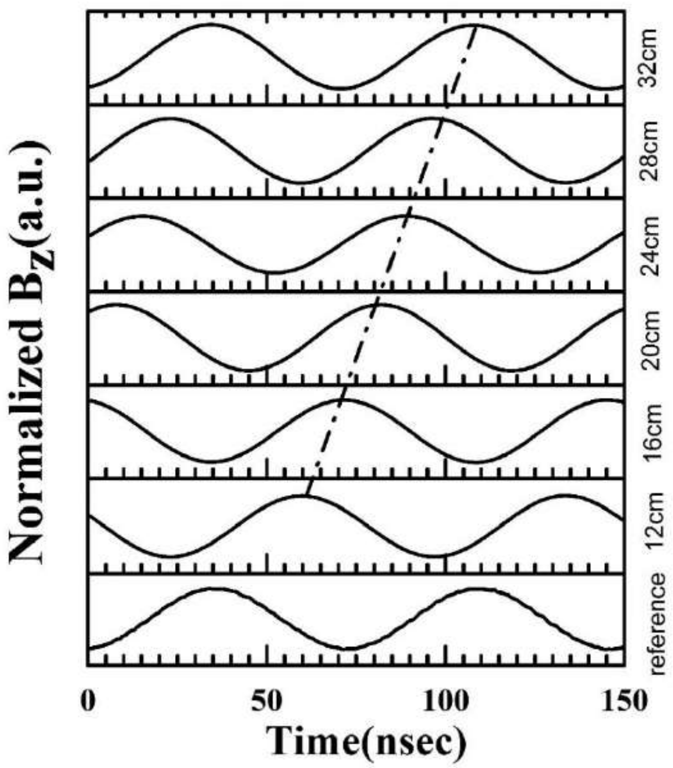

Fig. 4.4: Axial wave magnetic field (B_z) variation at the different axial location for case B; for magnetic field 22 G and RF power 400 W and pressure 1×10^{-3} mbar.

It has already been established that the density peaking at low magnetic field values is the result of wave coupling rather than capacitive or inductive coupling [23,28]. It was shown that the wave propagation near the resonance cone surface causes significant power absorption. To establish the existence of helicon waves, the measurement of phase and amplitude of axial wave magnetic field B_z, are carried out using a single loop B-dot probe.

Fig. 4.4 shows the axial variations of normalized B-dot probe signals with the Rogowski coil measured antenna current serving as a phase reference for 22 G, 400 W, and 1×10^{-3} mbar fill in pressure in case B configuration. It is seen in Fig. 4.4 that the phase is varying with axial locations indicative of a propagating wave. Fig. 4.5 shows the axial variations of amplitude and phase of B_z at 400 W RF power in case B at three magnetic field values at the antenna center. At 22 G, the axial variation of wave amplitude, B_z (Fig. 4.5(a)) has a spatial modulation, and the phase variations (Fig. 4.5(b)) demonstrate the traveling wave character. This type of B_z amplitude modulation can be explained by the beating of different helicon wave modes corresponding to the presence of fundamental and higher-order radial modes [17,37,38]. An effective traveling wavelength can be found by the slope $\frac{d\phi}{dz}$ of a fitted straight line to the axial phase variation (Fig. 4.5(b)), where ϕ is the phase difference. At 22 G, in the near field of the antenna, the effective traveling wavelength, $\lambda_{\parallel} = 360\left(\frac{d\phi}{dz}\right)^{-1}$ is ~ 34 cm, which is approximately twice the length of the antenna. At 50 G, the phase variation (Fig. (4.5(b)) indicates the presence of a helicon wave with a larger wavelength of ~ 70 cm. At 100 G the phase varies very slowly denoting that the wavelength may be larger than the system size. This increase in wavelength is also supported by the lower values of plasma density at 50 and 100 G, as shown in Fig. 4.3, which is in accordance with the helicon dispersion relation.

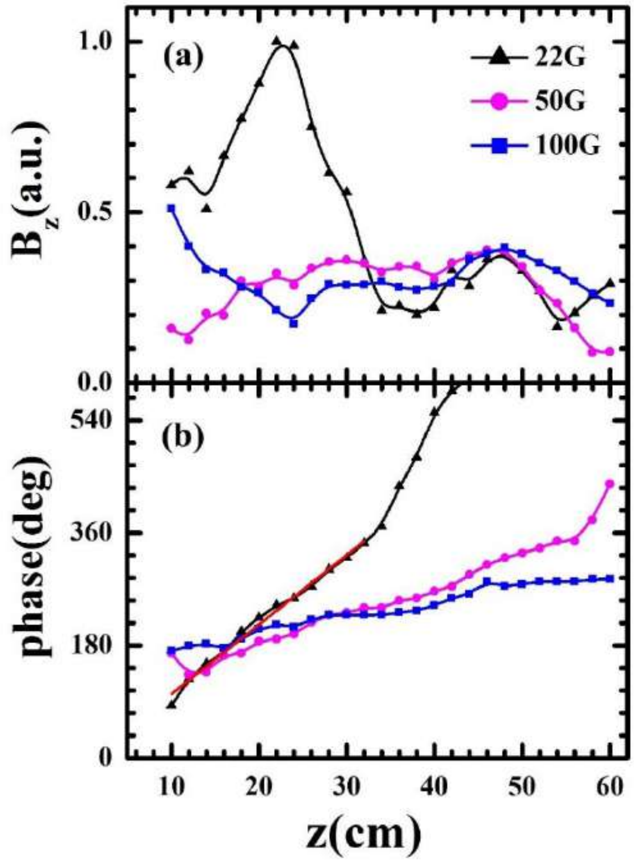

Fig. 4.5: Axial variation of (a) amplitude and (b) phase of an axial component of the wave magnetic field (B_z) at 400 W RF power and 1×10^{-3} mbar for the case B at magnetic field value 22 G (solid triangles), 50 G (solid circle) and 100 G (solid square).

The propagation angle with respect to the axial magnetic field of these obliquely propagating helicon waves can be found from the relation, $cos\theta = \frac{k_\parallel}{k}$, where $k = \sqrt{k_\parallel^2 + k_\perp^2}$, $k_\parallel$ and $k_\perp$ are the total, parallel, and perpendicular wavenumbers, respectively. The calculated value of wave propagation angle at 22 G comes to about 76.4^0 by using the measured values of parallel wavenumber, i.e. $k_\parallel = 18.4$ m^{-1} and estimated perpendicular wavenumber$k_{\perp 1}$. The value of $k_{\perp 1} = \frac{3.83}{a} = 76.6$ m^{-1} can be found from the 1st root of the first-order Bessel function $J_1(k_\perp a)$, by considering the plasma radius a = 5 cm [39]. The calculated value of resonance cone angle [23], $cos\theta = \frac{\omega}{\omega_{ce}}$, for 22 G at which the density peak occurs (Fig. 4.3(a)), is about 77.3^0. It is found that the helicon wave propagation angle well matches with the resonance cone angle. The details of the relation between resonance cone angle and the wave propagation angle are described in reference 28.

The absorption of the helicon wave near the resonance cone surface is correlated with the excitation of electrostatic fluctuations [23,40–42]. In the present experiment, the measurements of density fluctuations are performed at the magnetic field values where helicon wave is present and absent. For this, an RF compensation Langmuir probe biased to collect ion saturation current is placed in the source chamber at (r, z) = (0 cm, 31 cm). A 14-bit PXI based data acquisition system is used to acquire the time series with a low pass filter of 1.9 MHz with 50 k samples of record length at the sampling rate of 100 ks/s. The frequency spectrum (FFT) of density fluctuation at 400 W RF power and 1×10^{-3} mbar fill pressure for various magnetic field strength in case B is shown in Fig. 4.6. At 22 G, the frequency spectra shows two coherent peaks, one at ~ 15 kHz and other at ~30 kHz with reduced amplitude. Preliminary investigation suggests that the observed frequency peak at ~ 15 kHz is electrostatic in nature and may be related to ion-acoustic like wave [43–46]. Further, the spectral peak at ~30 kHz may be a harmonics of the peak at ~ 15 kHz. In contrary, at 50 G or 100 G, these low-frequency peaks remained absent. The presence of electrostatic fluctuations at the low magnetic field (~22 G) is correlated with the density peaking (Fig. 4.3). The electrostatic fluctuations for the magnetic field of 50 G or 100 G are much smaller than they are at 22 G.

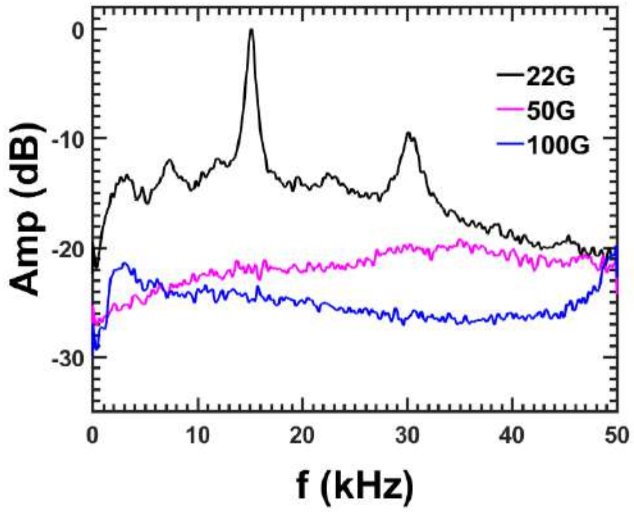

Fig. 4.6: The frequency spectrum of plasma density fluctuation obtained at the different magnetic field with RF compensated Langmuir probe in case B at the on-axial location of z = 31 cm, 400 W RF power, and 1×10^{-3} mbar fill pressure.

After establishing the presence of the helicon wave for which density peaked at the low magnetic field in the almost uniform magnetic field configuration (case B), the measurement of plasma density in the source chamber is made for other different magnetic field configuration as shown in Fig. 4.2 by cases A, B, C, and D. In all the cases the magnetic field is varied and the density is measured at the location, z = 31 cm at 1×10^{-3} mbar pressure for 600 W (Fig. 4.7(a)) and 300 W (Fig. 4.7(b)) RF powers. To get the same magnetic field at the antenna center (z = 0 cm), different amounts of current are passed for different coil configurations. For case A, i.e., uniform magnetic field (at the antenna location) configuration, density peak is present near 22 G (Fig. 4.7(a)). As the coils are removed, it can be seen from Fig. 4.2, that field non-uniformity is increased from case A to case D. For cases A, B and C the density peaks around 17-22 G and the peak value of density increases as non-uniformity increases from case A to C. With

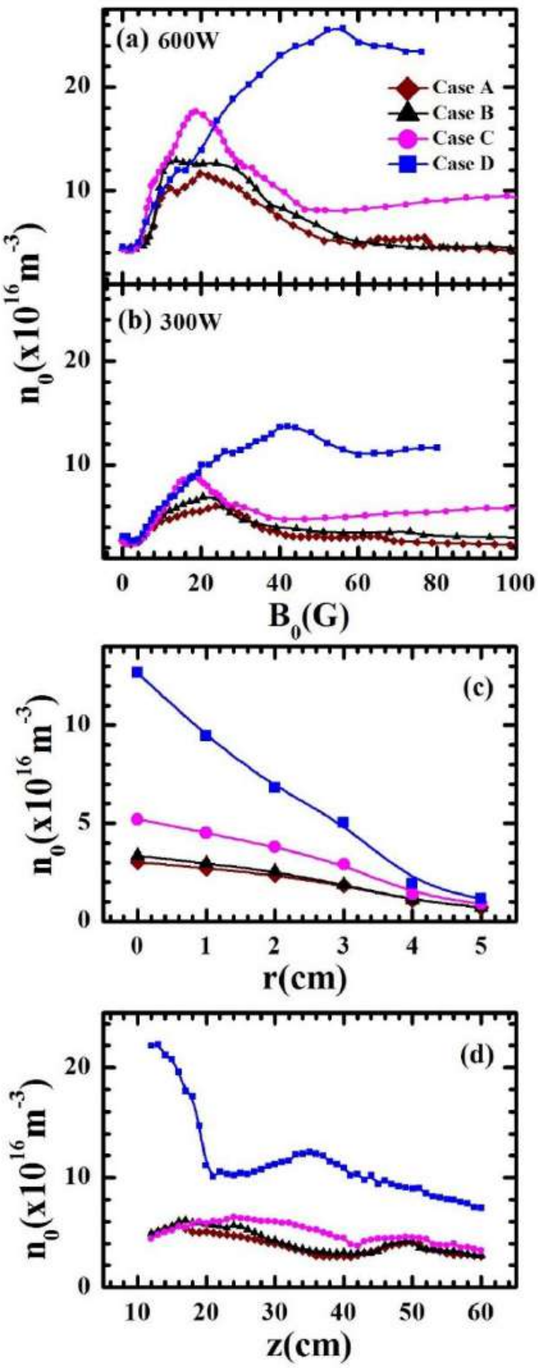

Fig. 4.7: Variation of plasma density in the source chamber at $z = 31\,cm$ with the applied magnetic field at antenna center for cases A-D; at pressure 1×10^{-3} mbar and RF powers (a) 600 W and (b) 300 W. (c) Radial density profile at z = 31cm in case A-D for 300 W, 50 G. (d) On-axis axial variation of the plasma density for the same condition as Fig. 4.7(c).

exclusion of one more coil from the case C, the magnetic field near the antenna becomes more non-uniform which is the case D magnet configuration. In case D, the density peaked around ~ 50-60 G, and the value of density is larger by about five times than the uniform magnetic field case at the same magnetic field value. It has to be noted here that the increase in density has been observed throughout the plasma volume with an increase in the magnetic field non-uniformity from case A to D. This has been verified by measuring the radial and axial plasma density profiles. The radial density profile is shown in Fig. 4.7(c), measured at z = 31cm in case A-D for 300 W, 50 G and 1×10^{-3} mbar fill pressure. Fig. 4.7(d) shows the on-axis axial variation of the plasma density for the same condition as Fig. 4.7(c). Fig. 4.7(d) clearly shows the enhanced plasma density is observed all along the axis in case D. Fig. 4.8 shows the density at 50 G, which increases as the magnetic field non-uniformity increases from case A to D. Results clearly shows a systematic increase of density with increased non-uniformity in the magnetic field near the antenna.

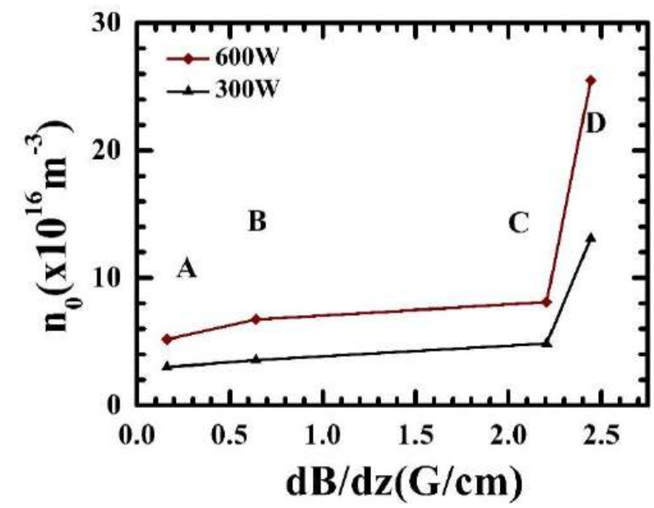

Fig. 4.8: Density as a function of magnetic field non-uniformity at the antenna center in different cases at 50 G and 1×10^{-3} mbar pressure.

To study further the effects of axial magnetic field non-uniformity, antenna plasma coupling efficiencies (Fig. 4.9) and plasma production efficiencies (Fig. 4.10) were estimated. Antenna plasma coupling efficiencies were estimated from the measurement of antenna current in vacuum as well as with plasma.

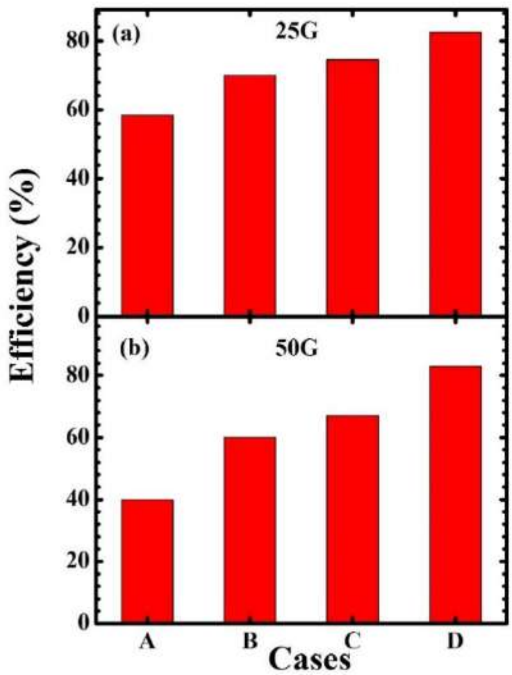

Fig. 4.9: Antenna plasma coupling efficiency at (a) 25 G and (b) 50 G at 300 W and 1×10^{-3} mbar pressure.

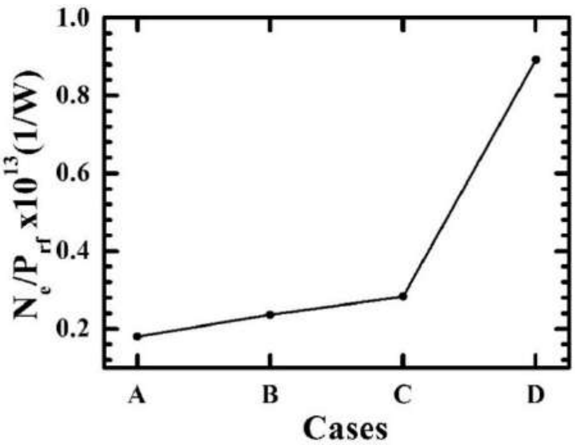

Fig. 4.10: On-axis plasma production efficiency at z = 31 cm, in different cases at 50 G, 600 W and 1×10^{-3} mbar pressure.

Fig. 4.9 shows antenna plasma coupling efficiency at 25 G (Fig. 4.9(a)) and 50 G (Fig. 4.9(b)) for all the magnetic field configurations. It is observed that at 25 G, antenna plasma coupling efficiencies are systematically increased from ~60% to ~80% for A to D configurations. There is 20% increase in efficiency from case A to D and correspondingly there is a slight increase in density. For 50 G, the efficiency decreases for case A, B or C compared to that at 25 G whereas the efficiency is almost the same for case D as is for 25 G. However, the density increases manifold (~ 4 - 5 times) for both 300 W and 600 W RF powers in case D. The observed increase in the plasma density (about 4-5 times around 50 G) in the case D as compared to case B is much higher than the increase in the antenna-plasma coupling efficiency (which is about 20 %). The most plausible reason for this behavior may be given as follows. The total RF coupling efficiency from the antenna to the plasma implicitly includes power coupling to the plasma through capacitive, inductive and helicon mechanisms. However, as the plasma production efficiency is different in different modes, i.e., the helicon mode has higher efficiency of plasma production than the capacitive and inductive modes, variation in the distribution of total power in these three modes may lead to different densities while keeping the total power same. It can be clearly seen in Fig. 4.11 that in case D, the antenna current is less compared to case B, whereas the resistance increases. The decrease in antenna current clearly indicate the decrease in power coupling through inductive mode and hence more power in helicon wave in case D as compared to case B. Therefore, it can be argued that although the “total” RF coupling efficiency from the antenna to the plasma remains small (20 %), the different capabilities of plasma production of different modes (helicon, inductive, capacitive) may lead to different densities in the plasma depending on which mode has got maximum power. Other experiments also support the above arguments. In Lafleur's experiment [28], where the coupling efficiency remains constant for the same input power, however, the density increases as pressure increases. Though they have not reported the antenna current, but it may very well be due to variation of antenna current at different pressures for the same coupled power and total coupling efficiency.

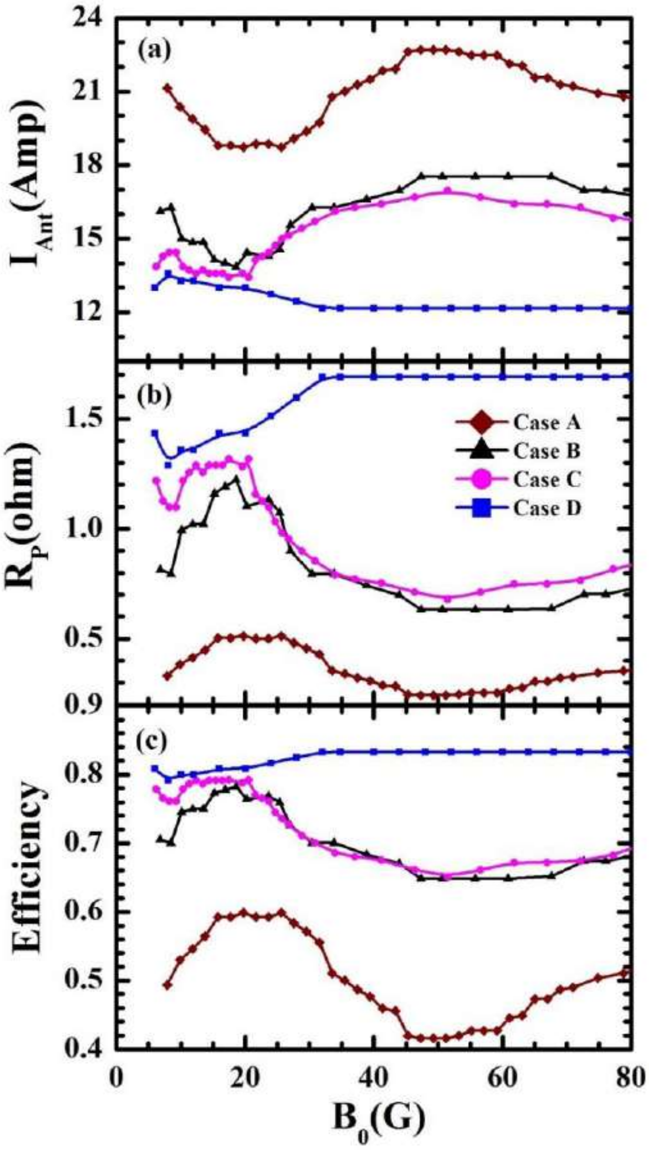

Fig. 4.11: Magnetic field scan of (a) Antenna RMS current (b) Plasma resistance (c) antenna plasma coupling efficiency at 300 W and 1×10^{-3}mbar fill pressure.

The plasma production efficiency [6] $\left(\frac{N_e}{p_{RF}}\right)$ which is the ratio of the number of total electrons to input power also increases with the magnetic field non-uniformity. Fig. 4.10 shows the production efficiency estimated on-axis at z = 31 cm in all four cases for 50 G at 600 W RF power. It is observed that plasma density is increased by fivefold, and also production efficiency is increased by a similar amount. This fivefold increase in density is attributed to higher absorption efficiency of RF power in the plasma. To identify this unusual high absorption, wavenumbers are measured for different cases in two different magnetic fields, as shown in Fig. 12.

Fig. 4.12 shows the axial variation of the amplitude (Fig. 4.12(a) and 4.12(c)) and the phase difference (Fig. 4.12(b) and 4.12(d)) of B_z at two different magnetic field values, 22 G ($\frac{\omega_{ce}}{\omega_0} = 4.5$) and 50 G ($\frac{\omega_{ce}}{\omega_0} = 10$), respectively for case B (solid triangle) and D (solid square) at 400 W RF power and 1×10^{-3} mbar fill in pressure. At 22 G, for both the cases B and D, the phase difference variations (Fig. 4.12(b)) show the wavelength is about 40 cm which is nearly twice the antenna length and the amplitude (Fig. 4.12(a)) modulations show the beating wave pattern. The beating pattern [17,37,38] of amplitude in the presence of a propagating wave indicates the existence of more than one radial modes. In principle, the beating wave pattern can be produced due to wave reflection from the axial boundary of the machine. However, for reflection from the boundary, the wave should have enough strength to reach the boundary. In the present experiments, the system boundary is very far away at z = 95 cm, where the wave amplitude decreases significantly. This suggests that the wave reflection from the axial end wall is unlikely to cause the observed beating patterns. At 50 G, for case B (where

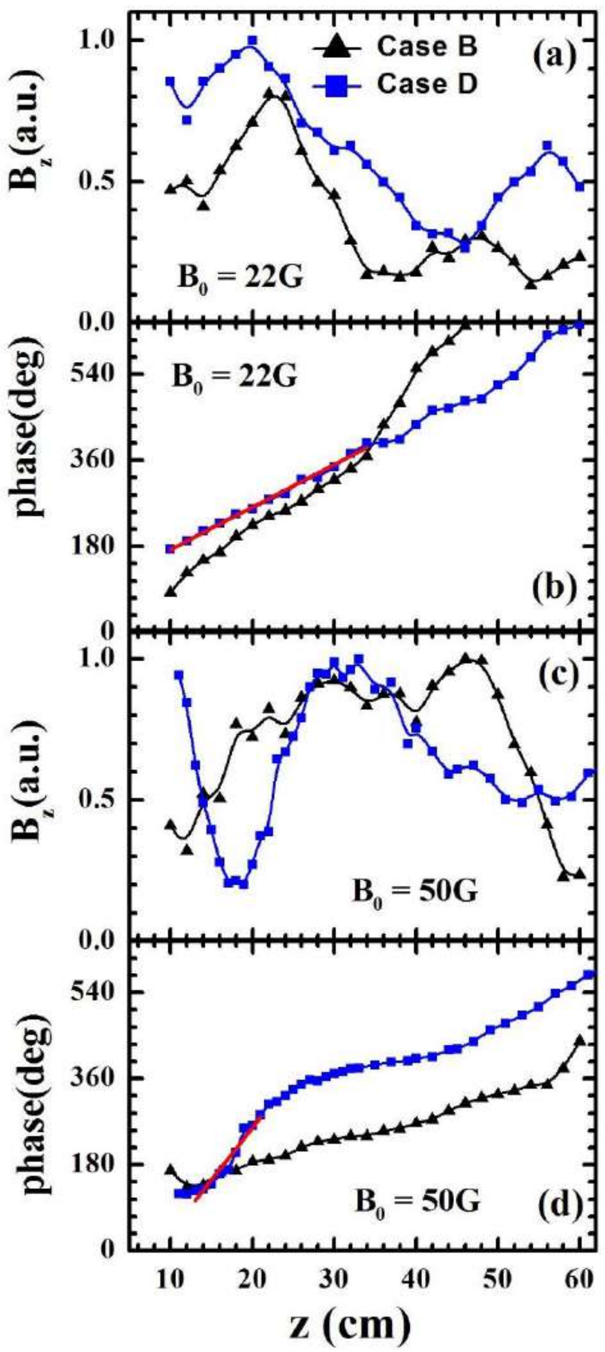

Fig. 4.12: Axial variation of amplitude and phase of B_z for case B (solid triangles) and D (solid squares) magnetic field configuration for 22 G (a and b) and 50 G (c and d) at 400 W RF power and 1×10^{-3} mbar fill pressure.

the density has 5 times lower magnitude from case D), the small phase difference variation shows the wavelength is the order of 70 cm (Fig. 12(d), solid triangles). The contrasting results are observed in the case D at 50 G (where the density is 5 times higher than case B), the wavelength is nearly 20 cm which is close to the length of the antenna. Amplitude variations along the axis shows beat wave in this case also. Excitation of helicon wave with the wavelength equal to the antenna length at 50 G (case D) for most non-uniform magnetic field is not clear. It should be mentioned here that no theoretical studies of antenna plasma coupling exist for a non-uniform magnetic field near the antenna.

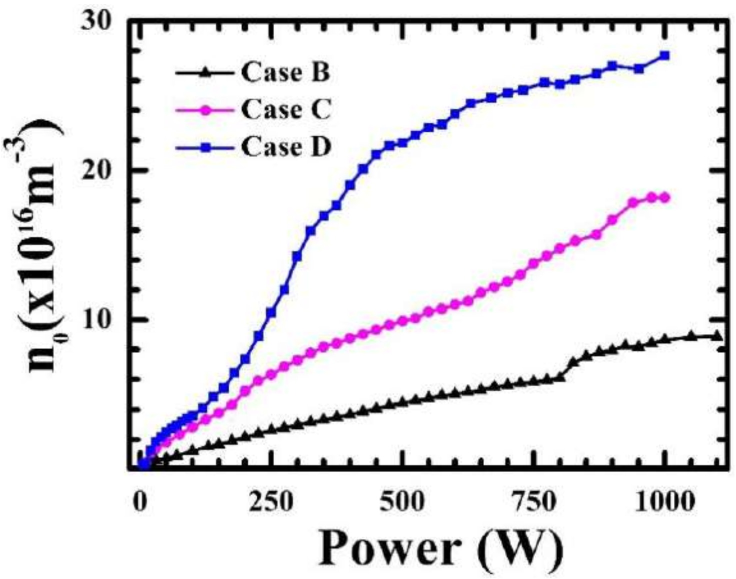

Fig. 4.13: Variation of on-axis plasma density at z = 31 cm with 87 A DC current for cases of B (solid triangle), C (solid circle) and D (solid square) at pressure 1×10^{-3} mbar.

Finally, experiments are carried out at different RF power up to 1000 W, where case B is for conventional helicon and cases C and D are for the non-uniform magnetic field near the antenna. Fig. 4.13 shows the variation of on-axis plasma density with RF powers for cases of B, C, and D at 1×10^{-3} mbar fill pressure. The density in cases B, C, and D is obtained by keeping the fixed DC current, 87 A from the magnet power supply, which corresponds to magnetic field values at the antenna center of about 160, 90 and 34 G, respectively. It is clear from Fig. 4.13 that, below 800 W RF powers, in the case D, density is five times higher than the case B and above 800 W RF powers, in case D, the density is close to four times of the case B. The density at 1000 W, in case B is about 8×10^{16} m^{-3} which is achievable at 200 W in the case D. These results successfully demonstrate that higher plasma production can be achieved with non-uniform magnetic field near the antenna. This should effectively reduce the cost of the magnet power supply and overall power consumption.

4.4 Summary

In the present experiment, four different magnetic field configurations have been used to study the effect of magnetic field inhomogeneity near the helicon antenna center on plasma production and antenna-plasma coupling efficiencies for low magnetic field values. It is shown that the antenna-plasma coupling efficiency increases with increasing the magnetic field inhomogeneity near the antenna. This is also reflected in the increase in density near the antenna. At 25 G, antenna efficiency increases from 60% to 80% for low to high non-uniformity in the magnetic field. Here, the excited wavelength is twice the length of the antenna. However, at 50 G magnetic field at the antenna center, the antenna efficiency remains the same for higher non-uniformity and goes down for less non-uniform cases. Wavelength excited for 50 G magnetic field at the antenna center is the same as antenna length for the most non-uniform magnetic field. The density is the highest in this case. Moreover, density is also less for conventional helicon mode operation (160 G, 800 W in the present case) compared to the non-uniform magnetic field at the same power level.

The response of the plasma to the applied antenna wave fields, i.e., wave absorption is determined by the distribution of antenna current, which sets the wavenumber spectrum. The wavelength spectrum along with spectral power density is related to antenna loading, which is synonymous to plasma resistance. In general, the vacuum power spectrum of a helical antenna has been relatively well studied. In those kinds of literature, antenna plasma coupling (spectral amplitudes) has been addressed considering radial density gradient, different antenna, its polarization, and antenna length. However, these studies don’t consider non-uniform magnetic field. Results obtained from the present experiments show that coupling and absorption in the operation of helicon discharges need to be understood more at least for nonuniform magnetic fields near the antenna. Further study is warranted.

References

[1] Perry A J 1991 The application of the helicon source to plasma processing *J. Vac. Sci. Technol. B Microelectron. Nanom. Struct.* **9** 310

[2] Mieno T, Kamo T, Hayashi D, Shoji T and Kadota K 1996 Efficient production of O + and O − ions in a helicon wave oxygen discharge *Appl. Phys. Lett.* **69** 617–9

[3] Jung H D, Park M J, Kim S H and Hwang Y S 2004 Development of a compact helicon ion source for neutron generators *Rev. Sci. Instrum.* **75** 1878–80

[4] Charles C 2009 Plasmas for spacecraft propulsion *J. Phys. D. Appl. Phys.* **42** 163001

[5] Chi K-K, Sheridan T E and Boswell R W 1999 Resonant cavity modes of a bounded helicon discharge *Plasma Sources Sci. Technol.* **8** 421–31

[6] Shinohara S and Tanikawa T 2004 Development of very large helicon plasma source *Rev. Sci. Instrum.* **75** 1941–6

[7] Zhao G, Wang H, Si X, Ouyang J, Chen Q and Tan C 2017 The discharge characteristics in nitrogen helicon plasma *Phys. Plasmas* **24** 123507

[8] Sharma N, Chakraborty M, Neog N K and Bandyopadhyay M 2018 Development and characterization of a helicon plasma source *Rev. Sci. Instrum.* **89** 083508

[9] Takahashi K, Charles C, Boswell R and Ando A 2013 Performance improvement of a permanent magnet helicon plasma thruster *J. Phys. D. Appl.*

Phys. **46** 352001

[10] Degeling A W, Jung C O, Boswell R W and Ellingboe A R 1996 Plasma production from helicon waves *Phys. Plasmas* **3** 2788–96

[11] Lafleur T, Charles C and Boswell R W 2010 Plasma control by modification of helicon wave propagation in low magnetic fields *Phys. Plasmas* **17** 073508

[12] Chen F F 2008 Permanent Magnet Helicon Source for Ion Propulsion *IEEE Trans. Plasma Sci.* **36** 2095–110

[13] Ling J, West M D, Lafleur T, Charles C and Boswell R W 2010 Thrust measurements in a low-magnetic field high-density mode in the helicon double layer thruster *J. Phys. D. Appl. Phys.* **43** 305203

[14] Harle T, Pottinger S J and Lappas V J 2012 Helicon double layer thruster operation in a low magnetic field mode *Plasma Sources Sci. Technol.* **22** 015015

[15] Sarra-Bournet C, Charles C and Boswell R 2011 Low temperature growth of nanocrystalline TiO2 films with Ar/O2 low-field helicon plasma *Surf. Coatings Technol.* **205** 3939–46

[16] Chen F F, Jiang X, Evans J D, Tynan G and Arnush D 1997 Low-field helicon discharges *Plasma Phys. Control. Fusion* **39** A411–20

[17] Lho T, Hershkowitz N, Miller J, Steer W and Kim G H 1998 Azimuthally symmetric pseudosurface and helicon wave propagation in an inductively coupled plasma at low magnetic field *Phys. Plasmas* **5** 3135–42

[18] Wang S J, Kwak J G, Kim C B and Kim S K 2003 Observation of enhanced

negative hydrogen ion production in weakly magnetized RF plasma *Phys. Lett. A* **313** 278–83

[19] Sato G, Oohara W and Hatakeyama R 2007 Experimental characterization of a density peak at low magnetic fields in a helicon plasma source *Plasma Sources Sci. Technol.* **16** 734–41

[20] Wang S J, Kwak J-G, Kim S K and Cho S 2007 Experimental Study on the Density Peaking of an RF Plasma at a Low Magnetic Field *J. Korean Phys. Soc.* **51** 989

[21] Sato G, Oohara W and Hatakeyama R 2004 Efficient plasma source providing pronounced density peaks in the range of very low magnetic fields *Appl. Phys. Lett.* **85** 4007–9

[22] Eom G S, Kim J and Choe W 2006 Wave mode conversion and mode transition in very high radio frequency helicon plasma *Phys. Plasmas* **13** 073505

[23] Barada K K, Chattopadhyay P K, Ghosh J, Kumar S and Saxena Y C 2013 Observation of low magnetic field density peaks in helicon plasma *Phys. Plasmas* **20** 042119

[24] Chen F F and Boswell R W 1997 Helicons-the past decade *IEEE Trans. Plasma Sci.* **25** 1245–57

[25] Chevalier G and Chen F F 1993 Experimental modeling of inductive discharges *J. Vac. Sci. Technol. A Vacuum, Surfaces, Film.* **11** 1165–71

[26] Braginskii O V., Vasil'eva A N and Kovalev A S 2001 Helicon plasma in a

nonuniform magnetic field *Plasma Phys. Reports* **27** 699–707

[27] Virko V F, Shamrai K P, Virko Y V. and Kirichenko G S 2004 Wave phenomena, hot electrons, and enhanced plasma production in a helicon discharge in a converging magnetic field *Phys. Plasmas* **11** 3888–97

[28] Lafleur T, Charles C and Boswell R W 2011 Characterization of a helicon plasma source in low diverging magnetic fields *J. Phys. D. Appl. Phys.* **44** 055202

[29] Wang Y, Zhao G, Liu Z W, Ouyang J T and Chen Q 2015 Two density peaks in low magnetic field helicon plasma *Phys. Plasmas* **22** 093507

[30] Cho S 2006 The resistance peak of helicon plasmas at low magnetic fields *Phys. Plasmas* **13** 033504

[31] Shamrai K P and Taranov V B 1996 Volume and surface rf power absorption in a helicon plasma source *Plasma Sources Sci. Technol.* **5** 474–91

[32] Lorenz B, Krämer M, Selenin V L and Aliev Y M 2005 Excitation of short-scale fluctuations by parametric decay of helicon waves into ion–sound and Trivelpiece–Gould waves *Plasma Sources Sci. Technol.* **14** 623–35

[33] Arnush D and Chen F F 1998 Generalized theory of helicon waves. II. Excitation and absorption *Phys. Plasmas* **5** 1239–54

[34] Barada K K, Chattopadhyay P K, Ghosh J, Kumar S and Saxena Y C 2012 A linear helicon plasma device with controllable magnetic field gradient *Rev. Sci. Instrum.* **83**

[35] Yadav S, Ghosh S, Bose S, Barada K K, Pal R and Chattopadhyay P K 2018 Role of ion magnetization in formation of radial density profile in magnetically expanding plasma produced by helicon antenna *Phys. Plasmas* **25** 043518

[36] Light M and Chen F F 1995 Helicon wave excitation with helical antennas *Phys. Plasmas* **2** 1084–93

[37] Chen F F, Sudit I D and Light M 1996 Downstream physics of the helicon discharge *Plasma Sources Sci. Technol.* **5** 173–80

[38] Light M, Sudit I D, Chen F F and Arnush D 1995 Axial propagation of helicon waves *Phys. Plasmas* **2** 4094–103

[39] Chen F F 1991 Plasma ionization by helicon wave *Plasma Phys. Control. Fusion* **33** 339–64

[40] Boswell R W 1975 Non-convective parametric instability associated with whistler wave resonance cone *Phys. Lett. A* **55** 93–4

[41] Krämer M, Aliev Y M, Altukhov A B, Gurchenko A D, Gusakov E Z and Niemi K 2007 Anomalous helicon wave absorption and parametric excitation of electrostatic fluctuations in a helicon-produced plasma *Plasma Phys. Control. Fusion* **49** A167–75

[42] Akhiezer A I, Mikhailenko V S and Stepanov K N 1998 Ion-sound parametric turbulence and anomalous electron heating with application to helicon plasma sources *Phys. Lett. A* **245** 117–22

[43] Corr C S, Plihon N, Chabert P, Sutherland O and Boswell R W 2004 Spatially

limited ion acoustic wave activity in low-pressure helicon discharges *Phys. Plasmas* **11** 4596–602

[44] Kwak J-G, Wang S J, Kim S K and Cho S 2006 Density fluctuations measured by a mm-wave collective scattering in helicon plasmas *Phys. Plasmas* **13** 074503

[45] Kline J L and Scime E E 2003 Parametric decay instabilities in the HELIX helicon plasma source *Phys. Plasmas* **10** 135–44

[46] Boswell R W and Giles M J 1976 Trapping of Decay Waves in Whistler Resonance Cones *Phys. Rev. Lett.* **36** 1142–4

Chapter 5
Hollow density formation and off-axis electron heating

5.1 Introduction

Plasma expansion along a diverging magnetic field is studied extensively in both astrophysical [1,2] and laboratory plasmas [3–5]. Plasma flows along the diverging magnetic field leading to magnetic reconnection is a well-known astrophysical phenomenon [6,7] too. In this connection, particularly of interest is the helicon plasma source with an expanding plasma geometry and diverging magnetic field due to its potential application as plasma thruster [3,8,9] for space propulsion. The efficiency of thrust generation in such device critically depends on the radial profiles of plasma density and temperature, and also of electric and magnetic fields [10]. These profiles (except that of the magnetic field) have been studied experimentally [5,11,12] and are found to depend substantially on the generation of diamagnetic current, Hall current, and additional ionization in the expanding diffusion chamber. In the magnetic nozzle geometry, one of the interesting aspects observed and supported by particle-in-cell simulation [13] is that a hollow density profile is generated in the expansion chamber[4,14,15]. This is of serious concern as such type of structure within magnetically expanding plasma causes reduction of the total thrust [11,12] and, therefore, it is necessary to avoid/remove the hollowness of the radial density profile at the nozzle throat to increase the thrust efficiency. However, the understanding of the generated hollow density profile in the expanding plasma is still not comprehensive and demands exploration of the individual roles played by the Hall and diamagnetic currents, and of the source of additional off-axis ionization.

In the helicon plasma source with expanding plasma geometry and diverging magnetic field, an off-axis energetic electron component has been observed experimentally [4,14]. These electrons, evidently created by skin heating [16][17] in the source region close to the location of radio frequency (RF) antenna, are transported from the source to the expansion chamber via the last diverging magnetic field lines emerging from the open exit of the source chamber. They are speculated to have a role in the formation of the hollow density profile [4,14] by off-axis ionization. However, since the ionization length of these fast electrons is substantially larger than the system dimensions, the proposed explanation needs further investigation. The formation of the hollow density structure is also explained in an alternative manner by the radial transport of plasma induced by the radial electric field generated because of magnetized electrons and unmagnetized ions in the expansion chamber [13,15]. In this mechanism, an azimuthal current is proposed to be driven by the E×B drift (Hall current) which in the presence of the axial magnetic field causes radially outward plasma transport. This explanation has been supported by experiment[15] and particle-in-cell simulation[13]. However, in a recent experiment [10,16], an azimuthal current was observed in a helicon thruster, which was seen to be diamagnetic in nature and opposite in direction. In our experiment, the hollow density structure is observed in the expansion chamber, even in the absence of the radial electric field. This contradicts the observations of Ref. 13 and 15. The distinct roles of the magnetic and geometric expansions were studied in our experiment, and it was found that the magnetic expansion plays the dominant role in the hollow density formation in the presence of off-axis energetic tail electrons. In the magnetic expansion region, these electrons rotate in azimuthal direction due to the gradient-B drift. As a consequence, their traversed distance is sufficiently enhanced to allow impact ionization of the neutrals and produces the hollow density structure.

In this chapter, the roles of the gradient-B drift and the absolute strength of the magnetic field in the formation of hollow density are discussed. In the present experiment, the magnetic field is varied, which effectively changes the ion Larmor radii in both the source and the expansion chambers, and the effects on the radial profiles are examined. Most interestingly, we observe that the on-axis peaked radial density profile in the magnetically expanding plasma transforms to a hollow profile when the external magnetic field strength is sufficiently increased. The transition occurs when the ions become magnetized in the expansion chamber, i.e., the ion Larmor radius started becoming smaller than the chamber radius. So, effectively, by changing the magnetic field, the density profile can be either center peaked, or flat or hollow. On the other hand, the density in the source chamber always remains center peaked, irrespective of the magnetic field of our experiment.

In this connection it should be noted here that none of the explanations stated so far, whether it is based on Hall current [13,15] or diamagnetic current [10] or ionization by high energy electrons along the last field line[14], predicts any critical magnetic field across which the plasma density profile undergoes peak-to-hollow transformation in the magnetic nozzle. Our observations, therefore, may lead to effective control of plasma density profile by the external magnetic field, and this may contribute to the understanding and improvement of the efficiency of the helicon source-based thrusters.

The rest of the chapter is organized as follows. In section 5.2, the experimental arrangement is discussed. In section 5.3, experimental results obtained for the plasma parameters in both source and expansion chambers are discussed. This section is followed by the discussion in section 5.4 and, finally, a summary is presented in Section 5.5.

5.2 Experimental arrangements

The present experiments are carried out in the HeX, as shown in Fig. 5.1. The whole system is evacuated to a base pressure of 1×10^{-6} mbar using a diffusion pump connected to the expansion chamber. Argon is used as the working gas in the pressure range of 0.7–3 x10^{-3} mbar. An 18 cm long right helicon antenna, placed around the source chamber and energized by a 13.56 MHz RF power generator through an L-type impedance matching network, produces the plasma. The reflected power is kept less than 2% for all the experiments. The axial location of the antenna center is defined as z = 0, and all other axial locations are with reference to this position, as shown in Fig. 1.

To distinguish the contributions of geometric and magnetic expansion in downstream plasma characteristics, independent experiments are carried out in two different magnetic field configurations. In one magnetic field configuration, four electromagnet coils (3 to 6) are energized, causing the maximum of the divergence magnetic field gradient occurrence near the

z ~ 46 close to the geometric expansion location (z = 45 cm). This named as Close Geometry Magnetic Divergence (CGMD) configuration, which is shown in Fig. 5.1(a). In other configurations, coil no. 7 is also energized pushing the maximum of the divergence magnetic field gradient move further down to and positioning near the z ~ 63 cm about 18 cm away from the geometrical expansion location. We termed it as Far Geometry Magnetic Divergence (FGMD) configuration, and it is shown in Fig. 5.1(b).

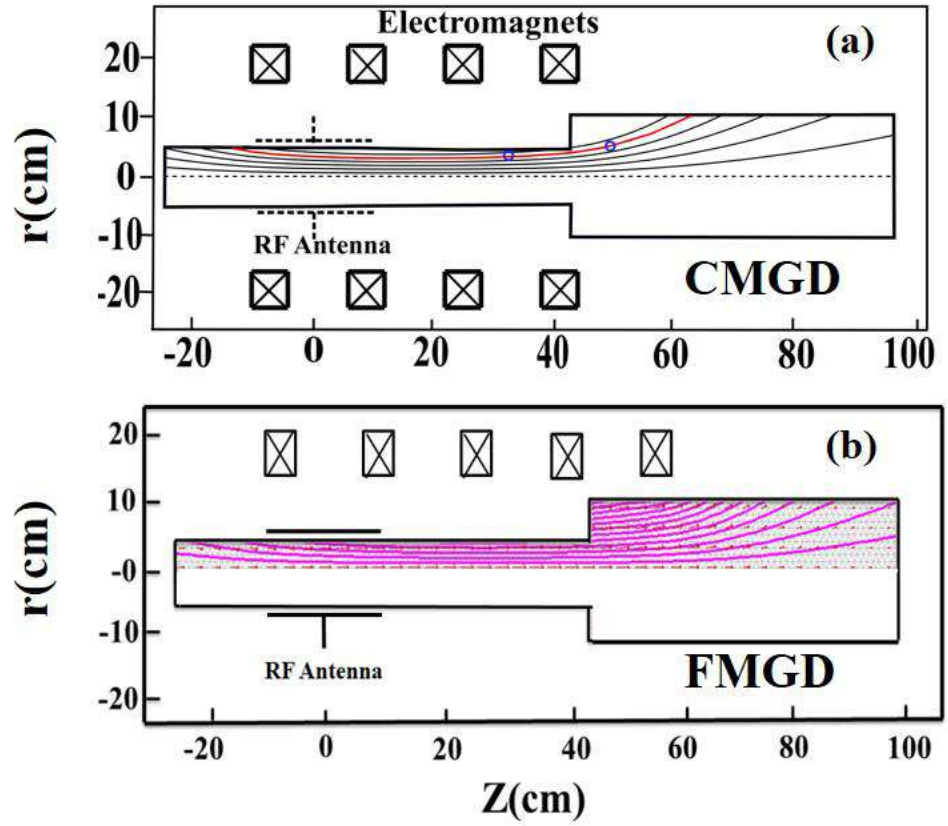

Fig. 5.1: (a) Close geometry magnetic divergence (CGMD) configuration and (b) far geometry magnetic divergence (FGMD) configuration.

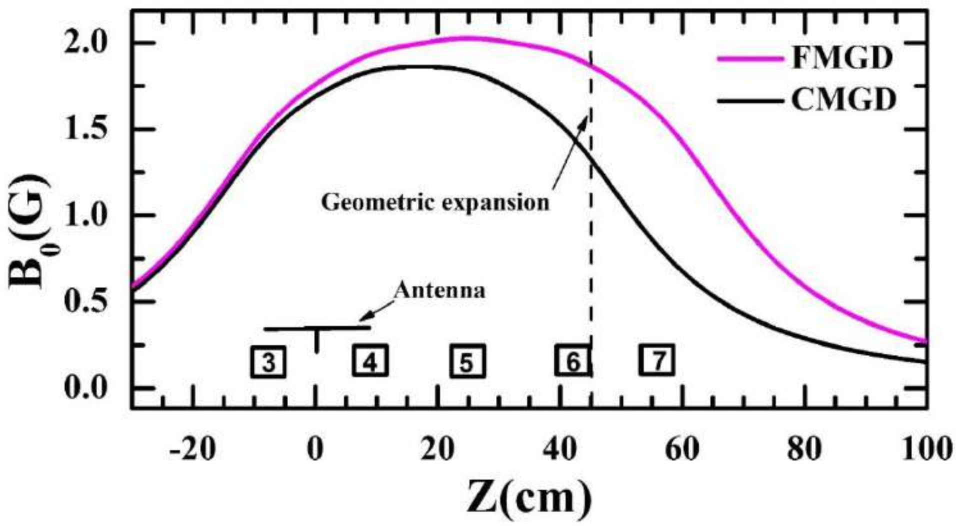

Fig. 5.2: Simulated magnetic field strength in FMGD and CMGD configurations when 1 A DC current is passed through 3-7 and 3-6 electromagnets, respectively. The vertical dash line shows the location of geometric expansion.

The simulated magnetic field strengths in FMGD and CMGD configurations are shown in Fig. 5.2 when 1A DC current is passed through 3-7 and 3-6 electromagnets, respectively.

5.3 Results

In order to understand the physics behind the formation of hollow density profile in the expansion chamber, the radial profiles of plasma density, n_0 and electron temperature, T_e are measured using RF compensated Langmuir probes. Two separate RF compensated Langmuir probes of nearly equal collection areas are used to measure profiles perpendicular to the external magnetic field in the present experiments. An L-shaped RF compensation Langmuir probe is used in the expansion chamber; by rotation and translation of the probe, it has been possible to position it at various radial and axial directions, respectively.

5.3.1 Far Geometry Magnetic Divergence (FGMD)

Measurement of the radial profiles of plasma density is carried out in both configurations. In this subsection, the results of FGMD configuration (Fig. 5.1(b)) are discussed. An L-shaped RF compensated Langmuir probe is positioned at two different axial locations, namely, z = 50 cm and 65 cm. The z = 50 cm location is near the geometric expansion throat, and it is in the uniform magnetic field region well behind the magnetic divergence. Whereas, the z = 65 cm location is far ahead of geometric expansion throat and it is just after the magnetic divergence. It is expected that the influence of the geometric expansion at z = 45 cm should be stronger in the first position than in the second since the latter is far away from the geometric expansion. Fig. 5.3

shows the experimental result at z = 50 and 65 cm with filling gas pressure 1×10^{-3}mbar and 95 A electromagnet current (I_B), which corresponds to the maximum magnetic field in the source chamber around 200 G. It is seen from the Fig. 5.3 that the radial profile of the plasma density is peaked at z = 50 cm. However, radially hollow plasma profile is observed at z = 65 cm. Similar experiments are carried out at different RF powers, which is shown in Fig. 5.4. Fig. 5.4 depicts the same plasma behavior as in Fig. 5.3 that is density is hollow at z = 65 cm and peaked at z = 50 cm. Here it should be noted that the z = 65 cm location is after and z = 50 cm location is before the magnetic divergence. Therefore, it is quite evident that the magnetic divergence is playing the dominant role, not the geometric expansion, in the formation of the hollow density profile. Moreover, the total number of particles integrated over the circular cross-section at z = 65 cm, i.e., after the magnetic divergence is much more than that before the magnetic divergence (Fig. 5.3 and 5.4). Such observation implies that there must be some mechanism which increases the total number of particles after the magnetic divergence, like local ionization.

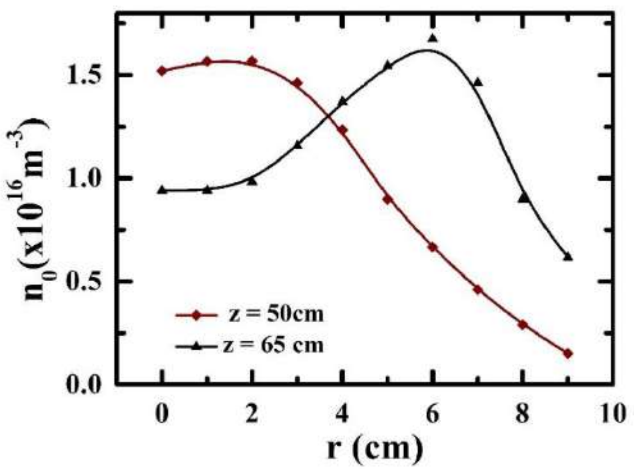

Fig. 5.3: Radial density profile in FGMD configuration at z = 50 (solid diamonds) and 65 cm (solid triangles), at 100W, pressure 1×10^{-3}mbar, 95 A. The magnetic field

strength is 1.73 G/A and 1.12 G/A at z = 50 and 65 cm respectively. Data are spline fitted for representation purpose only.

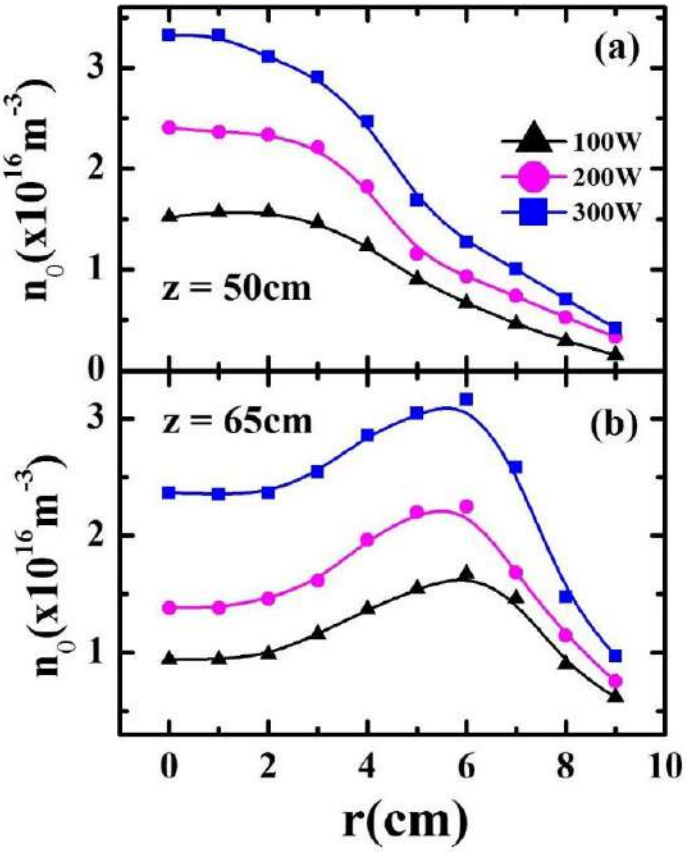

Fig. 5.4: Radial density profile in FGMD configuration at (a) z = 50 and (b) 65 cm, at 100W (solid triangle), 200 W (solid circle) and 300 W (solid square) for pressure 1×10^{-3}mbar, I_B =95 A. The magnetic field strength is 1.73 G/A and 1.12 G/A at z = 50 and 65 cm respectively. Data are spline fitted for representation purpose only.

5.3.2 Close Geometry Magnetic Divergence (CGMD)

In this subsection, the results of CGMD configuration (Fig. 5.1(a)) are presented. The radial profiles of n_0 and T_e are obtained using the RF compensated

Langmuir probe at two different axial locations, z = 31 cm and 50 cm and are shown as blue circles in Fig. 5.1(a). These locations are chosen such that one corresponds to before (z_{before} = 31 cm), and the other after (z_{after}= 50 cm) both the magnetic and geometric expansions (Fig. 5.1(a)). In CGMD configuration z = 50 cm location is just after the magnetic divergence and in the non-uniform magnetic field region (Fig. 5.1(a)). In CGMD configuration the magnetic field strengths are ~1.75 G/A and ~1.1 G/A at z = 31 and 50 cm, respectively, as shown in Fig. 5.2. As speculated that the off-axis tail electrons have a role in the formation of hollow density profile, simultaneous measurement of electron temperature also performed in CGMD configuration. The estimation of effective electron temperature ($T_{e,eff}$) from the cold and tail electron populations is described in the subsection 3.3.4.

To observe the evolution of the radial profiles with the applied magnetic field, four different values of I_B (45 A, 87 A, 130 A, and 174 A) are chosen, and the results are shown in Fig. 5.5. Fig. 5.5(a) and 5.5(b) show the radial profiles of n_0 and T_e at z_{before} whereas Figs. 5.5(c) and 5.5(d) show the corresponding radial profiles at z_{after} at a fixed RF power of 200 W and argon pressure of 1×10^{-3} mbar. From Fig. 5.5(a) it is seen that the radial profiles of plasma density in the source chamber at z_{before} are peaked on-axis for all values of I_B and the ratio of the center to edge (r ~ 4 cm) densities decreases as I_B is increased. At this location the electron temperature, T_e remains nearly the same on-axis for all values of I_B and gradually increases towards the edge. Interestingly, T_e at this axial location peaks at an outer radial location and its peak value increases with I_B (Fig. 5.5(b)). Increase in the plasma density at the outer edge follows a similar trend as of the effective electron temperature there. It is seen from Figs. 5.5(a) and 5.5(b) that radial profiles of plasma parameters in the source chamber are not substantially different above an I_B value of 87A.

Contrasting behavior of the radial density profile is observed with a magnetic field strength in the expansion chamber at z_{after}. Though the plasma density remains peaked on-axis for I_B = 45 A, it becomes hollow for I_B values greater than 80 A (Fig. 5.5(c)). The density peaks off-axis at r ~ 5 cm. At this axial position (z_{after} = 50 cm), the magnetic field is divergent (Fig. 5.1(a)). The amount of hollowness, i.e. the ratio of peak-to-center density also increases with I_B. The behavior of the radial profiles of T_e with increasing I_B at this location follows that in the source chamber, i.e. T_e peaks off-axis (Fig. 5.5d). The ratio of peak-to-center electron temperature increases with I_B. The peak location nearly coincides with that of the density peak location at z = 50 cm. Value of electron temperature remains nearly the same (about 4.5±1 eV) on-axis at the locations before, and after the magnetic expansion, however, they are significantly different at outer radial locations. It seems that the electrons having temperature of 9-12 eV at the outermost radial location (r ~ 4 cm) in the source chamber are not transported in the expansion chamber for all values of I_B. The electrons in expansion chamber at z = 50 cm have maximum temperature of 6 – 8 eV at r ~ 5 cm, which corresponds to the electron temperature at r = 3 ± 0.5 cm in source chamber (z = 31cm).

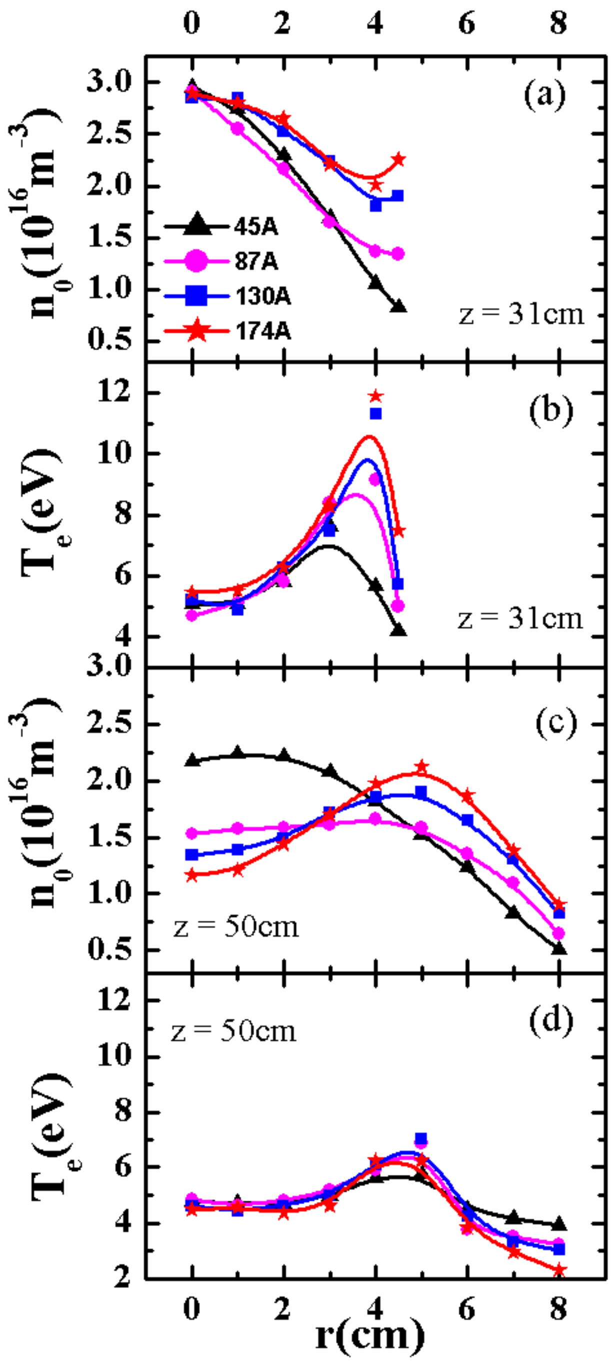

Fig. 5.5: (a), (c)plasma density and (b), (d) electron temperature in CGMD configuration at z = 31 cm and z = 50 cm, respectively at 200W RF power and $1x10^{-3}$mbar Argon pressure for I_B = 45A (solid triangles), 87 A (solid circle),130 A (solid square), and 174 A (solid star). Data are spline fitted for representation purpose only.

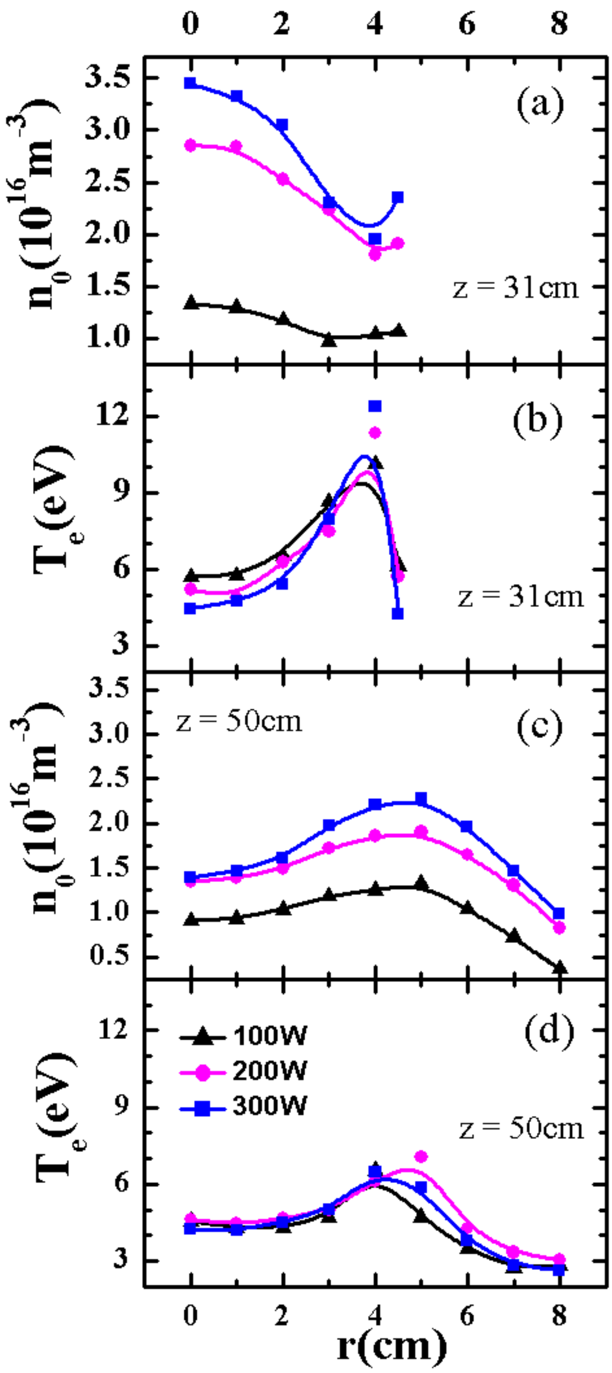

Fig. 5.6: Radial profiles of plasma density in CGMD configuration at locations (a) z = 31 cm and (c) z = 50 cm. Radial profiles of electron temperature in CGMD configuration at locations (b) z = 31 cm and (d) z = 50 cm for different RF powers, 100 W (solid triangles), 200 W (solid circle), and 300 W (solid square) at fixed I_B = 130 A and Argon pressure = $1x10^{-3}$ mbar. Data are spline fitted for representation purpose only.

After establishing that the plasma density profile is center-peaked in the expansion chamber at the low magnetic field, but becomes hollow above the certain magnetic field, we try to explore whether this hollow nature depends on other relevant parameters of the plasma source, like RF power and fill-in pressure. Fig. 5.6 and Fig.5.7 show the results of such investigations. First, the operating RF power is varied from 100 W to 300 W while keeping the coil current, I_B, and fill-in pressure of Argon at fixed values of 130 A and 1×10^{-3} mbar, respectively. The radial variations of plasma density and electron temperature are shown in Fig. 5.6. In the source chamber, the radial profiles of plasma density remain center peaked for all RF power values; however, the density increases throughout the profile with increasing RF power (Fig. 5.6(a)). The effective electron temperature peaks at the radially outward location (at r ~ 4 cm) and does not vary substantially with RF power (Fig. 5.6(b)). In the expansion chamber, the plasma density shows a hollow profile for all RF powers (Fig. 5.6(c)), though overall density increases to some extent with RF power. Electron temperature is also peaked radially outward at r ~ 4-5 cm (Fig. 5.6(d)) and does not vary much with RF power.

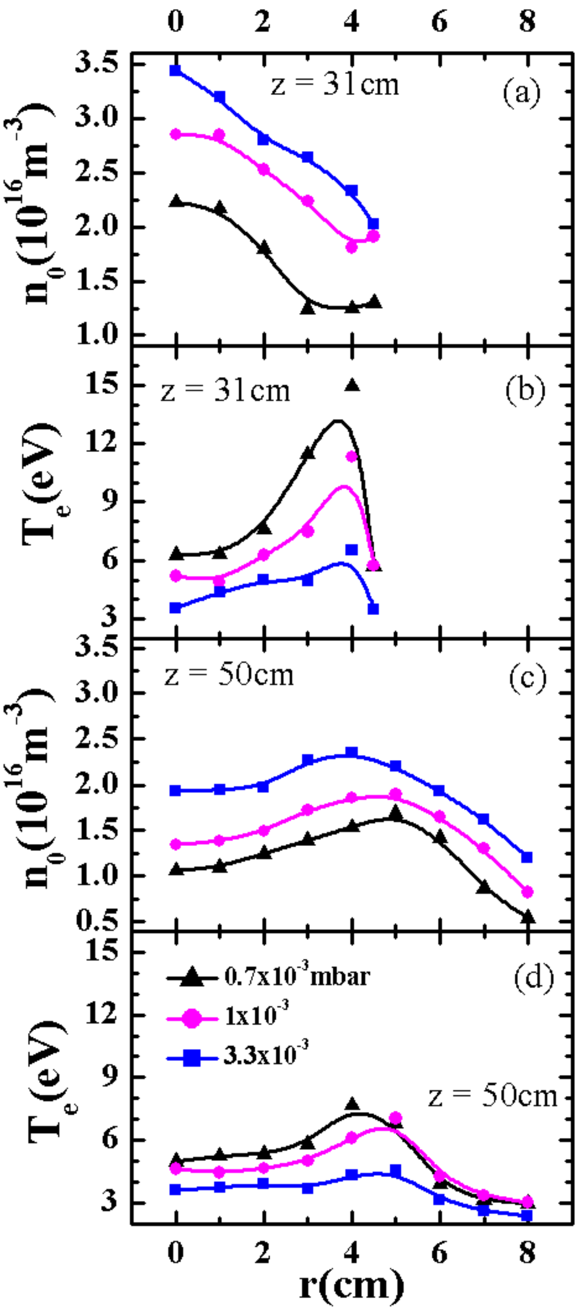

Fig. 5.7: Radial profiles of plasma density in CGMD configuration at axial locations of (a) z = 31cm and (c) at z = 50cm and that of electron temperature in CGMD configuration at axial locations of (b) z = 31cm and (d) z = 50cm for different fill-in pressure values of 0.7×10^{-3} mbar (solid triangles), 1×10^{-3} mbar (solid circle), and 3.3×10^{-3} mbar (solid square) at RF power = 200W and I_B = 130A. Data are spline fitted for representation purpose only.

Next, the fill-in pressure of Argon is varied from 0.7×10^{-3} to 3.3×10^{-3} mbar while keeping constant the values of magnet coil current, I_B and RF power at 130 A and 200 W, respectively. The measured radial profiles of plasma density and electron temperature are shown in Fig. 5.7. In the source chamber (z = 31 cm) the plasma density profiles remain axially peaked for all fill-in pressure values (Fig. 5.7(a)) and the density increases throughout the radius with increasing fill-in pressure. The electron temperature radial profiles (Fig. 5.7(b)) also remain peaked at the radially outer location, but the temperature is reduced throughout the radius with increasing pressure. In the expansion chamber, the hollowness in the density radial profile persists, and the density increases over the whole profile with pressure, but with increasing pressure, the hollowness tends to be suppressed (Fig. 5.7(c)). Similar behavior is observed with the electron temperature (Fig. 5.7(d)), which remains peaked off-axis but decreases with increasing pressure at all radii.

5.4. Discussion

The experimental results presented in Figs. 5.5 to 5.7 point towards two broad aspects: (i) irrespective of the values of the electromagnet coil current, the radial profiles of the electron temperature remain peaked off-axis in both source and expansion chambers, though the peak values are different, and (ii) the plasma density is center-peaked in the source chamber irrespective of the coil current, however, it becomes hollow in the expansion chamber only above a critical value of the coil current, that is magnetic field. It should be mentioned also that the behaviors explained in (i) and (ii) above do not change much when RF power and pressure are varied independently. In the following discussions, we elaborate on these findings and explore the underlying physics behind these observations.

5.4.1 Off-axis electron heating

The region of radially outward electron temperature peaking solely depends on operating conditions of helicon plasma discharge. It has been observed by several researchers [18–21] that depending on the input operating parameters (RF power, gas pressure, and applied magnetic field), helicon discharge can be operated in capacitive (E), inductive (H) or Helicon wave (W) heating mode. The radial structures of plasma density and electron temperature are also dictated by the dominant mode of discharge operation. In our operating conditions, the discharge is predominantly in the inductive mode where a skin current is induced in the plasma edge by the rf antenna current. The off-axis peaking of the electron temperature near the radial plasma boundary in the source chamber (Fig. 5.4-5.6) is indicative of a local electron heating mechanism due to this effect (skin effect).

In an insulating source discharge tube where the helicon antenna is placed around the tube, a skin layer is formed near the radial boundary where most of the RF-power is transferred to the electrons [16,17], and plasma is produced by electron impact ionization. The skin depth[22], is given by $\delta = \frac{\sqrt{2}\,c}{\omega_{pe}}\left(\frac{\nu_{en}}{\omega}\right)^{1/2}$, where c is the speed of light. ν_{en} is electron-neutral collision frequency and ω_{pe} is electron plasma frequency. With a typical plasma density of $1.5 \times 10^{16} m^{-3}$ the skin depth is about $\sim$2 cm, which is less than half the source chamber radius. As there is an external magnetic field, the bulk electrons are unable to freely diffuse radially from the skin layer, or in other words, the electrons which are present in skin layer are restricted by reduced cross-field diffusion. This is presumably the reason why the electron temperature profile in the source region (shown in Figs. 5.5-5.7) is peaked off-axis. The increase of the off-axis electron temperature with the increase of external magnetic field (Fig. 5.5(b)), is due to better confinement of these electrons in the skin layer because of smaller gyroradii ~ 0.44 mm for an average electron energy of 12 eV in 300 G (z = 31cm). Higher temperatures with an increase in the magnetic field also result in higher ionization rate coefficients [22] and add to a further increase in the edge density in the source tube (Fig. 5.5(a)) in our experiment. The reason behind the formation of a tail in the electron energy distribution in the source chamber near the antenna location is not comprehensively understood yet. However, tail electrons have been observed generally in similar devices. As ionizing collisions are statistical in nature, it may be possible that some of the high energy electrons in this region, instead of losing energy by ionizing collisions, remain in the plasma exhibiting a tail in the population. The high energy electrons are transported by the last diverging peripheral magnetic field lines emerging from open exit of source into the expansion chamber, as shown in Fig. 5.1(a).

The electrons that are very close to the source radial boundary at r ~ 4 cm are not transported into the expansion since these electrons are tied to magnetic field lines and follow the curvature of the magnetic field (Fig. 5.1(a)) to hit the source peripheral wall near to the open exit and are lost. Hence the electron energy distribution including the high energy tail in the expansion chamber at r ~ 5 cm, corresponds to that at the radial location of r ~ 3-3.5 cm in source chamber (shown by the circle in Fig. 5.1(a)). The external magnetic field plays an important role for maintaining of the electron temperature gradient radially in our experiment as inhibition of cross field diffusion restricts interaction among electrons of all regions.

5.4.2 Hollow density formation

Formation of hollow density profile in the expansion chamber can either be due to radially outward transport of plasma or due to additional ionization off-axis. Fig. 5.8 shows the local plasma potential profiles in the same conditions as in Fig. 5.5(c) and 5.5(d). The radial electric field at z = 50 cm is negligible, < 0.7 V/cm. So, the possibility of outward radial transport due to **E**× ***B*** drift (or Hall current) of electrons in hollow density formation can be ruled out in our experiment.

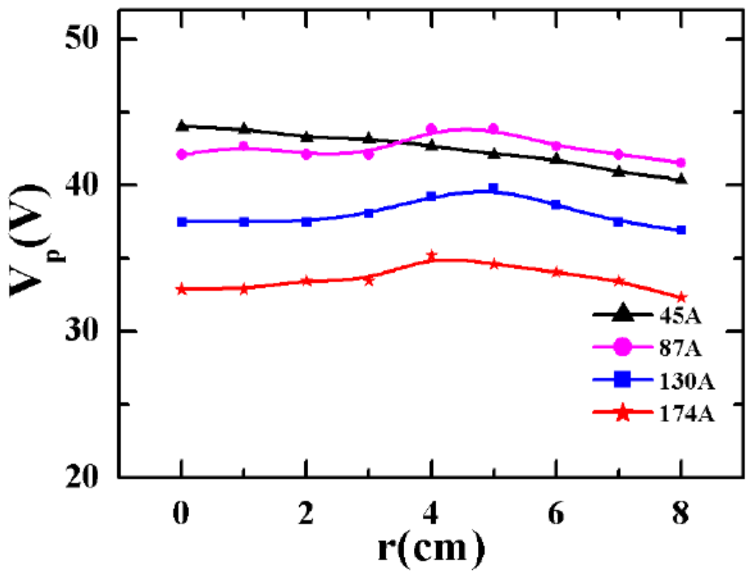

Fig. 5.8: Plasma potential radial profile in CGMD configuration at z = 50 cm in the expansion chamber at 200 W RF power and 1×10^{-3} mbar Argon pressure for I_B = 45 A (solid triangles), 87 A (solid circle), 130 A (solid square), and 174 A (solid star). Data are spline fitted for representation purpose only.

It is evident from the section 5.3.1 that magnetic divergence is playing the dominant role in the formation of the hollow density profile. It is also clear from Fig.

5.3, and Fig. 5.4 that a total number of particles integrated over the circular cross-section after the magnetic divergence is higher than that before, implying the existence of local ionization mechanism. A similar increase in the integrated density over the cross-section in downstream plasma was reported in ref. [4] and [15]; however, no clear explanation was given. Charles et al. and Takahashi et al. observed the tail electrons at off-axis location [4,14] but did not talk in detail about the ionization mechanism. The electron impact ionization scale length is quite large, more than the machine length, at working pressure.

Saha et al. [15] have seen the on-axis high energy electrons, which, they argued, cannot explain the results either. Experimentally we also observe the off-axially confined tail electrons in our plasma from the RF-compensated single Langmuir probe at the location of r = 5 cm in CGMD configuration. The I–V characteristic of the probe, shown in Fig. 5.9 reveals a second component (tail) of electrons. The temperature of high energy tail electrons in the expansion chamber ranges from 12-15 eV and their population generally [23,24] is about 15-20 % of the total electron density. So, there is a substantial number of electrons having energies 2-3 times their temperatures (~20-50 eV) off-axis. However, their ionizing collision length at an argon pressure of 1×10^{-3}mbar is given by $\lambda_{en} = 1/\sigma n_n$ is quite large $\sim$150 cm, that is much larger than system size. Hence, the plasma electrons, only by traversing linear distance along the magnetic field inside the device, are most unlikely to cause the ionization of the neutrals that increase the local density at off-axis to form hollow plasma after the magnetic divergence. However, the fact is that the hollowness is observed only after the magnetic divergence, where there is a strong gradient of the magnetic field.

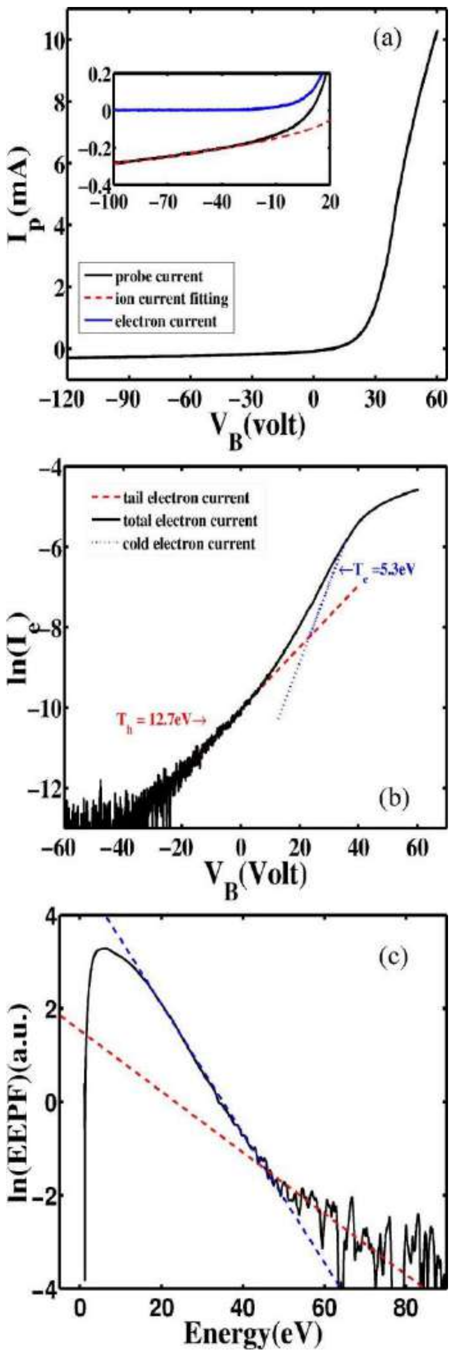

Fig. 5.9: (a) Langmuir probe I-V trace in the expansion chamber at (r, z) = (5,50) cm with 200 W RF power, 130 A coil current, and Argon fill pressure of 1x10^{-3} mbar in CGMD configuration. The contributions of ion (red dashed line) and electron (solid blue line) currents to the probe current for probe bias in the range of -100 V to +20 V are shown in the inset. , (b) semi-logarithm of I-V trace and linear fit of hot (red dashed line) and cold (blue dotted line) electron population (c) EEPF deduced using an active analog differentiator for the same conditions.

It indicates may be an inhomogeneous magnetic field has a role to play in this matter. The magnitude of the magnetic field, B, changes not only in the radial direction but also in the axial direction. It is well known that in the presence of a gradient in the magnetic field value, ∇B, a moving charged particle suffers a gradient-B drift and attains a drift velocity given by the expression: $\boldsymbol{v}_{\boldsymbol{\nabla B}} = \left(\frac{mv_{\perp}^2/2}{qBL_B}\right)\boldsymbol{n}$, with $\frac{\boldsymbol{n}}{L_B} = \frac{\boldsymbol{B}\times\nabla B}{B^2}$. Here L_B represents the scale length of B and $\boldsymbol{n}$ is the unit vector which along with the sign of q determines the direction of the drift, whereas $v_{\perp}$ is the perpendicular velocity component of a particle with the charge q and mass m. The calculated value of L_B at $(r, z) = (5{,}50)$ cm from the simulated magnetic field strength of $B_0 = 50 - 200$ G in our experiment is about $\sim 60 - 65$ cm. The gradient-B drift velocity calculated from the above formula for electron energy range of 20-50 eV comes about to be $v_{\nabla B} = 0.5$ to 2×10^6 cm/s in the $-\theta$ direction. So it seems, near the magnetic divergence, because of a strong magnetic field gradient, a substantial number of ionizing electrons in a radially localized region around r = 5-6 cm are rotating azimuthally with large velocity. These electrons can traverse a much longer distance near the magnetic divergence and can cause the ionizing collisions with neutrals within few rotations building up a local density off-axis. This explains why we observe the hollow density profile in this region. The presence of energetic electrons at the off-axis location (Fig. 5.9) adds to the cause more favorably. Ions also suffer the gradient-B drift, but in the opposite direction; however, because of having a much lower temperature, their rotation speed is negligible. The gradient-B drift in the expansion chamber causes the rotation of the high energetic electrons in the azimuthal direction with a speed of 2×10^6 cm/s but does not significantly affect the energy of the electrons. The rotation confines the electrons enough so that they traverse the ionization length in much shorter distance in the axial direction. The rotation speed is higher for a higher electron energy, a smaller magnetic field and a smaller radius of magnetic curvature.

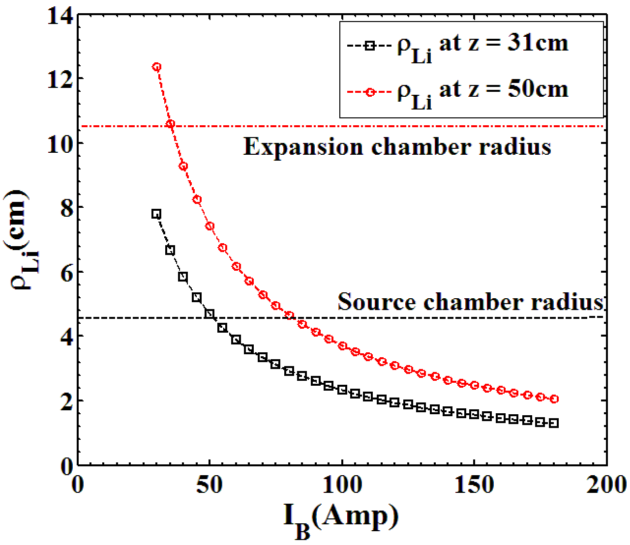

Fig. 5.10: Ion Larmor radius ρ_{Li} vs. coil current I_B in source chamber (z = 31 cm, open square) and in the expansion chamber (z = 50 cm, open circle). The magnetic field strength ~1.75 G/A and ~1.1 G/A at z = 31 and 50 cm, respectively.

However, in the present experiment, the interesting result is that a characteristic value of the magnetic field is observed above which the hollowness in plasma density profile in the expansion chamber arises (Fig. 5.5(c)). The density profile is center peaked for the magnetic field of 50 G (corresponding to the coil current I_B = 45 A) and starts becoming hollow around I_B = 87 A (95 G). So, it seems the grad-B drift effect is an essential condition, but it may not be a sufficient one to form the radial hollow density profile.

In order to find out the possible reason behind the critical value of the magnetic field observed, in Fig. 5.10 we plot the calculated ion Larmor radii at the two axial locations (where the experimental results of Fig. 5.5-5.7 are obtained) for different coil currents. The values of the source and expansion chamber radii are also indicated in the figure for comparison. Interestingly, it should be noted here that out of the four values of I_B (45 A, 87 A, 130 A, and 174 A) for which the profiles of Fig. 5.5-5.7 are obtained, only for I_B =45 A the ion Larmor radius in the expansion chamber is close to the chamber radius, that is, the ions here are not magnetized; for I_B = 87 A it is nearly half the radius, and for all other currents, the ions are totally magnetized. The change in the plasma density profile depends on the confinement of ions through ion gyroradius in expansion chamber (radius 10.5 cm) as explained below. For the magnetic field of 50 G at Z = 50 cm, the ion gyroradius ~ 9 cm, that is, close to the system radius. There, though the high energy electrons are confined and the gradient-B effect produces the off-axis ionization as explained above, but the ions are not magnetized, consequently, the ions, that may be produced off-axis, are lost quickly to the wall and so are the electrons to maintain quasi-neutrality. As a result, the density remains center-peaked. For 95 G of the magnetic field (corresponding to I_B of 87 A) the ion gyroradius becomes ~ 4.8 cm, which is half the chamber radius; here the ions are barely magnetized, and the density is flattened radially. For still higher values of the magnetic field, the ion gyroradius becomes much smaller than the system dimension and the plasma density starts to become hollow.

The hollowness of the plasma density and temperature profiles lead to a hollow electrons pressure profile as shown in Fig. 5.11. As a consequence, an electron diamagnetic current flows in anti-diamagnetic direction at r ∼5 cm for I_B = 130 and 174 A, whereas is in diamagnetic direction for r > 5 cm. This is consistent with recent measurements [10]. However, the anti-diamagnetic direction of azimuthal current within magnetically expanding plasma causes reduction of the total thrust in a plasma thruster, since it reverses the direction of Lorentz force in presence of a radial component of the applied diverging magnetic field [11][25].

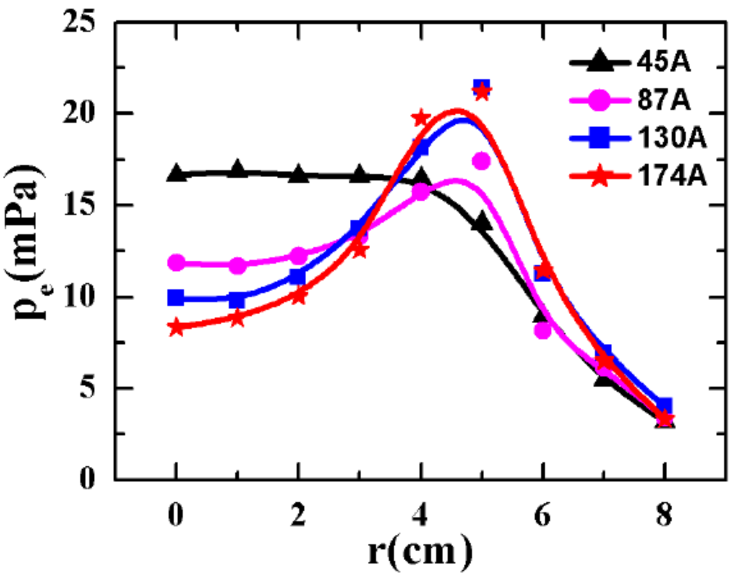

Fig. 5.11: Radial profiles of electron pressure, P_e in expansion chamber (z = 50 cm) at 200 W RF power and 1×10^{-3} mbar Argon pressure in CGMD configuration for I_B values of 45 A (solid triangles), 87 A (solid circle), 130 A (solid square), and 174 A (solid star).

5.5 Summary

The radial density profile in the magnetically expanding plasma is found to be peaked on-axis and evolves into a hollow profile as the diverging magnetic field at the axial location is increased beyond a critical value. The experimental results show that when the magnetic divergence and geometric expansion coincide, the hollow density formation occurs in front of both. However, when the magnetic divergence is shifted away from the fixed geometrical expansion, the formation also shifts and always follows the location of magnetic divergence. No hollow profile is observed immediately after the geometric expansion. This led us to conclude that the magnetic divergence is playing the dominant role, not the geometrical expansion for the formation of the hollow density profile. Moreover, the total number of particles integrated over the circular cross-section after the magnetic divergence is much higher than that before the magnetic divergence

It is seen that this hollow density profile is formed only when both electrons and ions are magnetized at this location and where the presence of magnetic divergence helps to increase the confinement of hot electrons due to the azimuthal rotation caused by the grad-B drift. On the other hand, irrespective of the plasma operating conditions of the experiment, the source radial density profile is center-peaked. The effective electron temperature is peaked radially outward in the source region for all values of the magnetic field due to the RF skin heating effect near the helicon antenna, where a hot electron component is also generated. The hot electrons and the temperature profile hollowness are transported to the expansion chamber along the divergent magnetic field lines, and the hollowness becomes more prominent for higher magnetic fields. Our investigations reported in this work represent not only a fundamental work to understand the downstream hollow density profiles in helicon plasmas, but also signifies the role of the magnetic field as a control parameter for thrust output in future helicon source-based thrusters.

References

[1] Block L P 1978 A double layer review *Astrophys. Space Sci.* **55** 59–83

[2] Marsch E 2006 Kinetic Physics of the Solar Corona and Solar Wind Living Reviews in Solar Physics *Living Rev. Sol. Phys* **3**

[3] Longmier B W, Bering E A, Carter M D, Cassady L D, Chancery W J, Díaz F R C, Glover T W, Hershkowitz N, Ilin A V., McCaskill G E, Olsen C S and Squire J P 2011 Ambipolar ion acceleration in an expanding magnetic nozzle *Plasma Sources Sci. Technol.* **20** 015007

[4] Charles C 2010 High density conics in a magnetically expanding helicon plasma *Appl. Phys. Lett.* **96** 051502

[5] Takahashi K, Charles C, Boswell R and Ando A 2014 Effect of magnetic and physical nozzles on plasma thruster performance *Plasma Sources Sci. Technol.* **23** 044004

[6] Arefiev A V. and Breizman B N 2005 Magnetohydrodynamic scenario of plasma detachment in a magnetic nozzle *Phys. Plasmas* **12** 043504

[7] Su Y, Veronig A M, Holman G D, Dennis B R, Wang T, Temmer M and Gan W 2013 Imaging coronal magnetic-field reconnection in a solar flare *Nat. Phys.* **9** 489–93

[8] Charles C 2009 Plasmas for spacecraft propulsion *J. Phys. D. Appl. Phys.* **42** 163001

[9] Takahashi K, Lafleur T, Charles C, Alexander P and Boswell R W 2012 Axial

force imparted by a current-free magnetically expanding plasma *Phys. Plasmas* **19** 083509

[10] Takahashi K, Chiba A, Komuro A and Ando A 2016 Experimental identification of an azimuthal current in a magnetic nozzle of a radiofrequency plasma thruster *Plasma Sources Sci. Technol.* **25** 055011

[11] Takahashi K, Lafleur T, Charles C, Alexander P and Boswell R W 2011 Electron Diamagnetic Effect on Axial Force in an Expanding Plasma: Experiments and Theory *Phys. Rev. Lett.* **107** 235001

[12] Takahashi K, Charles C and Boswell R W 2013 Approaching the Theoretical Limit of Diamagnetic-Induced Momentum in a Rapidly Diverging Magnetic Nozzle *Phys. Rev. Lett.* **110** 195003

[13] Rao S and Singh N 2012 Numerical simulation of current-free double layers created in a helicon plasma device *Phys. Plasmas* **19** 093507

[14] Takahashi K, Charles C, Boswell R, Cox W and Hatakeyama R 2009 Transport of energetic electrons in a magnetically expanding helicon double layer plasma *Appl. Phys. Lett.* **94** 191503

[15] Saha S K, Chowdhury S, Janaki M S, Ghosh A, Hui A K and Raychaudhuri S 2014 Plasma density accumulation on a conical surface for diffusion along a diverging magnetic field *Phys. Plasmas* **21** 043502

[16] Ando A, Boswell R W, Takahashi K, Charles C and Akahoshi H 2017 High temperature electrons exhausted from rf plasma sources along a magnetic nozzle *Phys. Plasmas* **24** 084503

[17] Cunge G, Crowley B, Vender D and Turner M M 2001 Anomalous skin effect and collisionless power dissipation in inductively coupled discharges *J. Appl. Phys.* **89** 3580–9

[18] Ellingboe A R and Boswell R W 1996 Capacitive, inductive and helicon-wave modes of operation of a helicon plasma source *Phys. Plasmas* **3** 2797–804

[19] Degeling A W, Jung C O, Boswell R W and Ellingboe A R 1996 Plasma production from helicon waves *Phys. Plasmas* **3** 2788–96

[20] Chi K-K, Sheridan T E and Boswell R W 1999 Resonant cavity modes of a bounded helicon discharge *Plasma Sources Sci. Technol.* **8** 421–31

[21] Franck C M, Grulke O and Klinger T 2003 Mode transitions in helicon discharges *Phys. Plasmas* **10** 323–5

[22] Lieberman M A and Lichtenberg A J 2005 *Principles of Plasma Discharges and Materials Processing* (Hoboken, NJ, USA: John Wiley & Sons, Inc.)

[23] Sheehan J P, Raitses Y, Hershkowitz N, Kaganovich I and Fisch N J 2011 A comparison of emissive probe techniques for electric potential measurements in a complex plasma *Phys. Plasmas* **18** 073501

[24] Umair Siddiqui M and Hershkowitz N 2014 Double layer-like structures in the core of an argon helicon plasma source with uniform magnetic fields *Phys. Plasmas* **21** 020707

[25] Ahedo E and Merino M 2011 On plasma detachment in propulsive magnetic nozzles *Phys. Plasmas* **18** 053504

Chapter 6
Electron energy distribution of current free double layer

6.1 Introduction

In a previous chapter (chapter 4) it has been discussed that the efficiency of the helicon plasma source is greatly enhanced when the helicon wave is launched into a non-uniform magnetic field configuration. Another feature of the non-uniform (diverging) magnetic field in the expanding helicon plasma geometry is the current free double layer (CFDL), which spontaneously forms in low pressure expanding plasma. The helicon discharge in a magnetic field geometry with a strong magnetic field gradient often shows the formation of CFDL, which is correlated with an acceleration of the plasma electrons and ions across it [1–6]. CFDLs are the potential structure forming self consistently in a current less plasma. Most of the works on the CFDL are reported in low pressure geometrically expanding helicon plasma systems with a diverging magnetic field. Still, efforts are going on to find out the cause behind the formation of CFDLs as well as to understand the role of neutral pressure [7], antenna frequency [8], magnetic field strength [9,10], location of magnetic field gradient [11,12] and ion and electron dynamics [13–16]. There has been considerable interest in the formation of CFDLs in rf-driven low-pressure plasmas and in their application to such diverse fields as plasma thrusters for space propulsion[17–19] and the physics of the solar corona [20,21]. Hence the study of the formation of the current free double layer and the physics related to ion and electron dynamics has its own importance. In most of the work, the existence of CFDL is manifested by the presence of ion beams in downstream of CFDL[3,5,6,13,22]. However, understanding of electron dynamics is also equally important to fully understand the behavior of CFDL. This chapter deals with the experimental measurement of electron energy probability function (EEPF) in the presence and absence of CFDL. In the presence of CFDL, the ion beam is observed in our experiments before [23], but the study of electrons is not done yet.

The rest of the chapter is organized as follows. In section 6.2, a brief introduction of the double layer is given. In section 6.3 a brief description of CFDL and helicon CFDL followed by electron dynamics of CFDL are given. Section 6.4 discusses the electron dynamics of CFDL and provides the measurement of upstream and downstream electron energy probability function. The dependency of CFDL on the magnetic field gradient is discussed in section 6.5, followed by a summary in section 6.6.

6.2 Double Layer

A double layer is a localized narrow region inside the plasma which sustains a large potential difference, i.e., an electric field. A double layer (DL) is the layers of two oppositely charged species spontaneously forming in the plasma. It is different from the normal sheath as the DL forms in the bulk of the plasma whereas the sheath forms on the boundary of any material inserted into the plasma or on the boundary of the plasma chamber. The very earlier work in double layers (or anode double sheaths) was undertaken by Langmuir 1929 [24] in DC discharge. Later Alfven (1958) [25] suggested that double layers could be responsible for the acceleration of the electrons onto the upper atmosphere creating the visible aurora. The electric double layers have also been studied experimentally [26] theoretically [27–29] and by computer simulation [30–32]. DLs must fulfill three conditions [33]: a potential drop larger than T_{ef}, an electric field stronger in the DL than outside and quasi-neutrality is locally violated at the position of the DL. In most cases, the plasma on either side of the DL is collisionless or exhibits low collisionality. A DL is defined as weak if $\varphi_{DL}/T_{ef} < 10$ and strong if $\varphi_{DL}/T_{ef} > 10$, where φ_{DL} is double layer potential drop and T_{ef} is the free electron temperature, i.e., the electron temperature on the low potential side of the DL.

In general, there are four groups of particles, groups of tapped (or reflected) electrons, and ions, and groups of free (or passing) electrons and ions are postulated [34] to maintain the electric double layer as shown in Fig. 6.1. A group of electrons or ion having low energy than the DL potential barrier are trapped on the high or low potential side of DL, they are termed as trapped electron or ions. A group of electrons having high energy than the DL potential barrier, overcome the DL and pass from high to low potential, called free or passing electrons similarly, group of ions having high energy overcome the DL and pass from low to high potential called free or passing ions. The presence of an electron and ion energetic beam (or accelerated electrons and ions) on the high and low potential side of the DL, respectively, results from particle acceleration while traversing the DL. These two ‘additional populations’ (accelerated ions flowing downstream and accelerated electrons flowing upstream) are to be considered along with the passing populations when estimating the net current through the DL (Fig. 6.1). The double layer is called current free if this net current is zero and term as current free double layer (CFDL). This can be true if the equal electron and ion fluxes flow across the double layer potential.

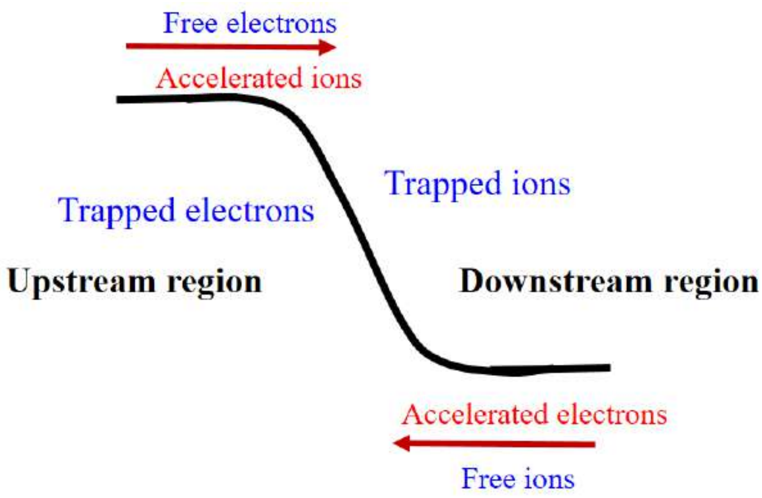

Fig. 6.1: Description of potential structure of double layer and associated groups of particles.

6.3 Current Free Double Layer (CFDL)

Until the late 1970s, it was commonly believed that a necessary condition for the formation of double layers was that the electron drift velocity had to exceed the electron thermal velocity [30], as shown by computer simulations [32] and laboratory experiments [35]. However, Mozer et al. [36] observed large potential difference along the auroral field lines, where the electron drift velocity was much less than the electron thermal velocity, suggesting that the presence of current was not necessary for the formation of double layers. Inspired by this peculiar observation, Sato and Okuda [37] showed, by using a particle-in-cell simulation, that double layers may form even if the electron drift velocity was smaller than the electron thermal velocity.

Perkins and Sun [38] by an analytical model suggest that current-free (with no net current at all) double layers could exist. The authors found solutions of the Vlasov equation that would satisfy a set of conditions, such as the existence of an abrupt potential drop surrounded by quasi-neutral plasma with no electric field. Hatakeyama et al. [39] seem to be the first ones to report an experimental stable current-free double layer. However, in their experiment, although the double layer was not imposed by drawing current through the plasma or by imposing a potential difference, the double layer was forced by creating two plasmas with two different temperatures interacting with each other. Hairapetian and Stenzel [40] have also reported the experimental formation of stationary current-free double layers. In their experiment, a very- low-pressure two-temperature plasma was created and allowed to expand into a longer chamber. By carefully adjusting the two distinct temperatures, the authors could form a stationary double layer. However, this double layer was "only" stationary during the duration of the pulse, i.e., for 1 ms. Sato and Miyawaki [41] have theoretically investigated a situation similar to that of Hairapetian and Stenzel [40], that is a plasma composed of two populations of electrons with two distinct temperatures. These authors have derived a minimal electron temperature ratio compatible with a double layer.

6.3.1 Helicon CFDL

A new class of current free double layer (CFDL) has been discovered in laboratory radio frequency plasmas [42]. This stationary CFDL spontaneously forms in a current-free expanding plasma in a divergent magnetic field for low operating gas pressure. The plasma source is mostly a helicon source, and it can be operated in capacitive, inductive and helicon wave mode. A supersonic ion-beam has been measured downstream of this double layer for both argon [13] and hydrogen[22] discharges. Charles and Boswell [43] showed that the current-free double layer was formed in the first 100 μs of the discharge; Charles also showed that this was accompanied by some charging of the source walls. The current-free double layer has many potential applications, such as in plasma processing [44], plasma propulsion [19,45] and space plasma [20]. The formation of double layers in current-free plasmas and associated ion beams were confirmed by similar experiments [4,6,12].

6.3.2 Helicon CFDL models

After the observation of CFDL in helicon plasmas, many models have tried to explain the observations of CFDL formation in low-pressure helicon discharges by taking various groups of trapped and free-electron distributions as shown in Fig. 6.1.

Taking a Maxwellian upstream electron population, with no additional energetic electron population, Chen [46] considered a Boltzmann plasma expansion in the diverging magnetic field. As the plasma expands in a diverging magnetic field, the density and plasma potential fall according to Boltzmann expansion. For a potential drop of $0.5\ kT_e/e$, the ions get accelerated and attain the Bohm velocity after which their density decrease is slower than that of electrons. So the plasma expansion is considered to be a simple Boltzmann expansion until the point where quasi-neutrality breaks down ($n = n_0 e^{-1/2}$) and the double layer forms. The double layer potential is self-consistently set such that equal electron and ion fluxes can flow across it, and it is, therefore, current free. As to a floating material inside plasma, the ion and electron fluxes are equal, this double layer structure thus evolved is current free in nature. For Argon plasma, a CFDL drop of ~ 5.2 kT_e/e was proposed. This model does not take into account the collisions and also cannot explain the 165 eV ion beams observed by Weibold et al. [35] for a 14 eV plasma.

Lieberman et. al. [1,2] developed a theory for the formation of a low-pressure current-free double layer in a plasma expanding from a small diameter source to a larger diameter chamber. In their model they consider the diffusive flows of the quasi-neutral plasma in the source and expansion chamber that coupled to the dynamics of the particles in the non-neutral double layer. To maintain the current-free nature of the experimental double layer, they introduced a fifth species apart from the four groups of charged particles: (a) thermal electrons (b) accelerated electrons flowing upstream (c) thermal ions (d) accelerated ion flowing downstream. This fifth species consists of a backstreaming population of electrons formed by the reflection of the all (almost) the accelerated electron group by the sheath at upstream wall of source region. Their explanations can explain the pressure dependency of CFDL strength observed in the experiments. For very low neutral pressure where collisions are sparse, additional ionization in the source cannot happen, and the CFDL vanishes, and for higher pressures, there is no longer a need for ionization by the energetic electrons and the double layer vanishes.

Takahashi et al. [15,47] measured the electron energy distribution function in an expanding low-pressure helicon discharge. In the upstream region of CFDL, the electron energy distribution function shows a very clear change in slope at energy (called break energy, ε_{break}) corresponding to CFDL potential drop. Electrons with lower energy than the ε_{break} are trapped in CFDL potential barrier, whereas those with high energy than ε_{break} overcome the potental barrier called as trapped and free electrons, respectively. The temperature of the trapped electron was higher than the free electrons as the trapped electron stays for a longer time, being trapped in the wall sheath and the CFDL potential. In the downstream, they have observed only the free population which escaped from the source. The free electrons, which go to the right side grounded wall sheath get reflected and then again get accelerated when they enter the upstream. So a single source of plasma can sustain the CFDL.

6.3.3 Electron Dynamics of CFDL

Various models have been dedicated to understanding the electron dynamics of CFDL generated in low pressure rf driven expanding plasma. Lieberman et al. [1,48] have introduced the backstream electrons polulation at upstream to explain the current-free nature of the experimental double layer. Instead of mono-energetic electrons, they have used non-Maxwellian ‘beamlike’ electron distribution for backstreaming electron. Thakur et al. [49] interpreted the increase upstream ionization is induced by the backstreaming ‘beam’ electrons. Aanesland et al. [7,50] experimentally observed the coexistence of instability with CFDL and interpreted as an ionization instability which is induced by the backstreaming ‘beam’ electrons. The earliest experimental observation by Charles et al. [13] has shown the existence of an electron beam in Langmuir probe characteristic. Meige et al. [51] by one dimensional particle in cell (PIC) simulation have shown the absence of electron ‘beam’ at an upstream side of CFDL instead their results of electron energy distribution show the presence of depleted tail at higher energy. The experimental measurement of electron energy probability function (EEPF) by Takahashi et al. [47] does not show any electron beam component rather they have shown the depleted tail of EEPF at upstream [47,52] very similar to PIC result [51]. Our measurements of EEPF reproduces the results of Takahashi et al. [47], showing the depleted tail of EEPF rather than the electron ‘beam’.

6.4 Electron energy Probability function (EEPF) of CFDL

The existence of the CFDL like potential and associated ion beam generation in HeX are already discussed in previous work [23]. In this work, the particular interest is the electron energy distribution function in the presence and in the absence of CFDL.

The experiments are performed in HeX experimental device, which consists of a 9.5 cm diameter and 70 cm long cylindrical glass source tube. The left end of the source tube is terminated with a pyrex plate. The right end of the source tube is contiguously connected to a 50 cm long 21 cm diameter grounded stainless steel diffusion chamber. The helical antenna wrapped over the glass tube is fed from an RF matching network/generator system operating at 13.56 MHz. A diffusion/rotary pumping system is connected to the sidewall of the diffusion chamber and provides a base pressure of 1×10^{-6}mbar. Argon feed gas is connected to the sidewall of the diffusion chamber. Four electromagnets in Close Geometry Magnetic Divergence (CGMD) configuration, as shown in Fig 6.2, are used to generate the magnetic field. In this magnetic field configuration, the location of maximum magnetic field gradient and geometric expansion is nearly collocated. In HeX, the reference parameters correspond to an argon pressure of ~0.5×10^{-3} mbar, an rf power of 300 W and a magnetic field of about 220 G in the source region. The axial location of the antenna center is defined as z = 0, and all other axial locations are with reference to this position, as shown in Fig. 6.2 The junction between the source and the diffusion chamber is located at z = 44 cm.

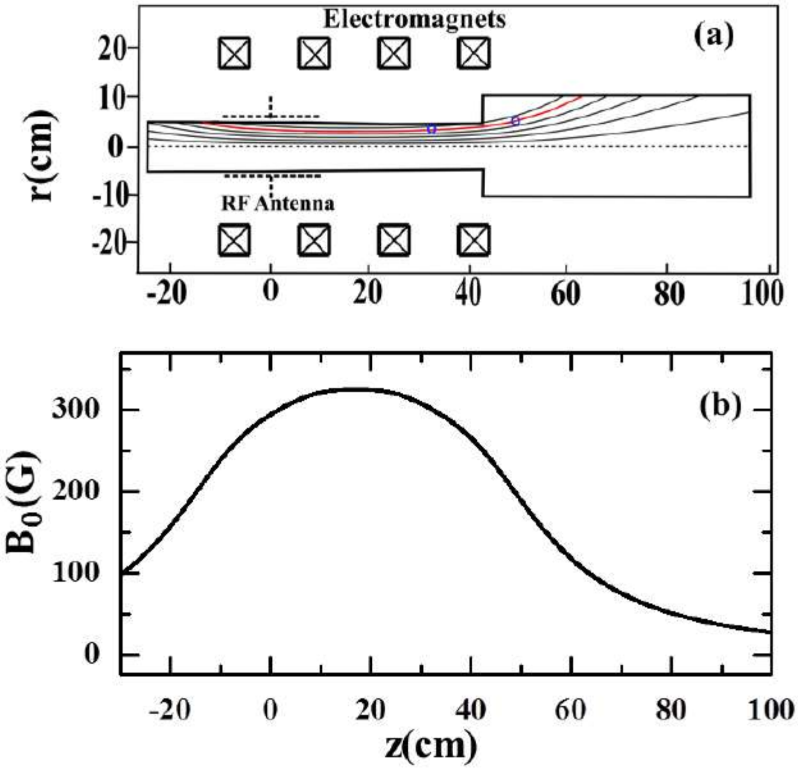

Fig. 6.2: (a) Simulated magnetic field lines and (b) simulated field strength for 174 A applied DC current.

The existence of CFDL like potential in our experiment is shown by the axial plasma potential profile measured using the emissive probe by floating potential method, and this is shown in Fig 6.3. The fall of plasma potential in Fig. 6.3 does not follow the Boltzmanian potential drop which is given by $\boldsymbol{n = n_0 exp(-e\Delta V_P/kT_e)}$. By measuring the plasma density upstream (z = 31cm) and downstream (z = 55cm), $n_0 = \mathbf{3.5} \times 10^{16}\ and\ \mathbf{1.3} \times 10^{16} m^{-3}$ respectively and assuming the constant electron temperature about $T_e = 6.5\ eV$ the Boltzmanian potential drop is about $\Delta V_P \approx 6.7$ Volt, whereas the CFDL potential drop $\Delta V_P \approx 25$ volt $> 4T_e$, confirm the existence of CFDL like potential in our experiment.

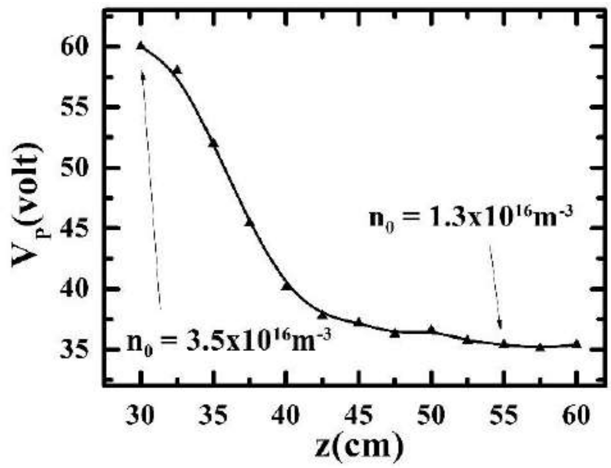

Fig. 6.3: Variation of axial plasma potential profile measured at 300 W RF power, 5×10^{-4} mbar fill pressure and 220G source magnetic field.

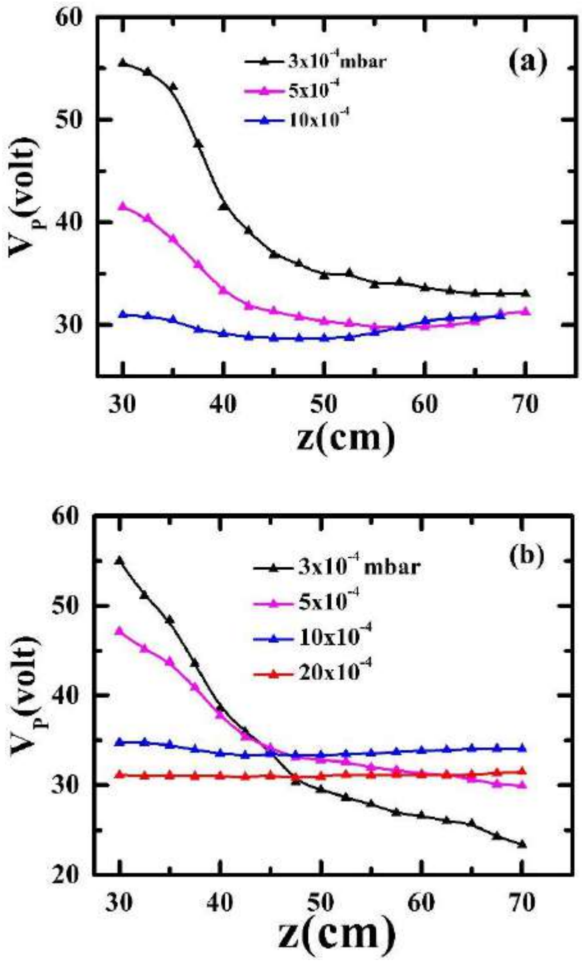

Fig 6.4: Axial plasma potential profile at different fill pressures at 200 W RF power and (a) 300G and (b) 150G source magnetic field.

The existence the CFDL like potential at different fill in pressure for 200 W RF power is shown in Fig. 6.4(a) and 6.4(b) for 300 G and 150 G respectively. Fig. 6.4 shows that the no CFDL like potential exist at pressure $\geq 10 \times 10^{-4}$ mbar.

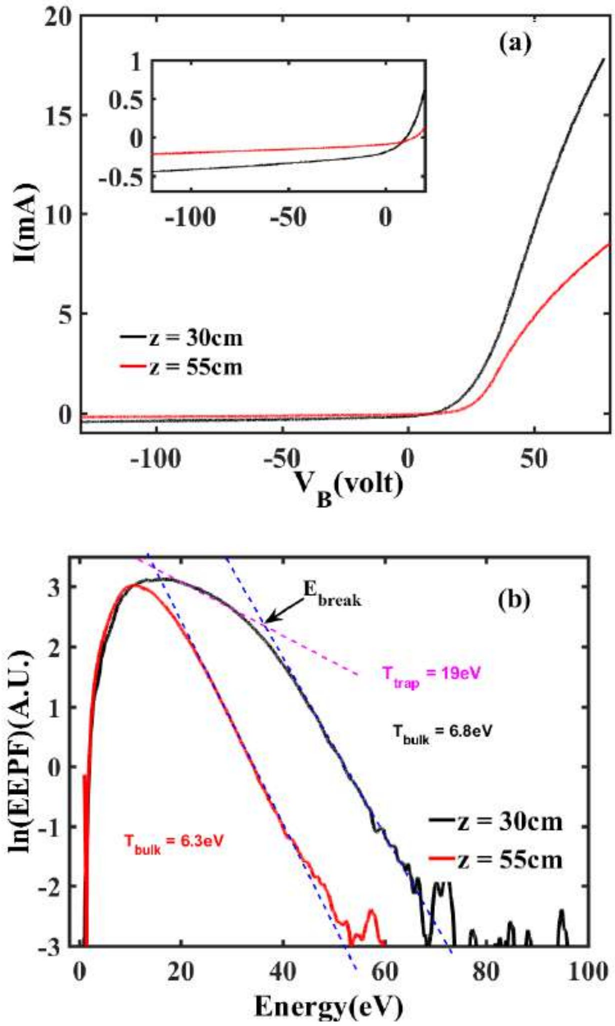

Fig 6.5: (a) I-V characteristics and (b) EEPF at upstream (red curve) and downstream (black curve) plasma at 300W RF power, 220G source magnetic field and 5×10^{-4}mbar fill pressure.

The measurement of electron energy distribution is performed for operating conditions given for Fig. 6.3 at upstream z = 31cm and downstream at z = 55cm. Fig. 6.5(a) shows the measured I-V characteristics at upstream and downstream locations using RF compensated Langmuir probe. The working of RF compensated Langmuir probe is already discussed in section 3.2.2. The measurement of EEPF in RF plasma is difficult due to the distortion of electron retardation region by plasma potential oscillation. The second derivative of I-V characteristics gives information of the EEDF and local plasma potential. The plasma potential is taken as zero crossing of the second derivative and observed EEDF is the remaining part of the curve begin from the plasma potential V_p. The electron in the plasma sees the plasma potential as the zero references for EEDF. The relation between the EEDF and EEPF is given in the section 3.3.3.

The upstream EEPF (black curve) at z = 31 cm is plotted in Fig. 6.5(b), where energy zero corresponding to local plasma potential (V_p ~ 60 V at z = 31, Fig. 6.3). Fig. 6.5(b) shows a clear ε_{break} (break energy) in the slope at about ~ 35 eV, which corresponds to potential drop (25 Volt) of CFDL within 20-30 %. Below ε_{break}, the slope of the EEPF yields a temperature of ~ 19 eV, whereas above ε_{break}, the temperature is ~ 6.8 eV. Fig. 6.5(a) shows the I-V characteristic at upstream at z = 31 cm (black curve). The I-V and EEPF do not indicate any electron beam rather depleted high energy electron as shown in EEPF (Black curve). So our measurement confirms the absence of electron beam at the upstream region.

Fig. 6.5(b) (red curve) shows the downstream EEDF at z = 55 cm (local V_p~ 35 volt, Fig. 6.3). The downstream EEPF shows the temperature~ 6.3 eV. The downstream temperature matches with the upstream depleted temperature within 10-20%. The difference in the local plasma potential upstream and downstream matches with ε_{break} within 20-30%. It is more or less quite evident that the depleted group of upstream electrons with energies greater than ε_{break} match in both density and temperature with the downstream group of electrons, suggesting that they are the same group of electrons that move from the upstream to downstream by climbing the double layer potential of magnitude ε_{break}. Our results verified the measurement performed in the Chi-Kung experiments [47].

The electrons with energy higher than the ε_{break} overcome the double layer potential and appearing in the downstream can be treated as free electrons. Electrons having energy less than the CFDL potential drop (i.e. ε_{break}) are trapped electrostatically between the left side floating wall of the source chamber and CFDL. These electrons in the upstream show a higher temperature (smaller slope) than those electrons having an energy higher than the ε_{break}. The simple explanation for this is that the electrons trapped in the upstream plasma spend a much longer time in the heating fields of the rf antenna whereas the escaping electrons only have (at most) one pass through the rf heating region before they escape.

6.5 Effect of magnetic field gradient on EEPF

In the present experiment, the EEPF is also measured in the absence of the CFDL. In our experiments at low pressures, the formation of CFDL can be controlled by changing the magnetic field gradient location near the throat. Fig. 6.6 shows the variation of magnetic field strengths and their axial gradients for 3-6 (CGMD) to and 3-7 (FGMD) magnetic field configurations. The z = 44 cm is the location of geometric expansion. The plasma potential profile and EEPF are measured in two different magnetic field configurations. In one configuration, four electromagnet coils (3-6) are energized, which causes the maximum magnetic field gradient to occur near the z ≈ 48 cm, close to geometric expansion location z = 44 cm. The result of this magnetic field configuration is already discussed in the previous section 6.5. In other magnetic field configuration, coil no. 7 is also energized along with 3-6 coils, this pushes the maximum magnetic field gradient in the expansion chamber at z ≈ 62 cm, about 18 cm away from the geometric expansion location.

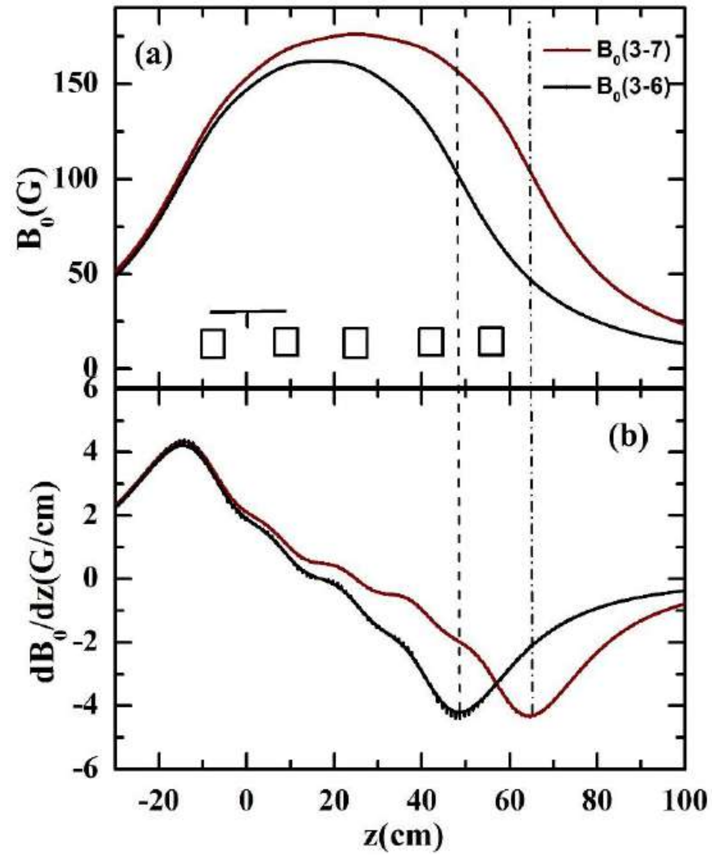

Fig. 6.6: Simulated (a) magnetic field and (b) derivative profiles for two different field configuration with maximum gradient location.

The axial plasma potential profiles of 3-6 and 3-7 magnetic field configurations are shown in Fig. 6.7. A CFDL like potential structure which is seen in 3-6 magnetic field configuration (black curve in Fig. 6.7), and it vanishes in 3-7 magnetic field configuration (pink curve in Fig. 6.7) at constant plasma parameters. Hence, In our experiment only by changing the magnetic field configuration, the double layer can vanish.

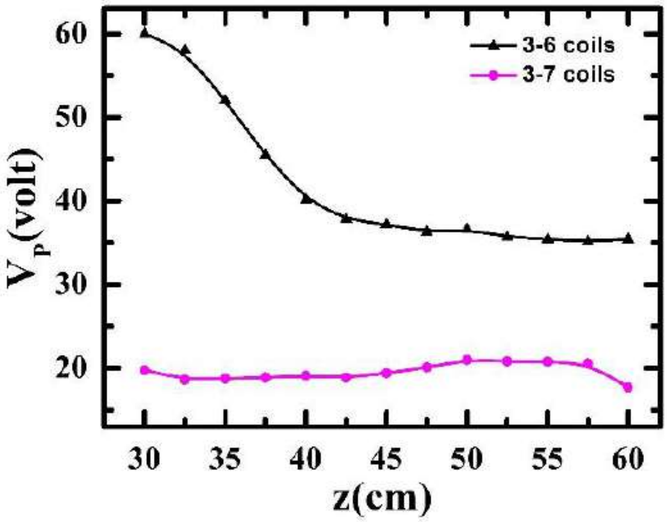

Fig 6.7: Axial variation of plasma potential profile at different magnetic field configuration at fill pressure 5×10^{-4} mbar, 300W RF power, and 220 G source magnetic field.

The measurement of RF compensated Langmuir probe I-V characteristics and EEPF at upstream location z = 31 cm in 3-7 magnetic field configuration is performed, and the results are compared with 3-6 magnetic field configuration. The I-V characteristics and EEPF at upstream z = 31 cm location for 3-6 and 3-7 magnetic field configurations are shown in Fig. 6.8(a) and Fig. 6.8(b). The inset of Fig 6.8(a) shows the ion saturation current which is the measure of ion density. The inset of Fig 6.8(a) shows, for same operating conditions (except magnetic field configuration) the plasma density is high in presence of CFDL (3-6 magnetic field configuration), indicating the more ionization might be due to trapped electron between the CFDL potential barrier and sheath at source floating end wall. The Fig. 6.8(b) also shows the area under the EEPF curve is higher in case of 3-6 magnetic field configuration compared to 3-7 magnetic field configuration.

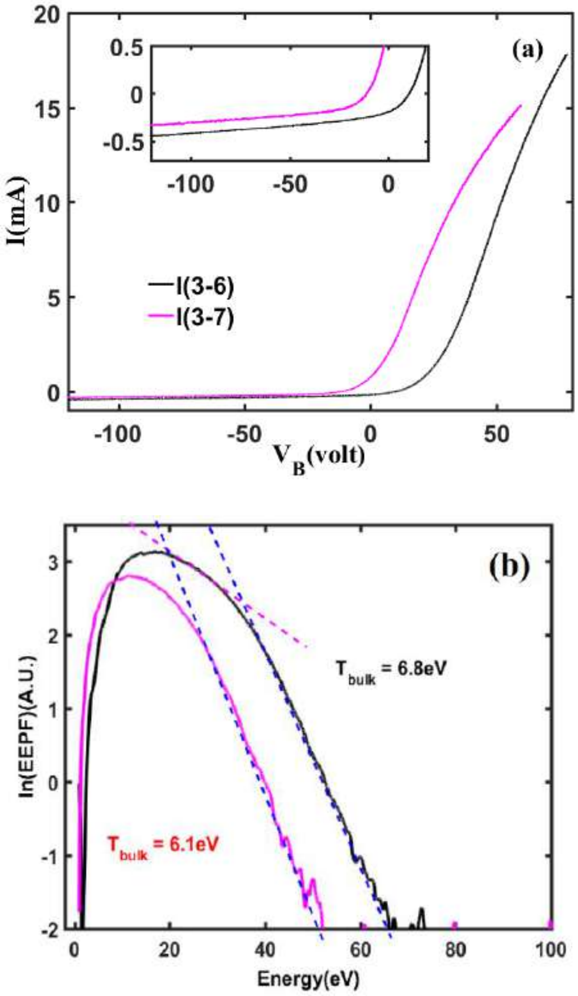

Fig. 6.8: (a) I-V characteristics and (b) EEPF at z = 31cm upstream for different magnetic field configuration at 300W, 220G and 5×10^{-4}mbar argon pressure.

The black curve in Fig. 6.8(b) shows the EEPF in 3-6 magnetic field configuration i.e. in the presence of double layer. This indicates the trapped and depleted tail electrons distributions which are separated by the energy corresponds to CFDL potential drop. This energy know as break energy (ε_{break}). The electron whose energy below than the ε_{break} are trapped between the CFDL and source end wall sheath. However, EEPF in 3-7 magnetic field configuration shows no such kind of nature instead shows a single Maxwellian electron energy distribution. The area under the EEPF curve shows the particle trapping increases the ionization. The electron temperature in the case of 3-6 magnetic field configuration is higher than in case 3-7 magnetic field configuration. This may be due to electrons that are interacting with double layer and getting energy from it.

6.6 Summary

The I-V characteristics and EEPF are measured in the presence and absence of CFDL like potential structure in HeX. The CFDL is formed when the magnetic field divergence and geometric expansion are co-located otherwise, CFDL vanishes under the same operating conditions. In presence of CFDL like structure, at upstream the measured EEPF shows the trapped and depleted tail electron energy distribution which are separated by the ε_{break}. Electron those have energy below than ε_{break} are trapped between the CFDL potential and source end wall sheath. This group of electrons is known as a trapped electron group. Electron those energies higher than the ε_{break} (this makes the depleted tail in EEPF at upstream) overcome the CFDL potential barrier and treated as free electrons. The free electrons at downstream show the approximate Maxwellian distribution and very closely resembles the shape and magnitude of the depleted upstream population. To explain the formation of experimental CFDL, many theoretical models involve the group of accelerated or 'beam' electrons. When the electrons are generated in the ionization process at upstream, among those a group of electrons having the energy less than the CFDL potential barrier is trapped in the high potential side, while a group of electrons having energy overcome the potential barrier. Some of them (if not scattered) is reflected by the sheath at a grounded wall and come back again to a high potential side. Moreover, if some electrons are newly generated via the ionization process at a low potential side, they are electrostatically accelerated from the low to high potential side and should be detected as a beam electron component. This should be seen as a positive slope in EEPF at upstream. In search of the electron 'beam' component we measured the I-V characteristic and EEPF at upstream, our results do not indicate a beam of electrons arriving from the downstream plasma, since there is no sign of a beam in I-V characteristic and also no positive slope in EEPF. However, it can be assumed that the upstream depleted tail electrons arrive from the downstream and can be treated as an accelerated group of electrons.

References

[1] Lieberman M A and Charles C 2006 Theory for Formation of a Low-Pressure, Current-Free Double Layer *Phys. Rev. Lett.* **97** 045003

[2] Lieberman M A, Charles C and Boswell R W 2006 A theory for formation of a low pressure, current-free double layer *J. Phys. D. Appl. Phys.* **39** 3294–304

[3] Charles C 2007 A review of recent laboratory double layer experiments *Plasma Sources Sci. Technol.* **16** R1–25

[4] Cohen S A, Siefert N S, Stange S, Boivin R F, Scime E E and Levinton F M 2003 Ion acceleration in plasmas emerging from a helicon-heated magnetic-mirror device *Phys. Plasmas* **10** 2593–8

[5] Plihon N, Chabert P and Corr C S 2007 Experimental investigation of double layers in expanding plasmas *Phys. Plasmas* **14**

[6] Sun X, Keesee A M, Biloiu C, Scime E E, Meige A, Charles C and Boswell R W 2005 Observations of ion-beam formation in a current-free double layer *Phys. Rev. Lett.* **95** 1–4

[7] Aanesland A, Lieberman M A, Charles C and Boswell R W 2006 Experiments and theory of an upstream ionization instability excited by an accelerated electron beam through a current-free double layer *Phys. Plasmas* **13** 122101

[8] Thakur S C, Hansen A and Scime E E 2010 Threshold for formation of a stable double layer in an expanding helicon plasma *Plasma Sources Sci. Technol.* **19** 025008

[9] Takahashi K, Charles C, Boswell R W and Fujiwara T 2010 Double-layer ion acceleration triggered by ion magnetization in expanding radiofrequency plasma sources *Appl. Phys. Lett.* **97** 141503

[10] Charles C and Boswell R W 2007 The magnetic-field-induced transition from an expanding plasma to a double layer containing expanding plasma *Appl. Phys. Lett.* **91** 201505

[11] Schröder T, Grulke O and Klinger T 2012 The influence of magnetic-field gradients and boundaries on double-layer formation in capacitively coupled plasmas *EPL (Europhysics Lett.* **97** 65002

[12] Sutherland O, Charles C, Plihon N and Boswell R W 2005 Experimental Evidence of a Double Layer in a Large Volume Helicon Reactor *Phys. Rev. Lett.* **95** 205002

[13] Charles C and Boswell R W 2004 Laboratory evidence of a supersonic ion beam generated by a current-free "helicon" double-layer *Phys. Plasmas* **11** 1706–14

[14] Takahashi K, Charles C, Boswell R W and Fujiwara T 2011 Electron Energy Distribution of a Current-Free Double Layer: Druyvesteyn Theory and Experiments *Phys. Rev. Lett.* **107** 035002

[15] Takahashi K, Charles C, Boswell R, Lieberman M A and Hatakeyama R 2010 Characterization of the temperature of free electrons diffusing from a magnetically expanding current-free double layer plasma *J. Phys. D. Appl. Phys.* **43** 162001

[16] Takahashi K, Charles C, Boswell R, Cox W and Hatakeyama R 2009 Transport of energetic electrons in a magnetically expanding helicon double layer plasma *Appl. Phys. Lett.* **94** 191503

[17] Takahashi K, Lafleur T, Charles C, Alexander P, Boswell R W, Perren M, Laine R, Pottinger S, Lappas V, Harle T and Lamprou D 2011 Direct thrust measurement of a permanent magnet helicon double layer thruster *Appl. Phys.*

Lett. **98** 141503

[18] West M D, Charles C and Boswell R W 2008 Testing a Helicon Double Layer Thruster Immersed in a Space-Simulation Chamber *J. Propuls. Power* **24** 134–41

[19] Pottinger S, Lappas V, Charles C and Boswell R 2011 Performance characterization of a helicon double layer thruster using direct thrust measurements *J. Phys. D. Appl. Phys.* **44** 235201

[20] Boswell R W, Marsch E and Charles C 2006 The Current-Free Electric Double Layer in a Coronal Magnetic Funnel *Astrophys. J.* **640** L199–202

[21] Fruchtman A 2006 Electric field in a double layer and the imparted momentum *Phys. Rev. Lett.* **96** 3–6

[22] Charles C 2004 Hydrogen ion beam generated by a current-free double layer in a helicon plasma *Appl. Phys. Lett.* **84** 332–4

[23] Ghosh S, Chattopadhyay P K, Ghosh J, Pal R and Bora D 2017 Transition from single to multiple axial potential structure in expanding helicon plasma *J. Phys. D. Appl. Phys.* **50** 065201

[24] Langmuir I 1929 The Interaction of Electron and Positive Ion Space Charges in Cathode Sheaths *Phys. Rev.* **33** 954–89

[25] Alfvén H 1958 On the Theory of Magnetic Storms and Aurorae *Tellus* **10** 104–16

[26] Hershkowitz N 1985 Review of recent laboratory double layer experiments *Space Sci. Rev.* **41** 300

[27] Andrews J G and Allen J E 1971 Theory of a Double Sheath between Two Plasmas *Proc. R. Soc. A Math. Phys. Eng. Sci.* **320** 459–72

[28] Hasan S S and Ter Haar D 1978 The Alfv�n-Carlquist double-layer theory of solar flares *Astrophys. Space Sci.* **56** 89–107

[29] Torvén S 1981 Modified Korteweg-de Vries Equation for Propagating Double Layers in Plasmas *Phys. Rev. Lett.* **47** 1053–6

[30] Knorr G and Goertz C K 1974 Existence and stability of strong potential double layers *Astrophys. Space Sci.* **31** 209–23

[31] Joyce G and Hubbard R F 1978 Numerical simulation of plasma double layers *J. Plasma Phys.* **20** 391–404

[32] Goertz C K and Joyce G 1975 Numerical simulation of the plasma double layer *Astrophys. Space Sci.* **32** 165–73

[33] Block L P 1978 A double layer review *Astrophys. Space Sci.* **55** 59–83

[34] Raadu M A 1989 The physics of double layers and their role in astrophysics *Phys. Rep.* **178** 25–97

[35] Quon B H and Wong A Y 1976 Formation of Potential Double Layers in Plasmas *Phys. Rev. Lett.* **37** 1393–6

[36] Mozer F S, Carlson C W, Hudson M K, Torbert R B, Parady B, Yatteau J and Kelley M C 1977 Observations of Paired Electrostatic Shocks in the Polar Magnetosphere *Phys. Rev. Lett.* **38** 292–5

[37] Sato T and Okuda H 1981 Numerical simulations on ion acoustic double layers *J. Geophys. Res.* **86** 3357

[38] Perkins F W and Sun Y C 1981 Double Layers without Current *Phys. Rev. Lett.* **46** 115–8

[39] Hatakeyama R, Suzuki Y and Sato N 1983 Formation of Electrostatic Potential Barrier between Different Plasmas *Phys. Rev. Lett.* **50** 1203–6

[40] Hairapetian G and Stenzel R L 1990 Observation of a stationary, current-free double layer in a plasma *Phys. Rev. Lett.* **65** 175–8

[41] Sato K and Miyawaki F 1992 Formation of presheath and current-free double layer in a two-electron-temperature plasma *Phys. Fluids B Plasma Phys.* **4** 1247–54

[42] Charles C and Boswell R 2003 Current-free double-layer formation in a high-density helicon discharge *Appl. Phys. Lett.* **82** 1356–8

[43] Charles C and Boswell R W 2004 Time development of a current-free double-layer *Phys. Plasmas* **11** 3808–12

[44] Charles C, Ramdutt D, Brault P, Caillard A, Bulla D, Boswell R, Rabat H and Dicks A 2007 Low energy plasma treatment of a proton exchange membrane used for low temperature fuel cells *Plasma Phys. Control. Fusion* **49** A73–9

[45] Gesto F N, Blackwell B D, Charles C and Boswell R W 2006 Ion Detachment in the Helicon Double-Layer Thruster Exhaust Beam *J. Propuls. Power* **22** 24–30

[46] Chen F F 2006 Physical mechanism of current-free double layers *Phys. Plasmas* **13** 034502

[47] Takahashi K, Charles C, Boswell R W, Kaneko T and Hatakeyama R 2007 Measurement of the energy distribution of trapped and free electrons in a current-free double layer *Phys. Plasmas* **14** 114503

[48] Lieberman M A, Charles C and Boswell R W 2006 A theory for formation of a low pressure, current-free double layer *J. Phys. D. Appl. Phys.* **39** 3294–304

[49] Thakur S C, Harvey Z, Biloiu I A, Hansen A, Hardin R A, Przybysz W S and Scime E E 2009 Increased Upstream Ionization due to Formation of a Double

Layer *Phys. Rev. Lett.* **102** 035004

[50] Aanesland A, Charles C, Lieberman M A and Boswell R W 2006 Upstream Ionization Instability Associated with a Current-Free Double Layer *Phys. Rev. Lett.* **97** 075003

[51] Meige A and Boswell R W 2006 Electron energy distribution functions in low-pressure inductively coupled bounded plasmas *Phys. Plasmas* **13** 092104

[52] Takahashi K 2019 Helicon-type radiofrequency plasma thrusters and magnetic plasma nozzles *Rev. Mod. Plasma Phys.* **3** 3

Chapter 7
Conclusion and Future scope

The last chapter of this dissertation is divided into two sections. The first section gives an account of a brief summary of the work described in this dissertation followed by the future scope in section 7.2.

7.1 Conclusion

As discussed in chapter 1, the objectives of the present thesis are as follows:

1. To understand the role of non-uniform magnetic field near the antenna for plasma production efficiency.
2. To understand the physics behind the downstream hollow density profile for diverging magnetic field configuration in expansion region
3. To study the relation between current free double layer and electron dynamics in diverging magnetic field configuration in the expansion region.

Based on the above mentioned objectives the experiments are carried in HeX device and the conclusions are as follows:

For several plasma applications, high density plasma is a crucial requirement [1–4]. The high density plasma production is limited due to the inefficient coupling of power from the source to the plasma. In the present thesis, it has been demonstrated experimentally that the original efficiency of helicon plasma source can be further raised when helicon wave launched into non-uniform magnetic field configuration near the antenna center. To study the efficient plasma production in non-uniform magnetic field experiments are carried out in different non-uniform configurations of the magnetic field near the helicon antenna keeping the magnetic field at the center of the antenna < 100 G. Antenna-plasma coupling efficiencies are studied by measuring antenna current with and without plasma. Plasma production efficiencies are also estimated in all the different magnetic field configurations. It has been observed that coupling efficiencies increase with magnetic field non-uniformity near the antenna. This is also reflected in the increase in density throughout the plasma volume. This has been verified by measuring the radial and axial plasma density profiles. At 25 G, antenna efficiency increases from 60% to 80% for low to high non-uniformity in the magnetic field. Here, the excited wavelength is twice the length of the antenna. However, at 50 G magnetic field at the antenna center, the antenna efficiency remains the same (i.e. 80 %) for highest non-uniformity of the magnetic field and goes down for less non-uniform cases. Wavelength excited for 50 G magnetic field at the antenna center is the same as antenna length for the most non-uniform magnetic field. The plasma production is highest in this case as antenna length is equal to helicon wavelength. Moreover, the density is also lower for conventional helicon mode operation (160 G, 800 W) at higher magnetic field compared to the non-uniform magnetic field at the same power level.

After studying the efficient plasma production in a non-uniform magnetic field configuration in the source region, a detailed study has been performed to understand the cause behind downstream hollow density profile for diverging magnetic field configuration in the expansion region. It has been observed previously [5,6] that the presence of hollow density profile in the expanding plasma in the non-uniform (diverging) magnetic field causes a reduction of the total thrust. In the present work, the role of both the geometric expansion and magnetic divergence has been investigated separately. It has been found that, the magnetic divergence plays the dominant role, not the geometrical expansion, in the formation of the hollow density profile. It is also observed that the total number of particles integrated over the circular cross-section after the magnetic divergence is higher than that before the magnetic divergence.

Such observation implies that there must be some mechanism which increases the total number of particles after the magnetic divergence, like local ionization. An off-axis energetic tail electron component has been observed experimentally in the expansion region. These energetic tail electrons are speculated to have a role in the formation of the hollow density profile by off-axis ionization. However, the fact is that the hollowness is observed only after the magnetic divergence, where there is a strong gradient of the magnetic field. The magnitude of the magnetic field, B, changes not only in the radial direction but also in the axial direction. In the presence of a gradient in the magnetic field, a moving charged particle suffers a gradient-B drift. The tail electrons rotate in azimuthal direction due to this gradient-B drift. As a consequence, their traversed distance is sufficiently enhanced to allow impact ionization of neutrals and consequently the production of the hollow density structure. However, in the present experiment, the interesting result is that a characteristic value of the magnetic field is observed above which the hollowness in the plasma density profile in the expansion chamber arises. The density profile is center peaked for the magnetic field of 50 G and started becoming hollow around 95 G. So, it seems the grad-B drift effect is an essential condition, but may not be sufficient to form the radial hollow density profile. It is seen that this hollow density profile is formed only when both electrons and ions are magnetized. Though the high energy electrons are confined and the gradient-B effect produces the off-axis ionization as explained above, but the ions are not magnetized, consequently, the ions, that may be produced off-axis, are lost quickly to the wall and so are the electrons to maintain quasi-neutrality. The effective electron temperature is peaked radially outward in the source region for all values of the magnetic field due to the RF skin heating effect near the helicon antenna, where a tail electron component is also generated. The tail electrons and the temperature profile hollowness are transported to the expansion chamber along the divergent magnetic field lines, and the hollowness becomes more prominent for higher magnetic fields. Our investigations reported in this work are not only a fundamental contribution to understand the downstream hollow density profiles formation in helicon plasmas but also signifies the role of the magnetic field as a control parameter for thrust output in future helicon source-based thrusters.

The diverging or non-uniform magnetic field of the expanding plasma not only affects the density distribution but also the plasma potential. A current free double layer (CFDL) is formed in a magnetically expanding plasma. Furthermore, experiments are performed to study the relation between the current free double layer and electron dynamics in the diverging magnetic field configuration in the expansion region. To study the electron dynamics the electron energy distribution function (EEDF) is measured using analog differentiator technique. In presence of CFDL like structure, at upstream the measured EEPF shows the trapped and depleted tail electron energy distribution which are separated by the ε_{break}. Electron those have energy below than ε_{break} are trapped between the CFDL potential and source end wall sheath. This group of electrons is known as the trapped electron group. Electron those energies higher than the ε_{break} (this makes the depleted tail in EEPF at upstream) overcome the CFDL potential barrier and treated as free electrons. The free electrons at downstream show the approximate Maxwellian distribution and very closely resembles the shape and magnitude of the depleted upstream population. In search of the electron ‘beam’ component we measured the I-V characteristic and EEPF at upstream, our results do not indicate a beam of electrons arriving from the downstream plasma, since there is no sign of a beam in I-V characteristic and also no positive slope in EEPF. However, it can be assumed that the upstream depleted tail electrons arrive from the downstream and can be treated as an accelerated group of electrons.

7.1 Future scope

In the present thesis, the reason of the excitation of helicon waves with a wavelength equal to the antenna length at 50 G for maximum non-uniformity in the magnetic field is not well understood, since no theoretical studies have yet been reported on the antenna spectrum and corresponding absorption for a nonuniform magnetic field near the antenna. The response of the plasma to the applied antenna wave fields, i.e., wave absorption is determined by the distribution of antenna current, which sets the wavenumber spectrum [7,8]. The wavelength spectrum along with the spectral power density is related to the antenna loading, which is synonymous to plasma resistance. In general, the vacuum power spectrum of a helical antenna has been relatively well studied [7]. In those kinds of literature antenna, plasma coupling (spectral amplitudes) has been addressed considering radial density gradient, different antenna, its polarization, and antenna length. However, these studies do not consider a nonuniform magnetic field. The results obtained from the present experiments show that coupling and absorption in the operation of helicon discharges need to be much better understood at least for nonuniform magnetic fields near the antenna. Further study should be carried out to understand the power coupling and absorption mechanism in the presence of non-uniform magnetic field in helicon plasma.

The density peaking at low magnetic field values is the result of wave coupling rather than capacitive or inductive coupling. It is shown that the wave propagation near the resonance cone surface causes significant power absorption. The absorption of helicon wave near the resonance cone surface is correlated with the excitation of electrostatic fluctuation. We observe the frequency peak between 10-20 kHz, which can be related to an ion acoustic-like wave. A detailed study of the nature of electrostatic fluctuation should be carried out to understand the exact mechanism of power deposition in low magnetic field helicon discharges.

A variable frequency RF generator can be used to further study resonance cone propagation as the resonance condition says low magnetic field density peak will be obtained at a higher magnetic field for a higher source frequency.

References

[1] Chen F F 2015 Helicon discharges and sources: a review *Plasma Sources Sci. Technol.* **24** 014001

[2] Longmier B W, Bering E A, Carter M D, Cassady L D, Chancery W J, Díaz F R C, Glover T W, Hershkowitz N, Ilin A V., McCaskill G E, Olsen C S and Squire J P 2011 Ambipolar ion acceleration in an expanding magnetic nozzle *Plasma Sources Sci. Technol.* **20** 015007

[3] Takahashi K, Charles C, Boswell R and Ando A 2013 Performance improvement of a permanent magnet helicon plasma thruster *J. Phys. D. Appl. Phys.* **46** 352001

[4] Perry A J 1991 The application of the helicon source to plasma processing *J. Vac. Sci. Technol. B Microelectron. Nanom. Struct.* **9** 310

[5] Takahashi K, Charles C and Boswell R W 2013 Approaching the Theoretical Limit of Diamagnetic-Induced Momentum in a Rapidly Diverging Magnetic Nozzle *Phys. Rev. Lett.* **110** 195003

[6] Takahashi K, Lafleur T, Charles C, Alexander P and Boswell R W 2011 Electron Diamagnetic Effect on Axial Force in an Expanding Plasma: Experiments and Theory *Phys. Rev. Lett.* **107** 235001

[7] Arnush D and Chen F F 1998 Generalized theory of helicon waves. II. Excitation and absorption *Phys. Plasmas* **5** 1239–54

[8] Fischer B, Kramer M and Enk T 1994 Helicon wave coupling to a finite plasma column *Plasma Phys. Control. Fusion* **36** 2003–20